# Model-Assissted Nonlinear Frequency Response Analysis for Lithium-Ion Battery Ageing

Zur Erlangung des akademischen Grades eines
DOKTORS DER INGENIEURWISSENSCHAFTEN (Dr.-Ing.)

von der KIT-Fakultät für Elektrotechnik und Informationstechnik des
Karlsruher Instituts für Technologie (KIT)
angenommene

Dissertation

von

M.Sc. Hoon Seng Chan

geboren in Penang, Malaysia

| | |
|---|---|
| Tag der mündlichen Prüfung: | 03. Juni 2026 |
| Hauptreferentin: | Prof. Dr.-Ing. Ulrike Krewer |
| Korreferent: | Prof. Dr. Miran Gaberšček |

# Abstract

Lithium-ion batteries are gaining increasing interest, advocated by the recent blooming in the electrification of transportation industries. Consequently, issues such as boosting the efficiency and performance of lithium-ion batteries have been addressed. Nevertheless, the ageing of lithium-ion batteries is still inevitable, and battery scientists still need to discover countermeasures against battery ageing.

A regular battery check-up is essential to keep track of its health status and to identify early signs of premature death of lithium-ion batteries. Among all diagnosis methods in battery research, electrochemical impedance spectroscopy emerges as a promising approach that can distinguish the kinetic and transport losses at different time constants. Nevertheless, this method only probes the linear system behaviour. It does not characterise the inherent nonlinear behaviour of lithium-ion batteries. Thus, nonlinear frequency response analysis (NFRA) was introduced in recent years as an extension to the classical electrochemical impedance spectroscopy.

The application of NFRA has led to some successful use cases in prior studies. In this work, NFRA is further extended to study and quantify the ageing behaviour of lithium-ion batteries. In particular, the following research questions are highlighted in this work: How do the nonlinear signals or harmonics respond to battery ageing? Can harmonics be used to quantify battery ageing or predict the remaining useful life of the battery? What kind of additional information can be gained as compared to other conventional methods? It is found that harmonics are sensitive and positively correlated to battery ageing. An empirical model that is developed for the state-of-health estimation based on NFRA can achieve a promising accuracy with a root mean square error of about 1 %. Furthermore, parameter identification that includes NFRA characterisation improves the identifiability of kinetic parameters in the battery model. Specifically, the charge transfer coefficient can be identified via the second harmonic, which is shown to be not equal to 0.50 as assumed in most of the simulation works.

# Acknowledgement

Pursuing PhD has always in my mind since my undergraduate time. Honestly, I did not have a concrete reason at that time but rather sounds cool to have the title “Doctor” in front of my name. After exposing myself for many years as a part-time student assistant at the university and research institute, I developed an interest in research, more specifically for intellectual pursuits.

It was then in the winter of 2018, that I started my doctoral studies. As compared to a student assistant, the PhD journey wasn’t easy as it requires self-management and self-reflecting qualities like taking the initiative to manage own research and taking proactive approaches to achieve the targeted objectives, which takes time to develop and adapt. And I appreciate Prof. Dr.-Ing. Ulrike Krewer for giving this opportunity, time and space to a neophyte like me. Prof. Dr.-Ing. Ulrike Krewer is not only knowledgeable and always available for scientific discussions but also cares for skill and personality development like self-esteem building and leadership nurture.

Furthermore, I would like to express my gratitude to Prof. Dr.-Ing. Fridolin Röder and PD Dr.-Ing. André Weber, also the NFRA-team, Yan Ying Lee, Julian Ulrich and Prof. Dr.-Ing. Vijayshankar Dandapani for their fruitful and constructive discussions and contributions. Also, thanks to all my colleagues in INES (TUBS) as well as in IAM-ET (KIT), for creating a friendly and comfortable atmosphere to work in. Besides, I would also like to thank all the project partners for the successful collaboration. Not to forget, I would like to especially thank Lars Bläubaum as a mentor, a friend, and a companion, whom we fought along the PhD journey. Without him, I wouldn’t have carried on until today.

Lastly, I would love to thank my family members in Germany as well as in Malaysia for their unconditional support and for always being there for me.

Nuremberg, February 2026 *Hoon Seng Chan*

# Contents

# 1 Introduction

"Energiewende" is the essence of the European energy policy, which aims to liberate the dependency of the European energy sector from the fossil-based energy market. To combat the aggravating climate change, the European Union sets out a few strategies: cut down greenhouse gas emissions by at least 55 % by 2030 compared to the 1990 level [1], increase the fraction of renewable energy by 42.5 % [2] and reduce the primary energy consumption by 32.5 % [3].

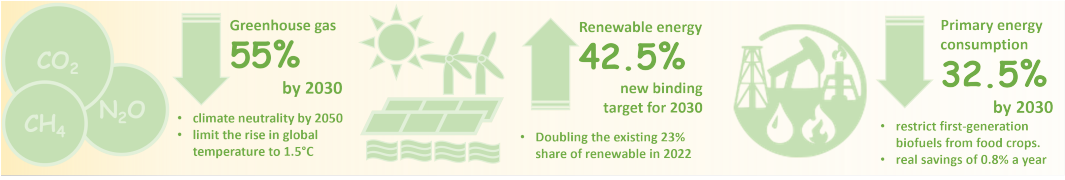


**Figure 1.1:** Roadmap of the EU energy policy.

From the legislated goals above, one could realise that renewable energy plays an essential role as a substitute for fossil-based energy sources. Nonetheless, renewable energy is intermittent, which serves as one of the key challenges that impedes the "Energiewende". To solve this issue, energy storage is planned to not only guarantee a consistent electricity supply but also helps to reduce price fluctuations, which makes renewable energy more attractive to consumers.

Batteries are one of the storage options. Batteries have long existed and their implementations range from small personal electronic appliances to cars, forklifts, or backup energy supplies. Yet, the main challenge faced by batteries are mainly low energy and power densities. In the past two decades, the introduction of lithium-based batteries with higher energy and power densities has pushed the application range towards larger-scale employment such as electromobility and stationary storage in a power grid.

Lithium-ion batteries (LiBs) in particular receive huge attention in response to the worldwide energy transformation. The global consulting firm, McKinsey and Company, projected exponential growth in the worldwide demand for LiBs by about 32 % between 2015 and 2030 with the mobility sector being the major contributor, coming mainly from China, the EU, and the US. Meanwhile, nickel manganese cobalt and lithium iron phosphate are shown to be the most demanded cathode material chemistries for LiBs [4].

Everything comes with a price. As “Energiewende” progresses, the surge in the demand for LiBs will lead to a higher demand for raw materials such as lithium and transition metals, which later results in environmental issues due to the excessive mining of the required minerals in return. Hence, efforts such as enhancing the lifespan of LiBs or closing the life cycle of the battery via recycling are examples of significant focuses in the current battery research.

The development of new battery materials and optimised battery designs with high energy and power densities, which are also stable under dynamic operating conditions have been intensively researched in the past few years. The battery is a closed system. The changes in the internal states concerning different chemistries and operating conditions are hardly measurable. Thus, its internal states can only be predicted and characterised via external current and voltage measurements — electrochemical impedance spectroscopy (EIS).

EIS delivers information about the interfacial properties related to the internal states of the batteries by measuring the battery’s response under small alternating current or voltage perturbation at different frequencies. In EIS, the battery state is moderately perturbed so that the battery’s responses are contained in the quasi-linear regime, which results in information loss as batteries are known to be inherently nonlinear. This motivates us to extend the analysis towards the nonlinear characterisation technique — nonlinear frequency response analysis (NFRA).

NFRA is an advanced version of EIS. The working principle is almost similar to EIS, except that a larger perturbation signal is applied to excite additional nonlinear information in the form of harmonics. Prior studies have shown the superiority of NFRA against EIS in terms of better process identification, access to additional kinetic information on charge transfer symmetry, and identification of lithium plating. The first model-based NFRA assessment has also been conducted, which provides the basic idea of the sensitivity of different battery parameters on the harmonics.

Ageing is an important aspect and unavoidable in LiBs as they are often operated outside the stable working potential windows. Ageing not only deteriorates the battery’s performance but could also trigger safety issues. An accurate assessment of the battery’s ageing is therefore essentially critical to analyse the ageing behaviour, quantify and predict the ageing extent, as well as detect any premature ageing in the batteries. Hence, NFRA is a potential tool to serve this purpose as it depicts the battery’s behaviour in a bigger picture.

The main objective of this thesis is to investigate the ageing of LiBs via this new metrology - NFRA. Specifically in this thesis, I would like to demonstrate how NFR signals can be correlated to battery ageing and be used to quantify the remaining useful life of the battery. Furthermore, I would also like to explore the possibility of NFRA to offer additional meaningful information as compared to the conventional EIS method.

# 2 Fundamentals and Thesis Scope

Batteries have a long-standing history. Since the invention of the Volta battery until today's widely commercialised LiBs, battery technology has been evolving rapidly. Ever since a variety of batteries has been presented from the technological advancement. Among all, LiBs emerge as the most attractive one: LiBs offer high energy and power densities as lithium is the lightest and smallest alkali metal.

In this chapter, I am going to show the basic structure and the working principle of LiBs. On that basis, I explore the ageing behaviours that are typically shown by LiBs. Also, the state-of-the-art of battery modelling approaches will be shortly discussed and compared. Lastly, the linear and nonlinear frequency response analysis, which serve as the research focus for the ageing analysis later, will be introduced and their use cases in the prior work will be presented.

## 2.1 Terminology

Before delving further, it is essential to introduce and define the key terminology used throughout this thesis.

**Capacity**
Capacity describes the amount of electric charge that is stored in the battery; alternatively, it represents the amount of current that can be delivered by the battery over a period of time. It is usually measured in ampere-hours (Ah).

**C-rate**
C-rate defines the speed of the battery charging or discharging and the rate is measured with reference to the battery capacity. For example, 1C indicates that the battery fully charges and discharges in 1 hour; at 0.5C, the battery needs double the time as 1C, which is then equivalent to 2 hours, to fully charge and discharge.

**State-of-Charge (SoC)**
SoC describes the amount of charge that is available in the battery at a certain time step with reference to the maximal amount of charge that can be held by the battery. SoC is usually given in percent,

ranging from 0 % to 100 %. SoC 0 % represents that the battery is completely discharged; SoC 100 % indicates that the battery is fully charged.

**State-of-Health (SoH)**
SoH compares the change in the maximal amount of charge that can be held by the battery during ageing with reference to the initial. Similar to SoC, SoH ranges from 0 % to 100 %: SoH 0 % means that the battery has no more useable capacity while the battery with SoH 100 % is at a pristine state before usage. Accordingly, SoH 50 % indicates that the battery has lost 50 % of its initial capacity.

**Positive/negative electrode vs. cathode/anode**
In electrochemistry, "cathode" is usually used to designate the electrode, where the reduction reaction occurs while "anode" indicates the electrode, where the oxidation reaction takes place. However, in rechargeable batteries, those reactions take place interchangeably at the two electrodes depending on the charge or discharge directions. Therefore, it is confusing to use these wordings to define the electrode precisely.
A better terminology is selected here, which defines the electrodes based on the potential level: "positive electrode" instead of "cathode" is used to indicate the electrode with a higher potential level such as the electrode that typically uses transition metal oxide. Meanwhile, "negative electrode" defines the electrode with a lower potential level, in this case, it is the carbonaceous electrode.

**Open circuit voltage (OCV)**
OCV indicates the electrical potential difference between two electrodes in an electrochemical cell, for example, a battery, when it is disconnected to a load or in other words, there is no current flowing through the cell.

## 2.2 Lithium-ion batteries

LiBs are units that store electrical energy in the form of chemical energy and transform it during discharge from chemical to electrical energy. The conversion between chemical and electrical energy is governed by reversible electrochemical reactions, mainly involving lithium ions as the name suggests. Upon charge, lithium is oxidized at the positive electrode and travels to the negative electrode for the subsequent reduction. Reversibly, lithium is released from the negative electrode and reduced at the positive electrode during discharge. While lithium ions shuttle between the negative and the positive electrodes via the electrolyte, the electrons travel through the external circuit, creating a current flow. A separator is placed in between negative and positive electrodes to prevent direct contact between both electrodes and thus, preventing short-circuit of the battery.

The general structure of LiBs is depicted in Figure 2.1. As shown, LiB is mainly composed of a negative electrode, a positive electrode, a separator, electrolyte, and current collectors. There are also other additives such as binder and carbon black to improve the contact resistance and electrical

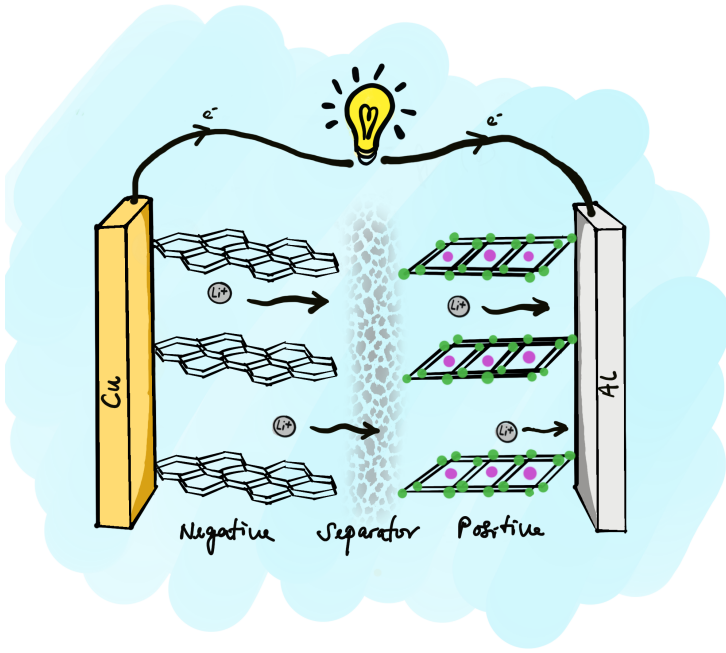


**Figure 2.1:** Lithium-ion battery structure.

conductivity, which are not shown in the figure. Batteries utilize the working potential difference at two electrodes to generate electrical energy, and the potential difference highly depends on the electrode materials. A stronger working potential difference by different electrode materials results in a larger energy that can be withdrawn from the batteries. Apart from that, particularly in LiBs, the negative and the positive electrodes must also possess the ability to reversibly host and release lithium ions during charge and discharge.

Typical negative electrode materials used nowadays are carbonaceous materials, which were introduced and commercialised by Sony for the first time in 1991 [5]. Since then, carbonaceous materials such as graphite, hard, and soft carbon have achieved huge success as they allow reversible intercalation of lithium ions and at the same time, offer a large gravimetric capacity of about $372\,\mathrm{mAh\,g^{-1}}$ [6]. Most importantly, they are much safer as compared to the predecessor — lithium metal. Recently, silicon oxide composite has been added to the carbonaceous negative electrode to enhance its capacity [7]. Another negative electrode material such as lithium titanium oxide has been introduced as well.

A large pool of positive electrode materials has been researched and used in LiBs in the past decades. Among those that survive today are transition metal oxides [5]. Three main groups of transition

metal oxides can be classified, which differ concerning their crystal structures: layered, spinel and olivine structures [8]. These structures aim to host and release lithium ions in an orderly manner and to hold as much lithium as possible. This leads to a higher capacity in return. Common examples of transition metal oxides are lithium cobalt oxide (layered), lithium nickel manganese cobalt oxide (layered), lithium manganese oxide (spinel), and lithium iron phosphate (olivine) [9, 10].

Meanwhile, electrolyte should show good wetting properties that favour interfacial reaction, good ionic properties for the facile transport of lithium ions, and promising stability under a wide range of operating conditions [11]. Organic carbonate-based electrolyte appears to be a suitable candidate that fulfils this purpose. Examples of carbonate electrolyte are ethylene carbonate, ethyl methyl carbonate, and dimethyl carbonate. In conjunction with this, the typical conducting salt used in LiBs is lithium hexafluorophosphate or similar to facilitate the transport of lithium ions through the electrolyte [12]. Often, different fractions of different carbonate electrolytes are combined and implemented in LiBs to complement each other's inadequacies. Commonly, additives such as vinylene carbonate are added to the electrolyte to increase the stability of the electrolyte, thus prolonging the lifespan of LiBs [13]. Advance development has brought forward the discovery of polymer and solid-state electrolytes [14, 15].

## 2.3 Ageing of lithium-ion batteries

Ageing is inevitable in LiBs, and the electrolyte is mainly responsible for it. This is because electrolyte generally exhibits a narrow electrochemical stability window, which favours the onset of electrolyte decomposition as soon as it comes in contact with the electrodes [16]. Accompanied by it, a fraction of lithium ions that shuttle between the negative and the positive electrode are immobilised, thereby reducing the battery capacity. At the same time, the deposition of the decomposition product on the electrode surface increases the interfacial resistance, which results in a decrease in the overall battery efficiency. In this thesis, I focus on the ageing mechanism of the graphitic negative electrode and transition metal oxides as the positive electrode, particularly lithium nickel manganese cobalt oxides (NMC).

On the graphite surface, the electrolyte is reduced together with lithium ions, forming an interfacial layer known as the solid-electrolyte interphase (SEI) [17]. The formation of the SEI usually takes place in the first few cycles and is needed to avoid direct contact between graphite and electrolyte, therefore, preventing further electrolyte reduction. An ideal SEI should be stable and elastic to adapt to the mechanical expansion and contraction of the graphite during charge and discharge, also, most importantly, ionic conductive and electrical insulating [18]. However, the real SEI does not seem to manifest these properties, leading to continuous SEI growth. In reality, the formed SEI is heterogeneous and composed of two layers: the compact inner inorganic SEI layer (close to the negative electrode surface), consisting of products from the decay of conducting salts, and the porous outer

organic SEI layer with its constituents, coming from electrolyte decomposition [19]. The porous SEI allows the penetration of electrolyte, leading to further SEI growth while the dense SEI permits growth mechanisms due to electron tunnelling [20] and radical electron transfer [21].

Elevated temperature aggravates the SEI growth [17]. Conversely, lower temperature favours lithium plating even at low SoC [22]: Instead of inserting into the negative electrode, lithium ions accumulate during charging on the negative electrode surface due to the sluggish interfacial as well as diffusion kinetics. As a result, lithium ions reduce and deposit on the negative electrode surface, forming patches of lithium metal. Since lithium metal is highly reactive, it further reacts with the surrounding electrolyte and forms an additional SEI layer on top of the plated lithium [23]. A similar phenomenon can also be observed during fast charging with a high current [24]. In connection with this, a high current load could also lead to exfoliation [25] and micro-cracking within graphite [26].

For NMC, on the other side, an interfacial layer is similarly formed due to electrolyte oxidation. This interfacial layer is commonly known as the cathode-electrolyte interphase (CEI) [27]. Till today, the composition and mechanisms of CEI growth remain unclear and under debate [28]. Nevertheless, an agreement has been achieved on the structure or morphology of CEI, which suggests that CEI is entirely porous and allows NMC access to the electrolyte, giving rise to the name solid permeable interphase (SPI) by some other research groups [29].

Alongside electrode oxidation, the electrolyte impurity — water, hydrolyses conducting salt, forming an extremely reactive hydrogen fluoride. This acidic compound attacks metal oxides, which results in the dissolution of manganese via a disproportional reaction [30]. It is reported that the dissolved manganese ions will be transported to and deposited at the negative electrode, which eventually accelerates the electrolyte reduction and catalyses the SEI growth [31].

Apart from the above degradation mechanisms, NMC is also known for its structural instability, especially at the high-voltage window during charge. Cation mixing between nickel and lithium ions due to their comparable ionic radii triggers the migration of nickel ions into the energetically favourable lithium vacancies [32]. The migration is then associated with a phase transformation from layered to disordered spinel and finally to rock-salt structure [33]. The rock-salt structure has poor kinetic, resulting in high interfacial resistance [34]. In the worst case, phase transformation is accompanied by oxygen release, which is detrimental to the safety of LiBs [33]. Meanwhile, micro-cracking is also commonly observed in NMC ageing.

In addition to the negative and the positive electrodes degradations, other ageing effects such as delamination of active material from the current collector [35, 36], corrosion of current collectors [37, 38], and degradation of the binder [39] are also reported as possible causes for LiBs ageing.

Overall, all the above-listed ageing mechanisms impact LiBs differently, in the end, leading to a reduction in battery capacity and efficiency. Their corresponding impacts due to the different ageing mechanisms are illustrated in Figure 2.2.

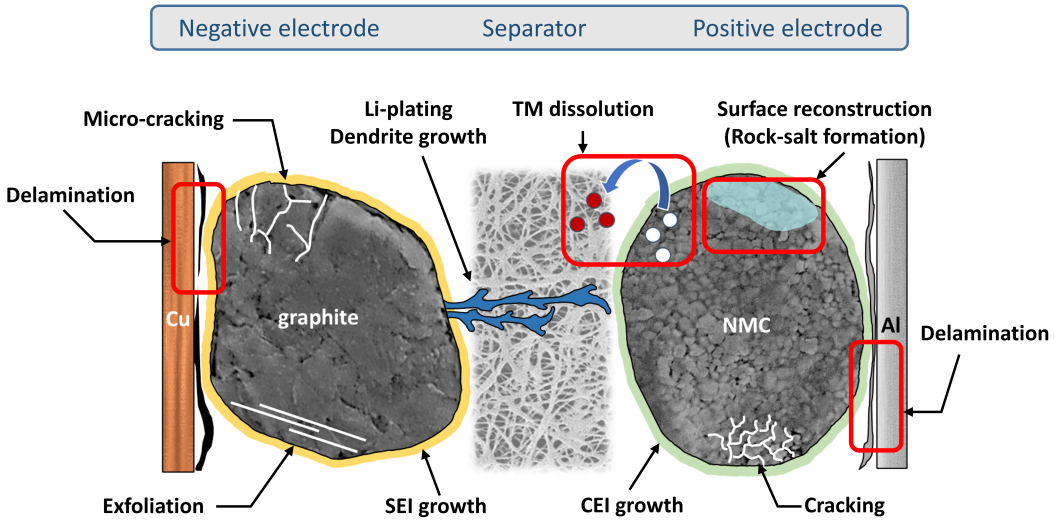


**Figure 2.2:** Ageing mechanism in LiB.

## 2.4 State-of-the-art lithium-ion battery modelling

Battery modelling targets to provide a fundamental understanding of the electrochemical processes in LiBs. A battery model captures the physics of electrochemistry in batteries to simulate the battery behaviour under defined operating conditions. By mapping the simulated battery behaviour with the characteristics in reality, the model parameters can be correlated to the internal states of LiBs. These model parameters could later serve as the indicator or predictor of the battery performance: SoC and SoH. Further, battery models can also be used to optimise battery design for specific real-life applications, for example, fast charging.

Comprehensive battery modelling approaches have been demonstrated in the past decades, which serve different purposes or applications. The battery model in general ranges from comprehensive multiphysics and multiscale models, to simplified equivalent circuit models and data-driven empirical modelling that requires no knowledge of the battery chemistries as shown in Figure 2.3.

The empirical approach derives a correlation to describe the observation on the data set via a simple mathematical expression without involving a theoretical background. Often, an empirical model demands a large amount of data to lower the calculation variance and enhance the model's accuracy. The established mathematical expression can either be the simple regression method or sophisticated machine learning approaches such as artificial neural network, support vector machine, gaussian approach and many more. Use cases of the empirical model in LiBs are battery design with desired energy density [41], ageing analysis such as prediction of remaining useful life [42, 43] and thermal analysis to design optimised thermal management [44, 45].

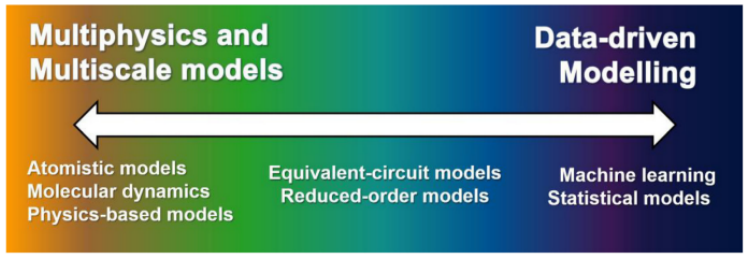


**Figure 2.3:** Battery modelling spectrum [40]. Reprinted from Materials Today, Vol. 49, M. Pang et al., Interactions are important: Linking multi-physics mechanisms to the performance and degradation of solid-state batteries, Pg. 145-183, Copyright 2023, with permission from Elsevier.

Next, the equivalent circuit model (ECM) belongs to the semi-empirical model. Compared to the empirical model, the semi-empirical model does not entirely depend on data but partially attains a simplified physical background with approximations. For example, the ECM approach only considers the linear behaviour of batteries. ECM uses electronic circuit components to replicate the behaviour of LiBs [46]. To date, different types of ECMs exist (Rint, Thevenin, PNGV models), which attempt to provide a better depiction of the internal processes as well as degradation in LiBs [47]. They differ in terms of complexities in the circuit connection and the number of electronic circuit components involved. ECM is popular for its trade-off between empirical and semi-mechanical advantages — fast computing while it does not lose significant physical insights in LiBs. Previously, ECM has shown its potential mainly in battery state estimation, which is especially useful in the battery management system (BMS) [47–49].

Rather than describing the data set in the same way as the empirical approach, the electrochemical multiphysics model uses a mathematical approach to illustrate the underlying physico-chemical processes in LiBs. Although this mechanistic approach is comparably computationally expensive and complicated to establish, it offers more useful in-depth information related to the internal processes in LiBs, i.e., the model parameters have physical meaning. Further, this modelling approach is more flexible in terms of its applicability for a wider operating range (high C-rate, low temperature). Most importantly, the electrochemical multiphysics model can reproduce the nonlinear behaviour of LiBs.

The common electrochemical model for LiBs is known as the Newman Pseudo-Two-Dimensional (P2D) model. The P2D model was first introduced by Newman and Doyle in 1993 [50]. The very first version of the P2D model was based on the porous electrode and concentrated solution theories, incorporating physical transport processes, electrochemical interfacial activities, Ohm's law, and mass and charge conservations [51]. Figure 2.4 shows the visual representation of a P2D model. As the name claims, the P2D model resolves the battery dynamic in two directions. Across the battery thickness, the P2D model considers the electrolyte dynamic, which involves mainly the transport of lithium ions (diffusion and migration) in the electrolyte phase, as well as the electrochemical lithium intercalation and deintercalation reactions at the electrode/electrolyte interphase. Meanwhile, the transport of lithium (solid diffusion) is considered radially within the active material of the electrode.

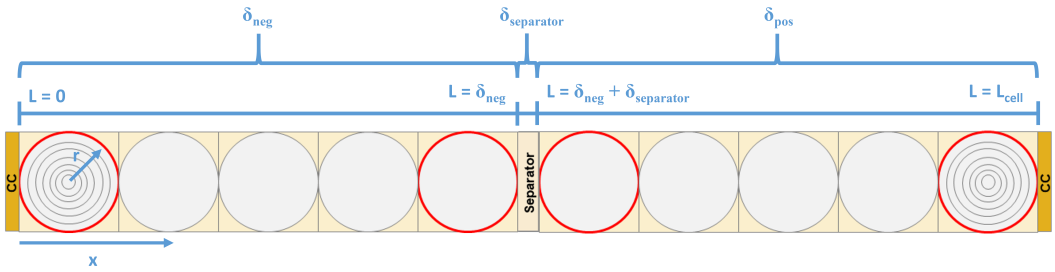


**Figure 2.4:** P2D model.

In the P2D model, the active materials in electrodes are assumed as uniform spherical particles and are identical spatially at every point within the electrode [52]. Further approximations such as negligible concentration and potential gradient in the electrolyte phase further simplify the P2D model to the Single Particle (SP) model [53]. However, the accuracy of the SP model is only limited to low current applications, which is not the focus of this thesis and will not be further detailed.

Several adaptations have been performed on the P2D model to refine the simulation precision of the LiBs' performance. For example, Legrand et al. included double-layer capacitance to describe the charging of interphase before lithium intercalation or deintercalation [54]. This enables the simulation of a semicircle in EIS. In addition, side reactions such as SEI growth and lithium plating have also been taken into account in the P2D model to better depict the ageing behaviour of LiBs.

Extensive modelling approaches for SEI growth have been well-researched and reviewed by Wang et al. [55]. Most of the work modelled the SEI growth as a parasitic current density that competes with lithium intercalation reaction. The corresponding current density for the SEI growth conforms to the Butler-Volmer kinetic, solely differing in the pre-exponential dependency on lithium and solvent concentrations as pointed out by Lawder et al. [56]. The derivation of pre-exponential terms depends on the assumptions made for the different SEI growth modes, i.e., diffusion-limited [57], kinetic-limited [58] and solvent-reduction limited [59]. Additionally, cracking or dissolution of the SEI due to graphite expansion, which accounted for the imperfect SEI growth, is proposed by Kindermann et al. [60]. Kolzenberg et al. [61] and Single et al. [62] also uncovered a second transport mechanism, which involves neutral lithium species travelling from electrode/SEI interphase across the porous SEI for the subsequent SEI reduction reaction with the electrolyte. They found that the SEI growth is first limited kinetically by the formation of lithium and is later limited by the diffusion of lithium and the migration of electrons.

Further, Single et al. derived an analytical solution for the EIS simulation and used an additional parallel resistor-capacitor (RC) circuit component to model the additional semicircle in the EIS [63]. The author described the additional semicircle as due to the ionic impedance of the SEI, which is a function of SEI thickness, conductivity and permittivity. Meanwhile, Heinrich et al. indicated that the arising semicircle originated from the skimming of the solvate shell of lithium-ion upon entering

the SEI layer, which takes place at the additional SEI/electrolyte interphase [64]. The increase in the semicircle is then due to the isolation of active area at both electrode/SEI and SEI/electrolyte interphases, which are in turn depending on the SEI thickness. Later, Witt et al. extended and improvised the model proposed by Heinrich et al. into the P2D model structure [65]. The author expressed the kinetics of the involved interfacial reactions individually via the thermodynamic ansatz and incorporated the transport of lithium ions across the SEI into the proposed model.

Similar to the SEI growth, lithium plating is modelled as concurrent current density to intercalation via the generalized Butler-Volmer kinetic and is only initiated when the negative electrode potential falls below 0 V [66, 67]. Nevertheless, some studies pointed out that the critical plating potential at the negative electrode does not necessarily lie at 0 V but rather depends on the amount of lithium deposition or surface coverage by plated lithium [68–70]. In addition, the charge transfer coefficient for the plating reaction is taken to be deviating from 0.5, which is normally assumed for the case of lithium intercalation reaction. This indicates the irreversibility of the reaction in most of the research works [22, 71, 72]. The interaction and connection between SEI growth and lithium plating are further established in several works [72–74].

So far, all modelling works focus on illustrating the negative electrode degradation. Although the positive electrode is as well known to undergo the dissolution of transition metal, the transformation of rock-salt structure, etc., the inclusion of these degradations in the P2D model is not yet ready or proposed in any current work, to the author's knowledge. This might be because the degradation at the positive electrode is still not well understood or possibly a new model architecture is needed to depict the influence of these degradations on battery performance.

## 2.5 Pseudo-Two-Dimensional (P2D) battery model

Hitherto wide ranges of continuum physical-based battery models have been developed, where one could see a trade-off between modelling accuracy and complexities, befitting different purposes and applications. As mentioned, for the model-based assessment, the P2D model is the most common battery model, which can model the battery behaviour under a wide range of current loads, in particular at high C-rate as it simultaneously can simulate the concentration as well as potential gradient developed within the electrode and electrolyte. In this section, the skeletal structure and the governing equation of the P2D model will be described in detail. Figure 2.4 shows the visual representation of a P2D model. As the name claims, the P2D model resolves the battery dynamic in two directions. Across the battery thickness, the P2D model considers the electrolyte dynamic, which involves mainly the transport of lithium ions (diffusion and migration) in the electrolyte phase, as well as the electrochemical lithium intercalation and deintercalation reactions at the electrode/electrolyte interphase. Meanwhile, the transport of lithium (solid diffusion) is considered radially within the active material of the electrode.

In P2D battery modelling, several simplications are assumed as listed specifically below [50, 51]:

- The cell temperature remains constant and uniform (isothermal),
- the convection in the electrolyte phase is neglected,
- the active material particle is treated as a perfect sphere, and
- the simulation of the electrodes can be approximated as an active material as all the active materials are assumed to be identical in terms of geometry and behave physically and chemically similar.

The governing equations for the P2D model are derived from the conservation laws of species and charge transport. These equations are present in the form of partial differential equations, and each of them describes the states inside the Li-ion battery. These partial differential equations are spatially discretised inside the battery, and then they are solved at every discretised cell for the temporal development of the state variables using the ordinary differential equation solver from `MATLAB`. The governing equations for the P2D model shown in this thesis take reference from the work by Legrand et al. [54].

### 2.5.1 Mass transport

The lithium concentration in the active material spherical particle $c_s$ follows Fick's law, and it can be expressed as

$$\frac{\partial c_s(r)}{\partial t} = \frac{1}{r^2}\frac{\partial}{\partial r}\left(D_s r^2 \frac{\partial c_s(r)}{\partial r}\right) \tag{2.1}$$

where $D_s$ indicates the diffusion coefficient in the solid phase, and r is the spatial discretisation in the direction of the particle's radius. Here, the boundary conditions are defined as no flux at the particle centre ($r = 0$) as shown in Equation 2.2 and the flux at the particle surface ($r = R_s$) is proportional to the interfacial reaction current $j^{Li}$ in Equation 2.3.

$$\frac{\partial c_s(r = 0)}{\partial r} = 0 \tag{2.2}$$

$$\frac{\partial c_s(r = R_s)}{\partial r} = -\frac{j^{Li}(x)}{a_s F D_s} \tag{2.3}$$

Similarly, the concentration of the electrolyte $c_e$ can be described via Fick's law with an additional source term as follows

$$\varepsilon_e \frac{\partial c_e(x)}{\partial t} = \frac{\partial}{\partial x}\left(D_{e,eff}\frac{\partial c_e(x)}{\partial x}\right) + (1-t_p)\frac{j^{Li}(x)}{F} \tag{2.4}$$

where $\varepsilon_e$ is the volume fraction in the electrolyte phase. $D_{e,eff}$ is the effective diffusion coefficient in the electrolyte phase, $t_p$ is the transference number, $j^{Li}$ is the rate of the volumetric $Li^+$ current generation, and F is the Faraday constant. The first term on the right-hand side indicates the diffusion process of the lithium salt ions in the electrolyte phase while the second term describes the generation of the lithium ions at the electrode/electrolyte boundary. At the current collector boundaries ($x = 0, L_{cell}$), it is defined as no lithium-ion flux flowing through the current collectors.

$$\frac{\partial c_e(x = 0, L_{cell})}{\partial x} = 0 \tag{2.5}$$

The diffusion coefficient in the porous phase $D_{e,eff}$ is computed by correcting the diffusion coefficient in the continuous phase of electrolyte $D_e$ with the volume fraction of the electrolyte phase and tortuosity $\tau$.

$$D_{e,eff} = \frac{\varepsilon_e}{\tau} D_e \tag{2.6}$$

The tortuosity can be described via the bruggeman relation as follows

$$\tau = \varepsilon_e^{-\beta} \tag{2.7}$$

with $\beta$ is the bruggeman exponent. Here, a polynomial correlation between the diffusion coefficient in the continuous phase of electrolyte $D_e$ and the ionic concentration in the electrolyte $c_e$ is implemented.

$$D_e = 1.47 \times 10^{-7} \exp(1.33\overline{c_e}) \exp\left(-\frac{1.69 \times 10^3}{T}\right) \exp\left(-\frac{563}{T}\overline{c_e}\right) \tag{2.8}$$

## 2.5.2 Charge transport

Meanwhile, Ohm's law is used to compute the potential in the solid phase $\Phi_s$ as shown below

$$J_s(x) = -\sigma_{s,eff}\frac{\partial \Phi_s(x)}{\partial x} \tag{2.9}$$

$$\frac{\partial J_s(x)}{\partial x} = -j^{Li}(x) - j^{DL}(x) \tag{2.10}$$

where $J_s$ is the current density in the solid phase, $\sigma_{s,eff}$ is the effective electronic conductivity in the solid phase, $j^{Li}$ is the rate of the volumetric $Li^+$ current generation, and $j^{DL}$ is the volumetric rate of double layer current generation. Likewise, the effective electronic conductivity in the porous solid phase $\sigma_{s,eff}$ is approximated by correcting the volume fraction in the solid phase $\varepsilon_s$ with the electronic conductivity in the continuous solid phase $\sigma_s$.

$$\sigma_{s,eff} = \varepsilon_s \sigma_s \tag{2.11}$$

For the electrolyte phase potential $\Phi_e$, Ohm's law is extended with the contribution from the diffusional electronic conductivity $\sigma_{De,eff}$.

$$J_e(x) = -\sigma_{e,eff}(x)\frac{\partial \Phi_e(x)}{\partial x} - \sigma_{De,eff}(x)\frac{\partial \ln(c_e(x))}{\partial x} \tag{2.12}$$

$$\frac{\partial J_e(x)}{\partial x} = j^{Li}(x) + j^{DL}(x) \tag{2.13}$$

with $J_e$ is the current density in the electrolyte phase, $\sigma_{e,eff}$ is the effective electronic conductivity in the electrolyte phase, $c_e$ is the concentration of the electrolyte, $j^{Li}$ and $j^{DL}$ are the rate of the volumetric $Li^+$ current generation as well as the volumetric rate of double layer current generation respectively.

The electronic conductivity in the continuous phase of the electrolyte $\sigma_e$ is adjusted with the volume fraction in the electrolyte phase $\varepsilon_e$ and tortuosity $\tau$, where the tortuosity is determined via the Bruggeman's relation as shown in Equation 2.7.

$$\sigma_{e,eff} = \frac{\varepsilon_e}{\tau}\sigma_e \tag{2.14}$$

In this work, $\sigma_e$ can be deduced from an empirical function that is expressed in terms of the electrolyte concentration $c_e$ and is discretised in the direction of x. The empirical function implemented in this thesis is obtained from [75] based on the electrolyte composition of EC:DMC 1:1 (wt. %).

$$\sigma_e = 0.0798(1 + (T - 228))c_e \frac{1 - 1.22c_e^{0.5} + 0.509\left(1 - 4 \cdot 10^{-3}\exp\left(\frac{100}{T}\right)\right)c_e}{1 + 3.79 \cdot 10^{-3}c_e^4 \exp\left(\frac{1000}{T}\right)} \tag{2.15}$$

The effective diffusional electronic conductivity $\sigma_{De,eff}$ can be expressed in terms of temperature T, transference number $t_p$, and effective electronic conductivity in the electrolyte phase $\sigma_{e,eff}$.

$$\sigma_{De,eff} = 2\frac{RT}{F}(t_p - 0.5)\sigma_{e,eff} \tag{2.16}$$

The boundary conditions for the potential in the solid phase $\Phi_s$ are defined as follows

$$J_s(x = 0, L_{cell}) = \mp\frac{I_{cell}(t)}{A_{cell}} \tag{2.17}$$

$$J_s(x = \delta_{neg}, L_{cell} - \delta_{pos}) = 0 \tag{2.18}$$

with $L_{cell}$ is the cell thickness, $\delta_{neg}$ is the negative electrode thickness, $\delta_{pos}$ is the positive electrode thickness, $I_{cell}$ is the current density and $A_{cell}$ is the cross-sectional area of the cell that is perpendicular to the current density. Meanwhile, the boundary conditions for the potential in the electrolyte phase $\Phi_e$ are defined as

$$\frac{\partial\Phi_e(x = 0)}{\partial x} = \frac{\partial\Phi_e(x = L_{cell})}{\partial x} = 0 \tag{2.19}$$

### 2.5.3 Butler-Volmer equation

The rate of the interfacial reaction, i.e., volumetric $Li^+$ current generation at the electrode/electrolyte boundary $j^{Li}$ can be described via Butler-Volmer kinetic.

$$j^{Li} = j_0 a_s[\exp(\frac{\alpha F\eta}{RT}) - \exp(-\frac{(1-\alpha)F\eta}{RT})] \tag{2.20}$$

$a_s$ indicates the active surface per unit volume in the solid phase. It is expressed as the ratio of the volume fraction in the solid phase $\varepsilon_s$ and the radius of the active material particle $R_s$.

$$a_s = \frac{3\varepsilon_s}{R_s} \tag{2.21}$$

The exchange current density $j_0$ is a function of rate constant $k_0$, chemical potential $\Delta G^0$, SoC $X_{Li(s)}$, the activity of lithium-ion in electrolyte phase $a_{Li^+(e)}$, maximum lithium concentration $c_{max}$ in the active material particle, and charge transfer coefficient $\alpha$.

$$j_0 = k_0 \exp\left(-\frac{\Delta G^0 \alpha}{RT}\right) Fc_{max}(1 - X_{Li(s)})^{\alpha} a^{\alpha}_{Li^+(e)} X^{(1-\alpha)}_{Li(s)} \tag{2.22}$$

The surface overpotential $\eta$ describes the potential difference between the electrode $\Phi_s$ and the electrolyte phases $\Phi_e$ as well as the electrode equilibrium potential $E^{eq}$.

$$\eta = \Phi_s - \Phi_e - E^{eq} \tag{2.23}$$

The electrode equilibrium potential $E^{eq}$ depends on the chemical potential and activities of lithium-ion in the electrode $a_{Li(s)}$ and occupancy site $a_{V(s)}$.

$$E^{eq}_{pos} = \frac{\Delta G^0}{F} + \frac{RT}{F} \ln\left(\frac{a_{V(s)}}{a_{Li(s)}}\right) \tag{2.24}$$

The activities of the species are then empirically computed via the following expressions with $A_m$ is the fitted redlich-kister parameter [76].

$$\ln a_{Li(s)} = \frac{1 - X^2_{Li(s)}}{RT} \sum_{m=0}^{N} A_m (2X_{Li(s)} - 1)^m \left(1 + \frac{2mX_{Li(s)}}{2X_{Li(s)} - 1}\right) \tag{2.25}$$

$$\ln a_{V(s)} = \frac{X^2_{Li(s)}}{RT} \sum_{m=0}^{N} A_m (2X_{Li(s)} - 1)^m \left(1 - \frac{2m(1 - X_{Li(s)})}{2X_{Li(s)} - 1}\right) \tag{2.26}$$

### 2.5.4 Double layer capacitance

In conjunction with the rate of the volumetric $Li^+$ current generation due to charge transfer reaction $j^{Li}$, the volumetric rate of double layer current generation $j^{DL}$ is used to describe charges stored at the electrode/electrolyte boundary.

$$j^{DL} = a_s C^{DL} \left(\frac{\partial(\Phi_s - \Phi_e)}{\partial t}\right) \tag{2.27}$$

where $C^{DL}$ is the surface double layer capacitance.

### 2.5.5 SEI model

On top of that, the P2D model is further extended with the SEI layer at the negative electrode to additionally consider the interfacial kinetic overpotential and transport losses through the SEI. There have been several versions of the SEI modelling in LiB. Here, the SEI model framework proposed by Witt et al. is implemented [65]. In the selected model framework, the implementation of the SEI modelling into a P2D model not only introduces an additional interfacial process besides the charge transfer process, i.e., the adsorption/desorption process at the interphase between the SEI layer and electrolyte but also transport through the SEI. A graphical illustration of the implemented P2D-SEI model is depicted in Figure 2.5.

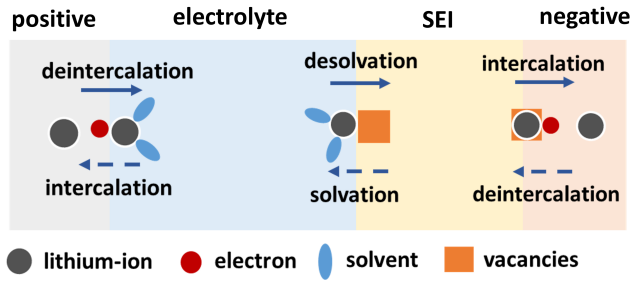


**Figure 2.5:** Graphical illustration of the P2D-SEI model by Witt et al. [65]

At the negative electrode, a lithium atom is first reversibly deintercalated from the active material and combined with a vacancy $V_{Li}(neg/SEI)$ at the interphase between the negative electrode and the SEI layer (neg/SEI), becoming a lithium-ion and leaving a vacancy $V_{Li}(neg)$ in the negative electrode:

$$Li(neg) + V_{Li}(neg/SEI) \rightleftharpoons Li^{+}(neg/SEI) + V_{Li}(neg) + e^{-}(neg)$$

Unlike the Butler-Volmer equation that is used to describe reaction kinetics in the P2D model, the de-/intercalation process is described with a more generalized approach via separate forward and backward reaction rates [76].

$$j^{Li}_{neg/SEI} = a_{s,neg} F \Gamma_{neg/SEI} \left[ a_{Li(neg)} (1 - \theta_{neg/SEI}) k_{f,neg/SEI} - a_{V_{Li}(neg)} \theta_{neg/SEI} k_{b,neg/SEI} \right] \tag{2.28}$$

where $a_{s,neg}$ is the specific surface area of the negative electrode, $a_{Li(neg)}$ and $a_{V_{Li}(neg)}$ are the activities of lithium atom and vacancy in the negative electrode, $\Gamma_{neg/SEI}$ and $\theta_{neg/SEI}$ are the maximum surface coverage and the coverage degree at the neg/SEI interphase. $k_{f,neg/SEI}$ and $k_{b,neg/SEI}$ are the reaction rates of the de-/intercalation process, which can be computed as

$$k_{f,neg/SEI} = k_{0,neg/SEI} \exp\left(-\frac{E_{a,neg/SEI}}{RT}\right) \exp\left(\frac{\alpha_{neg/SEI} \Delta\Phi_{neg/SEI} F}{RT}\right) \tag{2.29}$$

$$k_{b,neg/SEI} = k_{0,neg/SEI} \exp\left(-\frac{E_{a,neg/SEI} - \Delta G^0_{neg/SEI}}{RT}\right) \exp\left(-\frac{(1-\alpha_{neg/SEI}) \Delta\Phi_{neg/SEI} F}{RT}\right) \tag{2.30}$$

$$\Delta G^0_{neg/SEI} = \mu^0_{Li^+(neg/SEI)} + \mu^0_{V_{Li}(neg)} + \mu^0_{e^-(neg)} - \mu^0_{Li(neg)} - \mu^0_{V_{Li}(neg/SEI)} \tag{2.31}$$

with $k_{0,neg/SEI}$ is the rate constant of the de-/intercalation rate constant, $E_{a,neg/SEI}$ is the activation energy for the de-/intercalation process. $\Delta G^0_{neg/SEI}$ is the Gibbs free energy, which is the sum of chemical potential $\mu^0_i$ of the involved species i, $i \in \{Li(neg), V_{Li}(neg/SEI), Li^+(neg/SEI), V_{Li}(neg), e^-(neg)\}$, $\alpha_{neg/SEI}$ is the charge transfer coefficient for the de-/intercalation process and $\Delta\Phi_{neg/SEI}$ is the potential difference at the neg/SEI interphase. $\Delta\Phi_{neg/SEI}$ can be computed via the double layer capacitance $C^{DL}_{neg/SEI}$ as shown below.

$$C^{DL}_{neg/SEI} \frac{\partial \Delta\Phi_{neg/SEI}}{\partial t} = \frac{j^{tot} - j^{Li}_{neg/SEI}}{a_{s,neg}} \tag{2.32}$$

At the second interphase, lithium-ion is reversibly desorbed from the SEI layer into the electrolyte (SEI/e), leaving a vacancy $V_{Li}(SEI/e)$ at the SEI.

$$Li^+(SEI/e) \rightleftharpoons V_{Li}(SEI/e) + Li^+(e)$$

Similarly, the adsorption/desorption process is described via forward and backward reaction rates with

$$j^{Li}_{SEI/e} = a_{s,neg} F \Gamma_{SEI/e} \left[\theta_{SEI/e} k_{f,SEI/e} - a_{Li^+(e)} (1 - \theta_{SEI/e}) k_{b,SEI/e}\right] \tag{2.33}$$

where $\Gamma_{SEI/e}$ and $\theta_{SEI/e}$ are the maximum surface coverage and the coverage degree at the SEI/e interphase, $k_{f,SEI/e}$ and $k_{b,SEI/e}$ are the adsorption/desorption reaction rates. The reaction rates can be then described via

$$k_{f,SEI/e} = k_{0,SEI/e} \exp\left(-\frac{E_{a,SEI/e}}{RT}\right) \exp\left(\frac{\alpha_{SEI/e} \Delta\Phi_{SEI/e} F}{RT}\right) \tag{2.34}$$

$$k_{b,SEI/e} = k_{0,SEI/e} \exp\left(-\frac{E_{a,SEI/e} - \Delta G^0_{SEI/e}}{RT}\right) \exp\left(-\frac{(1-\alpha_{SEI/e})\Delta\Phi_{SEI/e}F}{RT}\right) \tag{2.35}$$

$$\Delta G^0_{SEI/e} = \mu^0_{V_{Li^+(SEI/e)}} + \mu^0_{Li^+(e)} - \mu^0_{Li^+(SEI/e)} \tag{2.36}$$

with $k_{0,SEI/e}$ is the rate constant of the adsorption/desorption rate constant, $E_{a,SEI/e}$ is the activation energy for the adsorption/desorption process. $\Delta G^0_{SEI/e}$ is the Gibbs free energy, which is computed from the chemical potential $\mu^0_i$ of the involved species i, $i \in \{Li^+(SEI/e), V_{Li}(SEI/e), Li^+(e)\}$. $\alpha_{SEI/e}$ is the charge transfer coefficient for the adsorption/desorption process. $\Delta\Phi_{SEI/e}$ is the potential difference at the SEI/e interphase, which is calculated via

$$C^{DL}_{SEI/e} \frac{\partial \Delta\Phi_{SEI/e}}{\partial t} = \frac{j^{tot} - j^{Li}_{SEI/e}}{a_{s,neg}} \tag{2.37}$$

The transportation of a lithium-ion through the SEI layer is governed by diffusion and migration processes depending on the surface coverage difference between two interphases, i.e., SEI/e and neg/SEI, with $D_{Li,SEI}$ is the diffusion coefficient of lithium-ion across SEI layer, $d_{SEI}$ is the SEI layer thickness and $t_{p,SEI}$ is the transference number of lithium-ion in SEI layer.

$$\dot{n}_{negSEI/SEIe} = -D_{Li,SEI}\, a^2_{s,neg} \frac{\Gamma_{SEI/e}\theta_{SEI/e} - \Gamma_{neg/SEI}\theta_{neg/SEI}}{d_{SEI}} + \frac{t_{p,SEI}}{F} j^{tot} \tag{2.39}$$

For simplicity, the same specific surface area $a_{s,neg}$ is implemented at both interphases due to the negligible small SEI thickness as compared to the particle radius, and no spatial discretization in the SEI layer is implemented in this case. The derivative of the surface coverages of the two interphases can be computed via the species balance, i.e., lithium flux from diffusion and migration across the SEI layer $\dot{n}_{negSEI/SEIe}$ as well as lithium flux that de-/intercalate from the active material $r_{neg/SEI}$ or lithium flux that adsorbed/desorbed from the SEI interphase $r_{SEI/e}$,

$$a_{s,neg}\Gamma_{neg/SEI} \frac{\partial \theta_{neg/SEI}}{\partial t} = r_{neg/SEI} - \dot{n}_{negSEI/SEIe} \tag{2.40}$$

$$a_{s,neg}\Gamma_{SEI/e} \frac{\partial \theta_{SEI/e}}{\partial t} = \dot{n}_{negSEI/SEIe} - r_{SEI/e} \tag{2.41}$$

Lastly, the total charge transport through the SEI is computed via the following equation with $\kappa_{SEI}$ as the ionic conductivity of the SEI layer,

$$j^{tot} = \frac{\kappa_{SEI}}{a_{s,neg} d_{SEI}} \left( \frac{RT(1-2t_{p,SEI})}{F} \ln\left( \frac{\theta_{neg/SEI}}{\theta_{SEI/e}} \right) - \Delta\Phi_{SEI} \right) \tag{2.42}$$

### 2.5.6 Contact resistance

In addition, the phenomenon of contact resistance between active materials as well as between active material and current collector has been often identified as a semicircle at the high-frequency region in the EIS as proposed by Gaberšček et al. [77]. Thus, for a meaningful cell diagnosis, the modelling of these contact resistances is also included in the SEI extended P2D model, which is then generalised as follows:

$$C_{cc}^{DL} \frac{\partial \Delta\Phi_{cc}}{\partial t} = \frac{I_{cell}(t)}{A_{cell}} - \frac{\Delta\Phi_{cc}}{R_{cc}} \tag{2.43}$$

where $C_{cc}^{DL}$ and $\Delta\Phi_{cc}$ are the double layer capacitance and potential drop at the interphase, where contact resistance presents while $R_{cc}$ is the contact resistance,

With the extended P2D-SEI model, it is thereby possible to precisely model the behaviour of LiBs not only under static load such as charging or discharging at different C-rates, but also simulate the dynamic behaviour of LiBs under sinusoidal excitation at different frequencies. The investigation of the dynamic behaviour of LiBs is more informative than static ones as it is able to distinguish the complex interaction of different processes in the LiBs. This type of dynamic analysis method is known as the frequency response analysis method. Different types of frequency response analysis such as EIS and NFRA will be detailed in the upcoming section.

## 2.6 Electrochemical Impedance Spectroscopy

EIS is a compelling electrochemical characterisation technique, which is typically used to probe the interfacial properties of a material. Via EIS, the impedance behaviour of a system is measured using small perturbation as shown in Figure 2.6. According to Linear System Theory, impedance is a frequency response function describing the relation between voltage and current. To ensure the validity of EIS, the preconditions proposed under Linear System Theory have to be fulfilled [78, 79]. First, the investigated system must be in a steady state and stable, meaning that the system must return to its initial state after the perturbation has been removed. Second, the causality relation must hold, e.g. the system must not exhibit any responses before any perturbation is applied. Third, the response of the system must be linear and describable via the superposition principle.

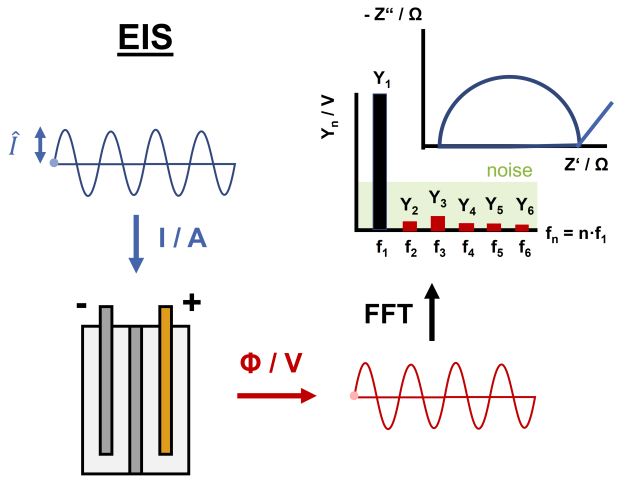


**Figure 2.6:** Working principle of EIS.

Probing EIS over a wide frequency range enables the identification and analysis of interfacial reactions at different time constants. The interpretation of EIS is challenging without a proper model. ECM offers a simple approach to analysing the EIS spectrum. However, the ECM approach is ambiguous as the modelling of the EIS feature is not only restricted to a singular electric circuit but rather open to multiple possible circuit connections [80]. Therefore, the electrochemical model compensates for these drawbacks, providing more physically meaningful insights into the investigated system [81]. The EIS technique has been applied mainly to inspect the interfacial properties such as coating quality [82, 83], corrosion analysis [84, 85], conducting polymer [86, 87], semiconductor [88], biosensors [89], electrochemical processes at electrode/electrolyte interphase as well as the corresponding degradation study in batteries and fuel cells [90–92].

Worth noting, that the Distribution of Relaxation Time (DRT) technique has been introduced in conjunction with EIS. As compared to EIS, DRT is superior in deconvoluting processes with almost similar time constants, which are hardly distinguishable via conventional EIS. Via DRT, the EIS spectrum is fitted via the following expression [93],

$$Z_{DRT} = R_{\infty} + \int_{-\infty}^{\infty} \frac{\lambda(\ln\tau)}{1+j\omega\tau} d\ln\tau \tag{2.44}$$

in which $R_{\infty}$ describes the ohmic resistance, added with a sum of infinite parallel RC circuits. Tikhonov's regularisation approach is commonly used to solve the ill-posed problem mainly arising from the second term in the expression above [94, 95]. This leads to the introduction of the regularisation parameter $\lambda$, which affects the resolution and accuracy of the DRT calculation. The impact of regularisation parameters on DRT computation as well as the identification of optimised

regularisation parameters has been extensively studied [96–98]. Anyhow, information that can be accessed via EIS is still limited as many processes in the battery are nonlinear.

## 2.7 Nonlinear Frequency Response Analysis

NFRA is an extension to EIS. Unlike EIS, NFRA studies the nonlinear information of a system that is excited under a moderately large perturbation (see Figure 2.7). In recent years, NFRA has gained popularity in the electrochemistry field as it allows a comprehensive system analysis. Nevertheless, the interpretation or representation of the information gained from this nonlinear technique has not reached a consensus in the community.

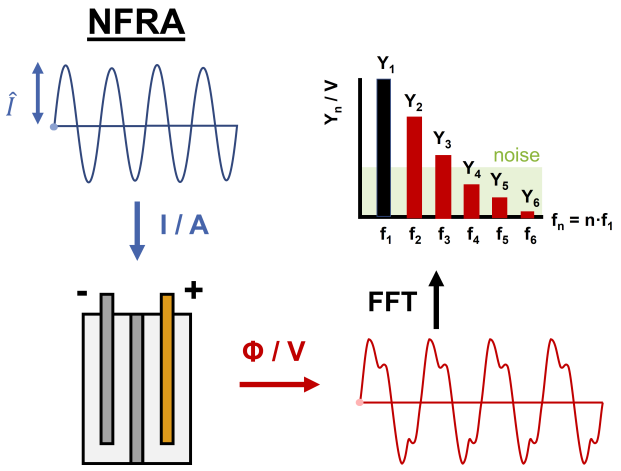


**Figure 2.7:** Working principle of NFRA.

A thorough review of this nonlinear method especially in the electrochemical system has been reported in [99]. Vidaković-Koch et al. mentioned the different terms of the nonlinear technique regardless of the same measurement principle [99]. For example, total harmonic distortion (THD) collates all harmonic signals and refers them to the fundamental harmonic. Nonlinear electrochemical impedance spectroscopy (NLEIS) and NFRA analyse the individual harmonic signals by constraining the extent of input excitation, which is not the case for total harmonic distortion. In contrast, NLEIS portrays harmonics in the form of nonlinear impedance, nonetheless, impedance has only physical meaning at the fundamental frequency, which makes the term impedance for nonlinear interpretation inappropriate. NFRA, on the other hand, considers the full nonlinear responses, including nonlinear contribution at fundamental frequencies as well as at harmonic frequencies. While the above methods take in input excitation at a single frequency at one time, excitation at multiple frequencies is

shown to be also feasible for nonlinear analysis, known as intermodulation differential immittance spectroscopy [100].

The applications of nonlinear analysis have been shown in prior works. An extensive review of the nonlinear analysis has been outlined by Vidaković-Koch [99] and the following are some examples from the author's publication. Bensmann et al. showed that better model discrimination for methanol oxidation kinetic could be achieved, in particular, the second-order frequency response function of NFRA is shown to be sensitive and unique to a different operating parameter that affects the kinetic of different reaction steps [101]. Vidaković-Koch [102] and Panić et al. [103] with the help of NFRA indicated harmonic signals show stronger parameter sensitivity as compared to linear response and the nonlinear signals mainly originate from charge transfer and mass diffusive processes. Further, Živković et al. disclosed linear approach is insufficient to describe the kinetic of oxygen reduction reaction under a highly alkaline medium and additionally, showed that the second-order frequency response function of NFRA can be used as an indicator for process intensification [104]. Interesting insights into NFRA in proton-exchange membrane fuel cells have also been shared by Kadyk et al. [105]. The author demonstrated by combining first-order (EIS) and higher-order frequency response functions (NFRA), three faulty modes in the fuel cell, i.e., dehydration, flooding and carbon monoxide poisoning, could be discriminated.

Other than interpreting the frequency response function of NFRA, Harting et al. analysed the amplitude of the harmonics arising from the LiBs. The author showed that NFRA is a powerful tool in process identification [106] and lithium plating detection [107], which is not accessible via EIS. Also, NFRA is capable of predicting the SoH of LiBs [108, 109]. A simulative investigation has been carried out by Wolff et al., highlighting the importance of NFRA measurement at steady-state [110]. In addition, the author performed a model-based assessment on LiBs via NFRA [111] and further provided a detailed fundamental analysis of the NFRA approach, indicating that the second harmonic is unique for the charge transfer asymmetry [112]. Similar findings were also reported by Murbach et al. [113, 114] but termed differently as NLEIS. While Wolff et al. mainly used FFT to extract the harmonic information from the raw output signals, Murbach et al. explicitly derived analytical expressions for the harmonic signals, revealing the parameter dependency of the second and third harmonics based on the P2D model [113]. By this means, it is shown that the identification of the change in the charge transfer coefficient is only possible via even order harmonics but remains ambiguous via EIS and odd order harmonics.

Apart from NFRA, THD has been implemented in direct methanol fuel cells by Mao et al., where the nonlinear feature in THD is relatable to the reaction kinetics and evolution of intermediate species [115]. Meanwhile, THD is shown to be able to estimate the methanol concentration [116]. Similar to other nonlinear approaches, NLEIS showed supremacy in kinetic discrimination in solid oxide fuel cells [117], unique sensitivity towards charge transfer asymmetry [113, 114], accessibility to thermodynamic properties [118, 119] and diffusivity nonlinearities by second harmonics and additional parameter sensitivity in LiBs [114].

## 2.8 EIS and NFR simulation architecture in electrochemical battery model

Via EIS and NFRA, the battery is periodically excited with either a sinusoidal current signal (galvanostatic mode) or voltage signal (potentiostatic mode). While taking either one as the input signal, e.g., current, the other will be then measured as the output signal, i.e., voltage. By taking the proportion between the output and input signals, one could then obtain information about the impedance (galvanostatic) or admittance (potentiostatic) properties, e.g. amplitude and phase shift. Theoretically, both measurement modes should deliver similar results, i.e., admittance is reciprocal of impedance. Nevertheless, for batteries or any electrochemical system that exhibits low impedance behaviour, the galvanostatic mode is usually recommended. This is because, via galvanostatic mode, one could control and ensure that the amount of current flowing in and out of the system is similar. This is essentially important not only for safety issues but also to avoid the drift in the system state during measurement, which could falsify the measurement result [120]. The drifting phenomenon could be more critical for NFRA as a larger current load is adapted.

Under galvanostatic mode, sinusoidal current signals at different frequencies, as described in Equation (2.45), are input into the battery model in terms of boundary conditions for the potential computation at both electrodes close to the current collector, i.e. $\Phi_s(x = L_{cell})$ and $\Phi_s(x = 0)$), whereby $x = 0 \ldots L_{cell}$ indicates the position of the current collectors in reference to Figure 2.4. The resulting potential difference is termed the output voltage signal of the battery as shown in Equation (2.46).

$$I_{cell}(\omega, t) = \hat{i} \sin(\omega t) = \frac{\hat{i}}{2} \left[ e^{j\omega t} + e^{-j\omega t} \right] \tag{2.45}$$

$$V_{cell}(\omega, t) = \Phi_s(x = L_{cell}, \omega, t) - \Phi_s(x = 0, \omega, t) \tag{2.46}$$

The output voltage signals, arising from every excitation frequency, are sequentially converted from time into the frequency domain through Fast Fourier Transformation, consisting of individual spectral information regarding the voltage signals. The Fast Fourier Transformation is repeatedly probed under multiples of the fundamental excitation frequencies to provide harmonic information of the output voltage signal.

The impedance information is acquired by relating the voltage spectral signals to the input current signals at the respective fundamental excitation frequencies. Combining the corresponding phase shifts, the impedance behaviour of the system can be portrayed as a Nyquist representation. Alternately, NFRA considers directly the harmonic voltage spectral signals. Contrary to impedance, NFRA, in

this work, only accounts for the magnitude of the harmonic voltage spectral signals: $V_1$ is the amplitude of the linear voltage signal at the fundamental frequency $\omega$, $V_2$ and $V_3$ are the amplitudes of the second and third voltage harmonics at a multiple of the fundamental frequency $2\omega, 3\omega$.

$$\begin{aligned} V_{\text{cell}}(\omega,t) = & \underbrace{V_1(\omega,\hat{i})\cdot e^{j\omega t} + V_1(-\omega,\hat{i})\cdot e^{-j\omega t}}_{\text{linear}} \\ & + \underbrace{V_2(2\omega,\hat{i})\cdot e^{j2\omega t} + V_2(-2\omega,\hat{i})\cdot e^{-j2\omega t} + V_3(3\omega,\hat{i})\cdot e^{j3\omega t} + V_3(-3\omega,\hat{i})\cdot e^{-j3\omega t}}_{\text{nonlinear}} \end{aligned} \tag{2.47}$$

$$Z = \frac{V_1}{\hat{i}} \tag{2.48}$$

$$Y_2 = |V_2|, \text{ for } V_2(2\omega,\hat{i}) = V_2(-2\omega,\hat{i}) \tag{2.49}$$

$$Y_3 = |V_3|, \text{ for } V_3(3\omega,\hat{i}) = V_3(-3\omega,\hat{i}) \tag{2.50}$$

## 2.9 Thesis scope

The goal of this thesis is to study the ageing behaviour of LiBs via frequency response analysis. For the ageing study, frequency response analysis involves the commonly used EIS, complemented with the nonlinear approach — NFRA. Through the combination of both linear and nonlinear techniques, this thesis aims to provide a multifaceted understanding of LiBs ageing and, at the same time, to explore the potential of NFRA in discerning additional information regarding ageing behaviour. Lastly, the frequency response analysis is assisted with a model-based approach. The scope and structure of this thesis are outlined as follows:

- *How does NFRA respond to the LiBs ageing as compared to other characterisation methods?*
  In Chapter 3, the ageing behaviour of LiB is assessed using a series of characterisation methods, including EIS and NFRA. This chapter focuses mainly on the phenomenological interpretation of the ageing evolution in EIS and NFR spectra, in particular, to identify any distinctive feature in NFRA, which is different from EIS or other characterisation methods. This chapter serves as an exemplary interpretation as well as the correlation of NFRA to other characterisation methods.

- *Is NFRA able to quantify the ageing?*
  In Chapter 4, the feasibility of ageing quantification via NFRA is explored. For this purpose, the SoH of LiB is predicted using an empirical (black-box) approach, established separately using EIS and NFR data. The derivation of the empirical model is described in more detail in

this chapter. Lastly, the precision and uncertainty of the SoH prediction using EIS and NFRA are discussed and compared.

- *What kind of additional nonlinear information could be extracted via model-assisted study?*
  In Chapter 5, NFRA investigation on LiBs ageing is assisted with a model-based approach. In this regard, Witt's SEI-P2D battery model is extended to enable NFR simulation. With this model, a parameter study is performed to show the uniqueness and sensitivity of NFRA, compared to other electrochemical characterisation methods such as EIS. In addition, the selected battery model is parameterised via multiple electrochemical characterisations, including NFRA.

- *How can the combination of EIS and NFRA help in studying the ageing phenomenon of LiBs via modelling?*
  In Chapter 6, the parameterised model from Chapter 5 will be used in studying LiBs ageing. By reproducing the ageing pattern in EIS and NFR spectra, the temporal development of the model parameters is extracted and studied, which depicts the evolution of the internal states during LiBs ageing.

In the last chapter, the results from the ageing study via frequency response analysis, combined linear and nonlinear approaches, are reviewed and summarised. Finally, open issues and an outlook for future research will be discussed.

# 3 Phenomenological Interpretation of Lithium-ion Battery Ageing [1]

**Research question:** *How does NFRA respond to the LiBs ageing as compared to other characterisation methods?*

This chapter aims to provide a phenomenological analysis of LiB ageing via frequency response analysis. It is essential to examine, how frequency response analysis reacts with ageing behaviour. Ideally, the different ageing features in the frequency response analysis can be distinctively correlated to the different ageing mechanisms, leading to a precise state characterisation of LiBs. In this chapter, the ageing behaviour of LiBs with different particle size distributions at the negative electrode is investigated. As mentioned before, apart from EIS, NFRA is additionally considered. Both EIS and NFRA will be carried out in an electrode-resolved manner to separate the contributions from the negative and the positive electrodes. In conjunction, a proper interpretation of the NFR spectrum is demonstrated together with EIS.

## 3.1 Introduction

One of the important physical properties of electrodes is the particle size distribution of the active material. In the previous study by Bläubaum et al. [26], he investigated mesocarbon microbeads graphite particles, particles of spherical form, with four different particle size distributions. It is shown that fine to middle-sized particle size distribution led to capacity loss mainly due to surface-related side reactions such as SEI formation. Interestingly, lithium plating was observed on the particle surface of coarse and broad particle size distribution right after formation due to the slow charge transfer and diffusion kinetics. However, for cells with these particle size distribution, a notable decrease in overall kinetic and transport losses during cycling was observed. There, micro-cracking could have taken place because a small specific surface area leads to a high local current density on coarse graphite particles, as also observed in [122–124]. Also, cells with broad and coarse

[1] This chapter has been published in H.S. Chan, L. Bläubaum, D. Vijayshankar, F. Röder, C. Nowak, A. Weber, A. Kwade and U. Krewer, Batteries & Supercaps, 2023. DOI of the original article: `https://doi.org/10.1002/batt.202300203` [121].

particle size distribution showed significant degradation behaviour as they contain the ageing effect of both fine and broad particles.

In most of the above-mentioned studies, C-rate tests and galvanostatic cycling were used to characterise the electrochemical performances of lithium-ion batteries. The former analyses the combined kinetic behaviour of the batteries concerning different current loads, while the latter investigates the performance stability under continuous constant current charge and discharge. However, both methods could not characterise the internal state of the batteries distinguishably, whereby the deconvolution of the losses into charge transfer, mass transport, ohmic and contact losses can only be determined via a specially constructed system [125] or sophisticated characterisation methods. To mitigate these shortcomings, frequency response analyses [78, 79, 126] were used in this study. For example, EIS is performed to identify the individual losses at a defined SOC. While EIS is limited to linear interpretation of the system behaviour, nonlinear characterisation via NFRA [106, 110, 111] extends the analysis to the nonlinear nature of the involved reactions in batteries. Therefore, NFRA is used in this study. Several publications on NFRA indicate its ability to extract additional information compared to EIS, for example, charge transfer symmetry [112, 113], lithium plating detection [107], prediction of capacity fade, and identification of ageing causes [108, 109].

In this chapter, I aim to build a deeper understanding of the ageing behaviour of cells with negative electrodes with different particle size distribution via the frequency response analysis approach. As mentioned before, apart from EIS, I additionally consider NFRA to include ageing-induced changes in the nonlinear behaviour resulting from different particle size distribution. Specifically, both EIS and NFRA will be carried out in an electrode-resolved manner to separate the contributions from negative and positive electrodes, which will give new and deeper insights into the performance degradation with different particle size distribution.

## 3.2 Methodology

*Electrode production* — In this study, the negative electrode published in [26] with three fractions of different particle size distributions and the source material were used. The negative electrode was initially produced by C. Nowak et al. and has been published in the work [127]. The active material for the negative electrode was artificial graphite MCMB powder from Osaka Gas Chemicals Co. Ltd, which has an average specific capacity of $325\,\mathrm{mA\,h\,g^{-1}}$ [26]. Table 3.1 shows the characterisation results of the negative electrode.

The positive electrode from Customcells was used in this study. The selected positive electrode has an average specific capacity of $145\,\mathrm{mA\,h\,g^{-1}}$ and contains 86 wt.% of active material (NMC-111) and 14 wt.% of additives and binder. The material of the positive and the negative electrodes with different particle size distributions in this study is similar to that reported in the work [26].

**Table 3.1:** Characteristic of the different particle fractions and their corresponding source material from the negative electrode. [26]

| Material | Acronym | $x_{50}{}^{a}/\mu m$ | $\varepsilon_{c,ML}{}^{b}/\%$ | $d^{c}/\mu m$ | $S_v{}^{d}/m^2cm^{-3}$ | $C_{theo}{}^{e}/mAh$ |
|---|---|---|---|---|---|---|
| Source material | SM (broad) | 12.90 | 50 | 74 | 1.36 | 5.05 |
| Fraction 1 | F1 (fine) | 1.53 | 45 | 78 | 4.31 | 4.99 |
| Fraction 2 | F2 (middle) | 5.86 | 45 | 69 | 1.06 | 5.19 |
| Fraction 3 | F3 (coarse) | 17.45 | 59 | 66 | 0.38 | 5.15 |

[a] median particle size
[b] porosity based on the coating mass loading on the electrode, the resulting mass loading for all negative electrodes was $8.9\,mg\,cm^{-2}$
[c] electrode thickness
[d] volumetric specific surface area
[e] theoretical electrode capacity calculated based on the positive electrode

*Cell assembly and ageing experiment* — Cell assembly was performed by D.Vijayshankar, while all subsequent measurements were conducted by the author. Electrochemical characterisations were done in a commercial three-electrode setup (PAT-Cell) from EL-CELL GmbH. In between the negative and positive electrodes, a commercial insulation sleeve (ECC1-00-0210 V/X) from EL-CELL GmbH that consists of polypropylene and polyethylene separator with a thickness of 220 µm and a built-in lithium reference ring was used. As the electrolyte, 103 µL mixtures of ethylene carbonate and dimethyl carbonate with a ratio of 1:1 (v/v) and 1 M lithium hexafluorophosphate were used. The whole cell assembly process was completed inside an argon-filled glovebox ($O_2$ and $H_2O < 0.1$ ppm). For reproducibility, three cells were built for each fraction of a given particle size distribution. The freshly built cells were rested for 12 hours in a temperature chamber (ESPEC EUROPE GmbH, SU 642) at 25 °C. After that, the cells were subjected to the formation and cycled using a battery cycler (MACCOR INC., Series 4000). During the formation step, the cells were charged and discharged with C/10 in the constant current (CC) step for two cycles and constant current-constant voltage (CC-CV) step for one cycle between 2.9 V and 4.2 V at 25 °C. The CV step was stopped when the charging current was reduced to C/20. Within a similar voltage window and temperature, the ageing experiment was conducted at 1C in CC-CV step. The abort criterion for the ageing experiment was when either of the cells had reached the SoH 60 % (60 % of its initial capacity) or 200 cycles. The protocols for the formation cycle and the ageing experiment are detailed in Table 3.2.

*Electrochemical characterisation* — EIS and NFRA were conducted at 25 °C and SoC 50 % right after the formation step at the $4^{th}$ cycle, after the $50^{th}$ cycle and after every consecutive 100 cycles using Zahner Zennium electrochemical workstation. SoC 50 % was adjusted by discharging the cell from a fully charged state at 4.2 V by C/10 for 5 hours, whereby the SoC-adjustment current depended on the capacity that was measured from the previous characterisation series. For example, the SoC-adjustment current for the characterisation at the $100^{th}$ cycle is determined from the capacity that was characterised at the $50^{th}$ cycle. For EIS, the cells were measured under galvanostatic mode

**Table 3.2:** Protocol for formation and ageing experiment.

| | **Formation** | **Ageing experiment** |
|---|---|---|
| Temperature | 25 °C | |
| No. of cycles | 3 cycles | 200 cycles |
| Dis-/charge pattern | CC: 2 cycles (C/10)<br>CC-CV: 3rd cycle (C/10) | CC-CV: 1C charge<br>CC: 1C discharge |
| Abort criterion for CV | I < C/20 | |

with an excitation amplitude of 500 µA and a frequency range between 10 mHz and 10 kHz. As for NFRA, the cells were measured under a similar measurement mode but with a higher excitation amplitude of 10 mA and a smaller frequency range between 100 mHz and 1 kHz. The amplitudes of up to nine harmonics $Y_{2-9}$ were measured, which correspond to multiples of the fundamental frequency $f_1$. During NFR measurement, the cells were moderately excited, giving rise to only the second harmonic $Y_2$ and third harmonic $Y_3$ with sufficient signal-to-noise ratio, so that the interaction between the higher harmonics can be minimised [106].

*Measurement reliability and data treatment* — As known, the utilisation of a reference ring electrode may lead to artefacts during frequency response measurements, for example, inductive loops in certain frequency ranges of AC impedance [128, 129] or NFR spectra. Still, it is a useful in-operando analysis technique to obtain the DC potentials and overpotentials of the negative and the positive electrodes. Symmetrical cells were not applied as the measurements had to be performed during the ageing procedure in a working full cell [129]. The frequency range in EIS, where the artefact appears, was identified and disregarded the DRT analysis in the artefact range by greying out the specific frequency region in the spectra.

In addition, the measured NFR data must be conditioned according to an algorithm developed in-house. The algorithm diminishes artefacts originating from the potentiostat itself: the measured response signals contain not only responses from the battery but also responses of the battery corresponding to the undesired harmonics in the input signal. Furthermore, those NFRA data are only considered reliable where nonlinear response signals (normalised against the linear signals) are at least 1 % of the linear response signals. The unreliable NFRA region is marked in red.

The derivation of DRT from EIS spectra was performed using the in-house established software tool "All-Fit" in `MATLAB`. For the DRT computation, the regularisation parameter $\lambda$ has shown to be a significant input parameter that could affect the accuracy of DRT analysis: large $\lambda$ leads to poor deconvoluted DRT peaks (underfitting) while small $\lambda$ causes erroneous splitting of DRT peaks (overfitting). As shown in Figure 3.1, large $\lambda$ ($\lambda = 10^{-2}$) leads to poor deconvoluted DRT peaks (underfitting), e.g., only one broad peak is observed for cells with negative electrode fractions F1 (fine), F3 (coarse) and SM (broad). When $\lambda$ decreases, the broad DRT peaks are better deconvoluted

into additional peaks, which are previously concealed under the broad DRT peak. However, too small $\lambda$ ($\lambda = 10^{-4}$) causes erroneous splitting of DRT peaks (overfitting), which have no physical meaning. In Figure 3.1, $\lambda = 10^{-3}$ is shown to be the optimal value, i.e., $\lambda$ is sufficiently small to ensure a good resolution for DRT computation and at the same time large enough to avoid false peaks due to overfitting.

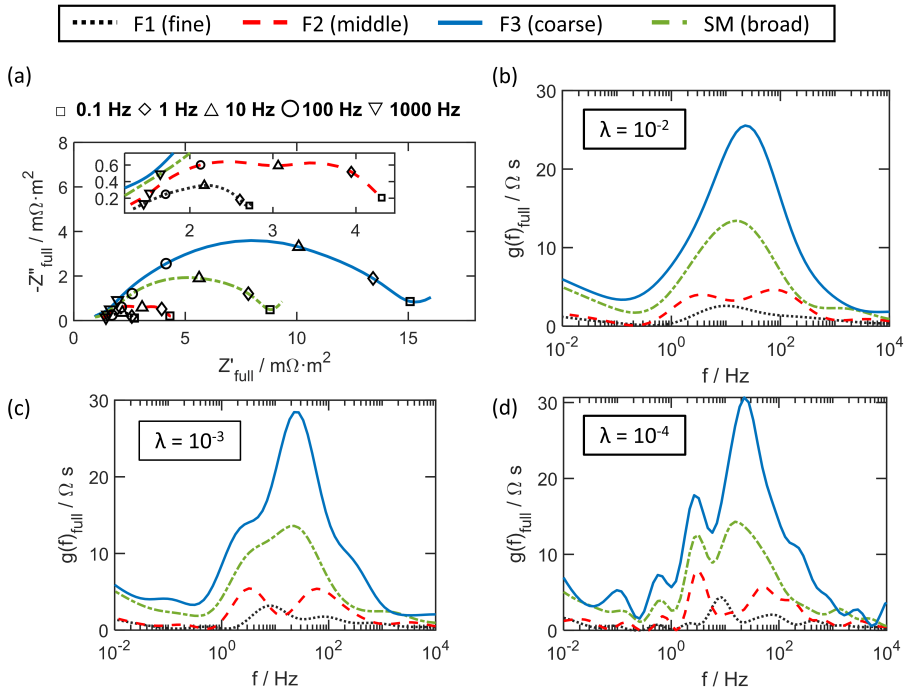


**Figure 3.1:** (a) EIS spectra recorded with cells built from four different particle size distributions at 25 °C and SoC 50 %. DRT spectra computed from the EIS spectra using different regularization parameters with (b) $\lambda = 10^{-2}$, (c) $\lambda = 10^{-3}$ and (d) $\lambda = 10^{-4}$.

## 3.3 Results and Discussions

In the following, the effect of particle size distribution on the performance of formatted cells (pristine state) including their dynamic behaviour is analysed. This is followed by an ageing study, which reveals the change in the performance and frequency response spectra that can be related to the ageing processes.

### 3.3.1 Pristine state

The states of the battery cells with different particle size distributions were characterised right after the formation step. Complementary to EIS, the distribution of relaxation times (DRT) technique was implemented for a clearer separation of processes with different time constants [93]. These processes were then analysed deeper with NFRA to observe the nonlinear behaviour of these processes.

Figure 3.2 (a) shows the full cell DRT spectrum at SoC 50 % directly after formation for cells with different particle size distributions at negative electrode: F1 (fine), F2 (middle), F3 (coarse), and SM (broad). Figure 3.2 (b) displays the respective Nyquist diagram of the EIS. From the full cell DRT spectrum, two to three main peaks can be identified in the trusted region of the spectra: one peak between 1 Hz to 10 Hz, another from 10 Hz to $10^2$ Hz and the third one above $10^2$ Hz. Overall, characteristic frequencies and peak height change with particle size distributions. The peak height decreases with decreasing particle size. Electrode-resolved analysis as shown in Figure 3.2 (c) and (d) allows assigning these peaks and dynamic phenomena to negative and positive electrodes. Here, one can identify that the peak in the low-frequency region (1 Hz to 10 Hz) is attributed to the positive electrode while the two higher ones (10 Hz to $10^2$ Hz and above $10^2$ Hz) are mostly from the negative electrode with minute contribution from the positive electrode. The DRT spectra for the negative electrodes in Figure 3.2 (c) show three peaks in total. The first peak at a lower frequency ranging from $10^{-1}$ Hz to 1 Hz arises from a measurement artefact, i.e., inductive loop. These artefacts will not only influence the recorded EIS at the negative electrode but also at the positive electrode, i.e. a flattened curve within the respective frequency range at the EIS of the positive electrode. Hence, this first DRT peak at the negative electrode will not be considered in further analysis. The assignment of the peaks in the DRT to physicochemical processes in the cell is based on prior studies [106, 130]. The second peak at about 10 Hz to $10^2$ Hz is related to the charge transfer process at the negative electrode/electrolyte interphase and the third peak above $10^2$ Hz is attributed to the ionic transport across the SEI layer. Comparing the DRT spectra of the negative electrode for the various particle size distributions, it can be generally observed that the peak height that can be correlated to the charge transfer kinetics increases and the corresponding characteristic frequency decreases with increasing particle size. Finer particles have a larger specific surface area, which favours a faster charge transfer process. Thus, a smaller impedance or smaller DRT peak is observed for finer particles.

The DRT spectrum at the positive electrode in Figure 3.2 (d) shows two peaks. The peak at around 1 Hz to 10 Hz is attributed to the charge transfer process at the electrode/electrolyte interphase of the positive electrode and the smaller peaks at frequencies > 10 Hz are attributed to ionic transport in the pores of the positive electrode along the electrode thickness [131]. All the impedance spectra and DRTs at the positive electrode were initially expected to be identical for all cells since a similar positive electrode was used in all cells. Yet, from Figure 3.2 (d), it is obvious that this is not the case. Considering the main peak, the height and relaxation frequencies differ. Especially in the case of a fine powder, a significant difference is observed. Only a small part of these differences is related to

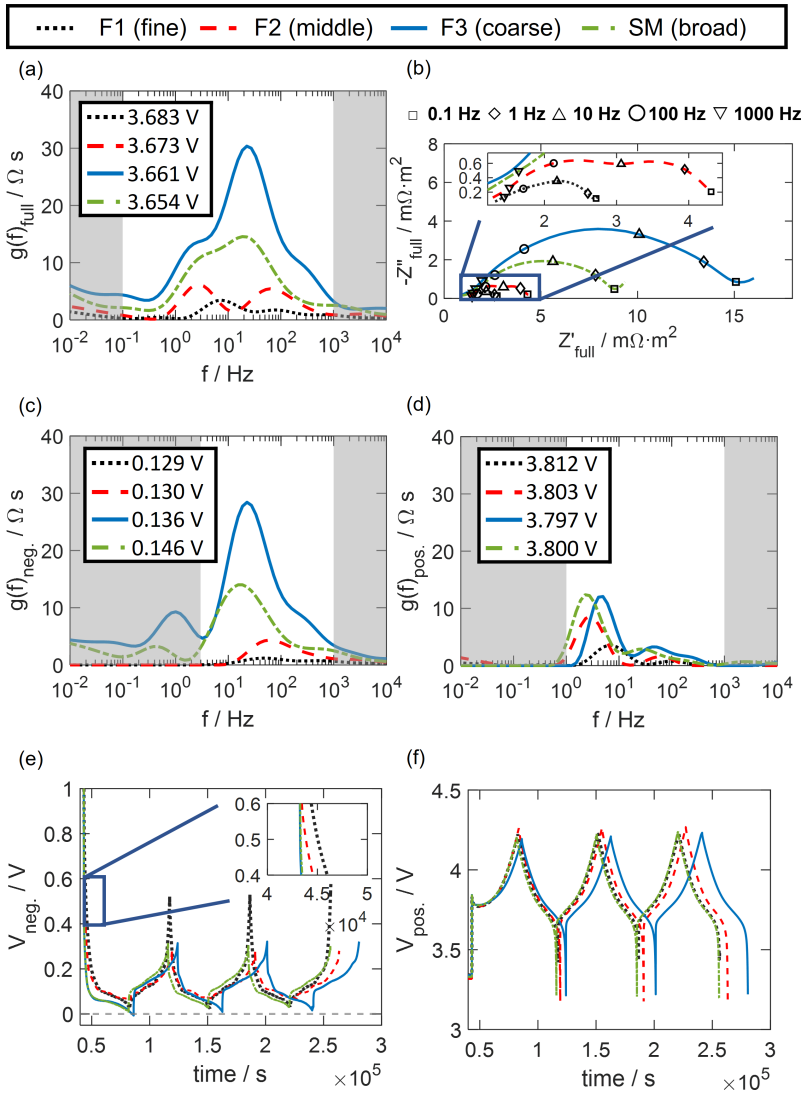


**Figure 3.2:** Impedance and DRT spectra after formation at SoC 50 % for cells with F1 (fine), F2 (middle), F3 (coarse) and SM (broad) particle size distribution at the negative electrode recorded at 25 °C: full cell (a) DRT and (b) EIS spectra, electrode-resolved DRT spectra at (c) the negative and (d) the positive electrodes. The shaded area indicates less reliable DRT data. The given voltages indicate the open circuit potentials that correspond to the SoC 50 % adjustment. Half-cell potentials at the (e) negative and (f) positive electrodes during formation.

the reproducibility in cell manufacturing as shown in Figure 3.3. The major impact is the difference in the electrode balancing of different particle size distributions during formation. Fine particles (F1) with a larger mass-specific surface area exhibit a smaller kinetic loss at the negative electrode and simultaneously favour surface-related side reactions such as SEI formation, leading to loss of active lithium and affecting electrode balancing overall as shown in Figure 3.2 (e) and (f). This results in the difference in the lithium concentration distribution or lithiation degree in the positive electrode as indicated by the half-cell potential in 3.2 (f), which can be therefore related to the change in the EIS of the positive electrode for F1 (fine).

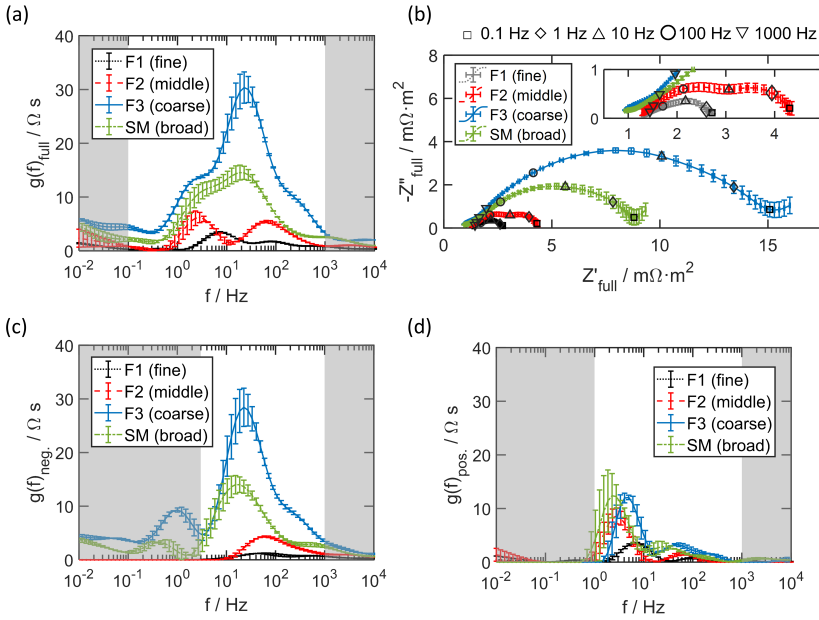


**Figure 3.3:** The error bar shows the measurement standard deviation of three cells for each particle size distribution at 25 °C and SoC 50 %: full cell (a) DRT and (b) EIS, DRT spectra at (c) the negative and (d) the positive electrodes. The shaded area indicates the less reliable DRT analysis region.

The attribution of peaks to certain processes is substantiated by NFR analysis: charge transfer processes should show significant nonlinearities whereas transport across the SEI and ionic transport should show negligible nonlinearities [106, 111]. In Figure 3.4 (a), the full cell NFR spectrum of the cell with F1 (fine) shows nonlinear behaviour only below 10 Hz. By comparing the electrode-resolved NFR spectra, the nonlinear signal from the negative electrode in the inset of Figure 3.4 (a) is about two orders of magnitude smaller than the full cell. Thus, the nonlinear signals in full cell stem mainly from the positive electrode and a correct attribution of this area to the charge transfer process at the positive electrode is confirmed. In contrast to F1 (fine), the full cell NFR spectra of cells with fractions F2 (middle), F3 (coarse) and SM (broad) feature nonlinear responses starting already from higher frequencies around $10^2$ Hz, which is characteristic to the charge transfer process at the

negative electrode. For F3 (coarse) and SM (broad), the nonlinear response at the negative electrode is similarly large as the full cell response. This confirms the attribution of the nonlinear responses within the designated frequency range to the charge transfer at the negative electrode. For F2 (middle), at a higher frequency range (roughly between 10 Hz and 200 Hz), NFR spectra (especially third harmonic $Y_3$) for full cell and the negative electrode are almost identical, i.e., charge transfer at the negative electrode dominates, whereas similar as in DRT, contributions from the positive electrode come into play at lower frequency range.

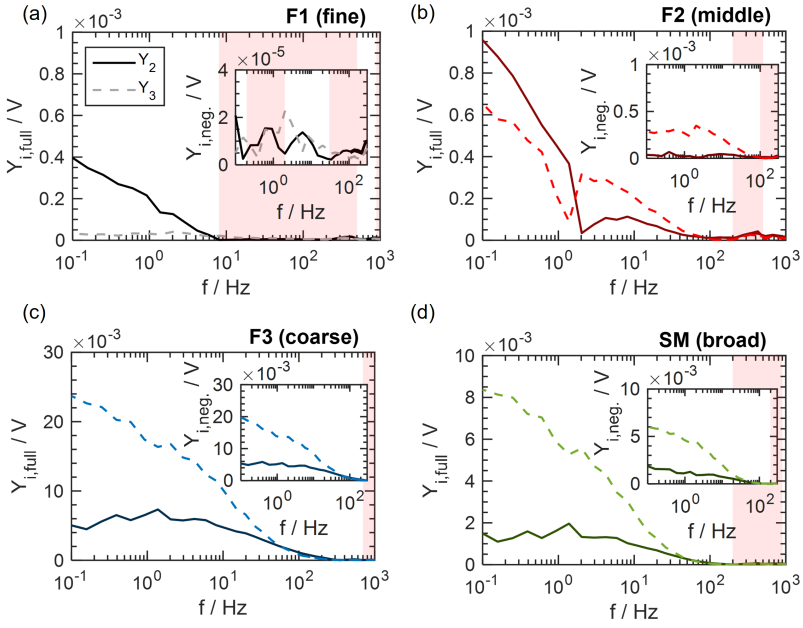


**Figure 3.4:** Full cell NFR spectra for cells with fractions (a) F1 (fine), (b) F2 (middle), (c) F3 (coarse) and (d) SM (broad) recorded after formation at 25 °C and SoC 50 %: $Y_2$ (solid lines) vs.$Y_3$ (dashed lines). The insets show the corresponding NFR spectra of the negative electrode. The red regions indicate unreliable regions for NFRA.

In general, similar to impedance, a monotonous relation between particle size distribution and nonlinear responses in the characteristic frequency range of the charge transfer process at the negative electrode can be drawn: The larger the particle size, the smaller the surface area, which is unfavourable to the charge transfer process. Thus, larger impedance and nonlinear response, especially $Y_3$, are observed. In none of the cells, significant nonlinearities are observed in the frequency range of $10^2$ Hz to 1 kHz. This confirms that the processes observed in DRT at this frequency range are not charge-transfer processes, but most probably SEI processes and ion transport processes. Interestingly, it seems that the amplitude of the second harmonic, $Y_2$ and the third harmonic, $Y_3$, have different sensitivities to the negative and the positive electrodes: the positive electrode causes significant $Y_2$

responses (see F1), whereas the negative electrode causes more $Y_3$ (see F3). This indicates asymmetry in the charge and discharge kinetics, or in other words, the charge transfer coefficient as typically used in the Butler-Volmer equation deviates stronger from 0.5 for the positive electrode.

In summary, by combining EIS and NFRA, a clear attribution of frequency response features at certain frequencies to specific processes could be established. F1 (fine) is more dominated by charge transfer at the positive electrode, whereas F3 (coarse) and SM (broad) have very high contributions from the charge transfer at the negative electrode.

### 3.3.2 Ageing

Having established an in-depth understanding of the losses in cells with different active particle sizes of the negative electrode, and how they can be monitored with EIS and NFRA, the following section focuses on ageing-induced changes in these cells and their losses. Figure 3.5 shows the ageing-related changes in the discharge behaviour and half-cell potential at the negative electrode during cycling for all four particle size distributions.

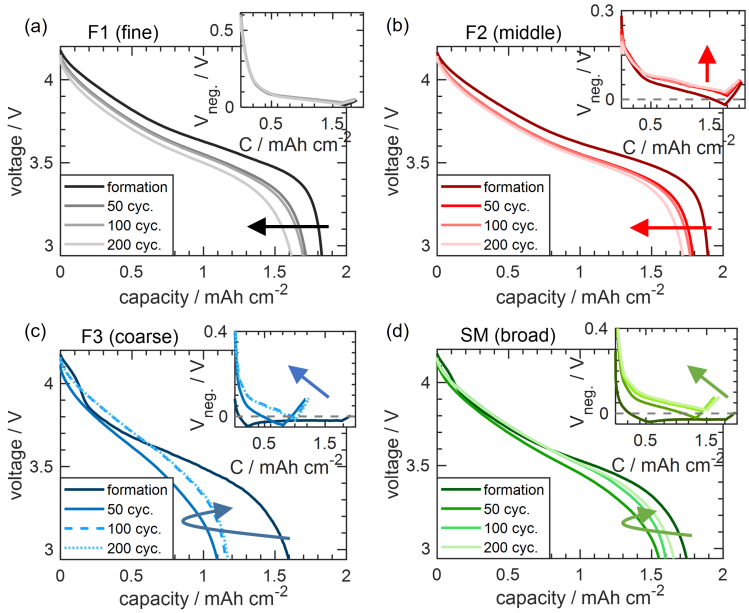


**Figure 3.5:** Change in 1C discharge behaviour during cyclic ageing of cells with (a) F1 (fine), (b) F2 (middle), (c) F3 (coarse) and (d) SM (broad) with respective half-cell potential at the negative electrode given in the insets.

It is shown that the fine (F1) and medium-sized particle size distribution (F2) have strong similarities to each other, and the coarse (F3) with broad particle size distribution (SM), respectively. Cells

with F1 (fine) and F2 (middle) show monotonous capacity fade with cycle number. This is mostly attributable to losses at the positive electrode, as half-cell potential at the negative electrode remains almost constant (see inset). In contrast, cells with F3 (coarse) and SM (broad) show an instantaneous decrease and later increase in capacity. The instantaneous decrease in capacity is attributed to plating at early cycles, which occurs when the potential at the negative electrode drops below zero (see inset). A fraction of the plated lithium reacts irreversibly with electrolyte, forming a new SEI film and leading to a loss in lithium inventory, thus, significant capacity fade. Other possible reason for the capacity fade could be that the micro-cracking, leads to the electrical isolation of the active material and is no longer useable for further lithium deintercalation and intercalation. However, as the cells continue to age, the cells recover in capacity. This similar occurrence has also been pointed out previously in [26]. It is suggested that one possible reason is due to the changing of the cycling current (1C). A significant capacity loss for F3 (coarse) and SM (broad) was observed until the 50$^{th}$ cycle. After that cycle, the discharge rate of 1C was adapted to the new capacity, leading to lower current and thus higher capacity of ca. 3 % for SM (broad) and 8 % for F3 (coarse) (see Figure 3.6). This effect is no longer visible after 100$^{th}$ cycle. Therefore, the further capacity increase in SM (broad) might be attributed to the kinetic improvement and will be investigated in-depth via EIS and NFRA.

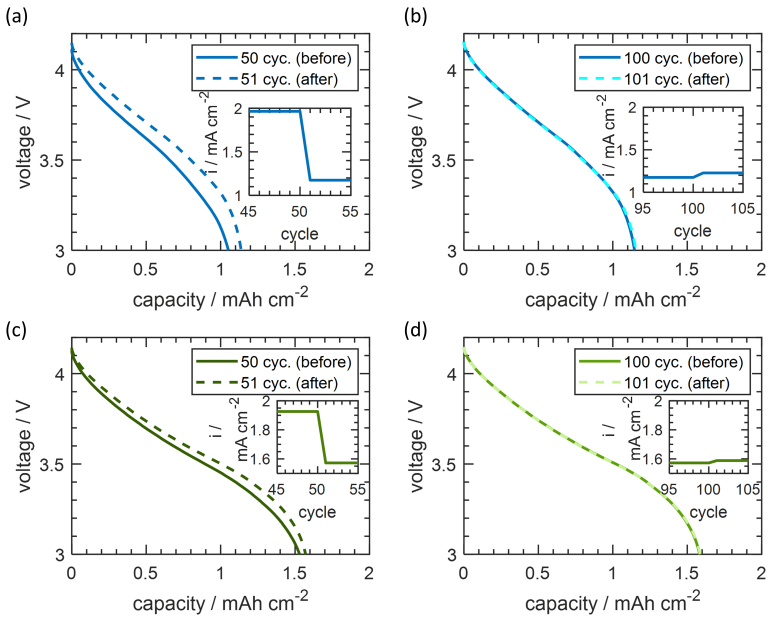


**Figure 3.6:** Comparison of discharge behaviours (1C) at the 50$^{th}$ cycle (before) and 51$^{st}$ cycle (after) (a) for F3 (coarse) and (c) for SM (broad) as well as at the 100$^{th}$ cycle (before) and 101$^{st}$ cycle (after) for (b) F3 (coarse) and (d) SM (broad).

EIS and NFRA allow a deeper look into ageing, and here especially into the kinetic changes of the different particle size distributions. For cells with F1 (fine) and F2 (middle) in Figure 3.7 (a) and (c), one could observe during ageing a significant increase in DRT peak at frequencies below 10 Hz, which is attributed mainly to a worsened charge transfer process at the positive electrode. The peak shifts to lower frequencies as the cell ages, further supporting that charge transfer at the positive electrode becomes slower. The ageing-induced increase in the third harmonic $Y_3$, Figure 3.7 (b) and (d), is visible in the same low-frequency range, and thus attributed to the worsening kinetics of the positive electrode. The increase with worsening kinetics is expected, as increased nonlinearity has been shown before for decreased charge transfer kinetic constants, i.e., exchange current densities [112, 113]. In the frequency range of the negative electrode (> 10 Hz), no significant increase in DRT peaks or nonlinearities can be seen for cells with F1 (fine). In contrast, F2 (middle) negative electrode, which already exhibited nonlinear and linear responses for the pristine cells, shows a decrease in impedance and nonlinear responses ($Y_3$) during ageing. This suggests a kinetic improvement of the corresponding charge transfer processes at the negative electrode of F2 (middle) [65].

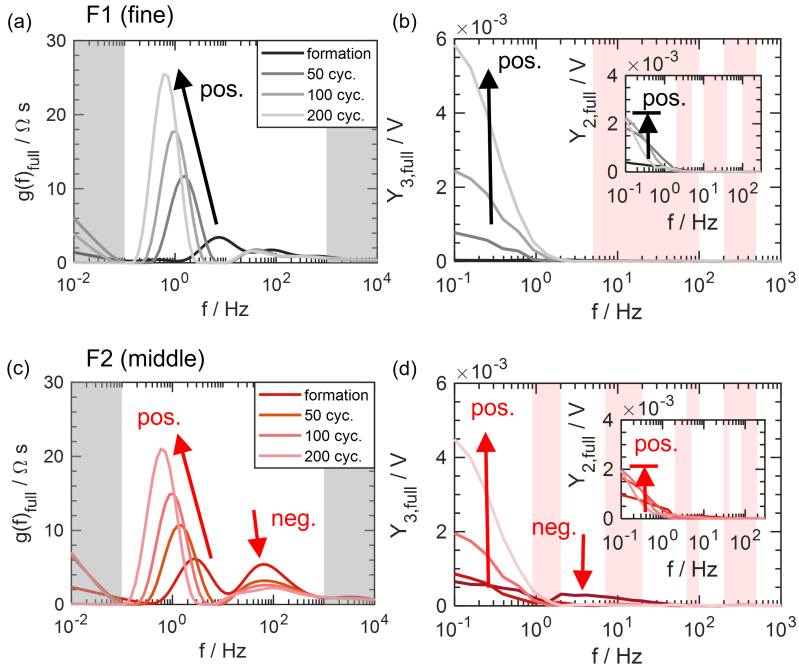


**Figure 3.7:** Ageing-related changes of cells with F1 (fine) particle size distribution in full cell (a) DRT and (b) NFR spectra of $Y_3$ ($Y_2$ in inset) and with F2 (middle) particle size distribution in full cell (c) DRT and (d) NFR spectra at 25 °C and SoC 50 %.

Contrary to $Y_3$, the second harmonic $Y_2$ provide additional information about the asymmetry behaviour of the charge transfer process [112–114]. For both F1 (fine) and F2 (middle), $Y_2$ does not

show a monotonous increase. Instead, $Y_2$ increases mainly at the beginning of cycling up to the 50$^{th}$ cycle, and only in the frequency range of the positive electrode (see insets of Figure 3.7 (b) and (d)). This implies that the charge transfer process at the positive electrode becomes asymmetric at the beginning of ageing while the kinetics of the charge transfer process at the positive electrode, represented by $Y_3$ and EIS, continues to deteriorate as the cells age. The change in charge transfer symmetry suggests a qualitative change in the nature of the reaction during ageing. A possible reason may be the migration of transition metals into lithium vacancies in the early cycles, which causes the energy difference in intercalation and deintercalation as lithium is inserted or removed from different locations [132, 133].

For cells with F3 (coarse) and SM (broad) shown in Figure 3.8 and 3.9, as they age, the DRT peaks that are attributed to the charge transfer process as well as ionic transport through the SEI at the negative electrode decrease and shift to a higher frequency range, which is similar to F2 (middle) and suggests an improvement of the respective kinetics.

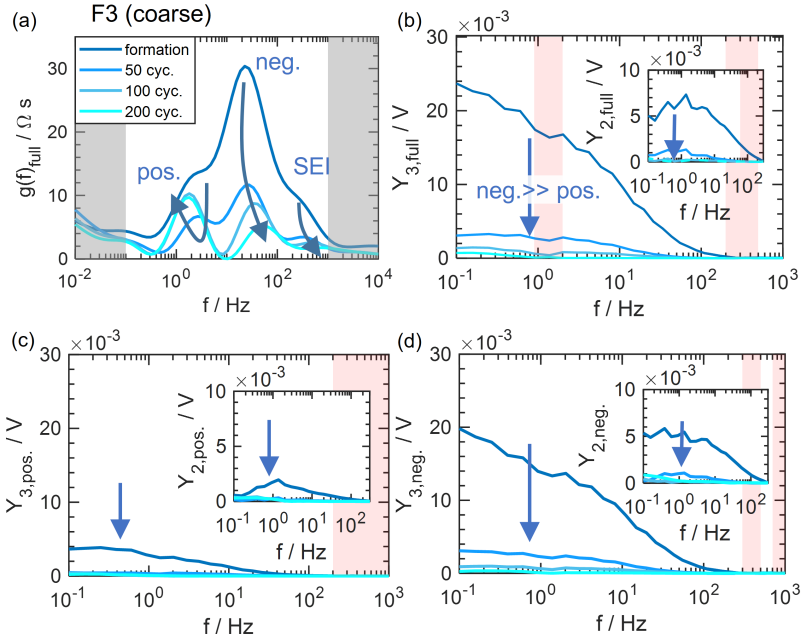


**Figure 3.8:** Ageing-related changes of cells with F3 (coarse) particle size distribution in full cell (a) DRT and (b) NFR spectra of $Y_3$ ($Y_2$ in inset) and electrode-resolved NFR spectra at (c) the negative and (d) the positive electrodes at 25 °C and SoC 50 %.

The kinetic improvement was hypothesised in the prior work [26] and also in other publication [134] to be caused by the micro-cracking that generates more active surface area and lowers the overpotential for the respective processes. In this study, microstructural changes and cracks are proven at the

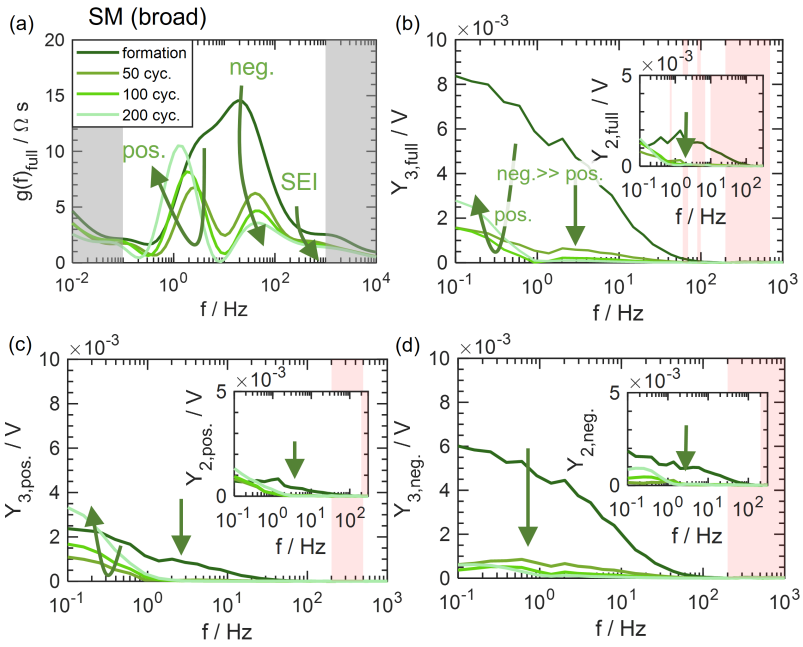


**Figure 3.9:** Ageing-related changes of cells with SM (broad) particle size distribution in full cell (a) DRT and (b) NFR spectra of $Y_3$ ($Y_2$ in inset) and electrode-resolved NFR spectra at (c) the negative and (d) the positive electrodes at 25 °C and SoC 50 %.

negative electrode with scanning electron microscopy for SM (broad) and F3 (coarse) electrodes, as shown in Figure 3.10.

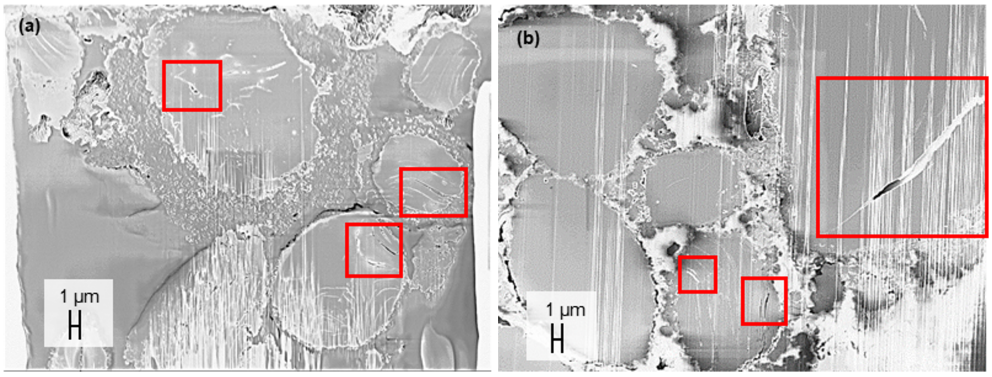


**Figure 3.10:** Cross-sectional cut by focused ion beam and scanning electron microscope (FIB-SEM) scan of the negative electrode for (a) F3 (coarse) and (b) SM (broad) show exfoliation and micro-cracking (red-framed region) within the particles. The vertical white stripes are artefacts during sample preparation.

In addition to the previous work by Bläubaum et al. [26], in which only a small number of cycles were examine, a long-term cycling revealed that, charge transfer kinetics at the positive electrode, which is presented by the DRT peak in the low-frequency range, interestingly first improves and then worsens as the cell further ages. Such a phenomenon has not been observed before and is only visible in longer-term ageing. $Y_3$ again has a similar trend as impedance, except that for the later ageing stage of the cells with F3 (coarse), where only impedance increases at the lower frequency. Meanwhile, for cells with SM (broad), the further increase in $Y_3$ in lower frequencies is visible and identified to be arising from the positive electrode as shown in Figure 3.9 (c). $Y_2$ for both cases behaves similarly to $Y_3$, whereby it decreases significantly in the frequency range of the negative electrode. This indicates that micro-cracking not only improves the charge transfer kinetics at the negative electrode, represented by EIS and $Y_3$, but the charge transfer nature becomes more symmetric. Again, for cells with SM (broad), $Y_2$ increases after the $100^{th}$ cycle. While comparing the electrode-resolved measurements in Figure 3.9 (c) and (d), one could notice that the charge transfer process at the negative electrode, as well as the positive electrode, becomes asymmetric as the cells age.

### 3.3.3 Information content of NFRA vs. discharge curves and EIS

Overall, discharge curves, EIS (DRT) and NFRA were shown to give complementary insights into the effect of electrode design and the ageing behaviour of Li-ion batteries. Discharge curves yield combined kinetic and mass transport losses, which affect the discharge trajectory and gained capacity. Via discharge curves alone, one cannot deconvolute the losses attributed to the kinetic or transport overpotentials. Frequency response analysis fills this gap. EIS enables the identification of overpotentials by different underlying processes. For example, kinetic losses for the charge transfer process at respective electrodes and the transport overpotential through the SEI can be separately identified. NFRA allows discrimination between charge transfer and transport processes through the SEI by their nonlinear behaviour, whereby the transport process through the SEI is almost linear and is not visible in NFR spectra. NFRA provides additional information on the symmetry of the charge transfer process via $Y_2$, suggesting qualitative surface changes, e.g. due to mechanistic changes. Furthermore, the ageing trend of $Y_2$ is different from $Y_3$, which might give extra information on ageing nature. Thus, NFRA yields highly valuable information on the nature and degree of ageing.

## 3.4 Conclusion

The ageing behaviour of LiBs with different particle size distributions of a graphitic negative electrode and NMC-111 positive electrode is assessed in detail using various electrode-resolved measurements. Discharge curves are complemented by EIS and NFRA to separately analyse kinetic and transport processes. NFRA allows additional identification of the nonlinear kinetic contributions.

In this chapter, it is found that the particle size distribution of the negative electrode determines whether the negative or the positive electrode is showing the highest kinetic losses. Strongly different ageing behaviour is observed for cells with different particle size distributions, which are dominated by either the negative or the positive electrode ageing. On one hand, for cells with small to middle-sized particles at the negative electrode, one observed before cycling, the charge transfer kinetic loss at the positive electrode is more dominant than the negative electrode. As cycling begins, the positive electrode is therefore more stressed and aged, causing a consistent reduction in discharge capacity; specifically in this work, the increase in EIS and NFRA due to dominant degradation of charge transfer at the positive electrode is identified. On the other hand, for cells with coarse and broad particle size distribution at the negative electrode, one could observe firstly a decrease and then recovery in discharge capacity, EIS and NFRA. This finding is due to the kinetic improvement at the negative electrode, resulting from the micro-cracking and evidenced by the FIB-SEM scan in this study. Meanwhile, the charge transfer process at the positive electrode also shows a slight increment in EIS as well as NFRA in the later cycling stage for coarse and broad particle size distributions, which suggests the degradation of the positive electrode becomes increasingly significant when the cells continue to age in the long term. Additionally, via second harmonic $Y_2$ in NFRA, it is further identified that the positive electrode shows stronger charge transfer asymmetry whereas the negative electrode is dominated by third harmonic $Y_3$ due to inferior charge transfer kinetics. Also, $Y_2$ shows a different ageing trend than impedance and $Y_3$, which is believed could be related to the change in charge transfer symmetry.

In summary, I conclude that the frequency response analysis method - EIS complemented with NFRA is an essential tool to get additional information on the nature of kinetic and surface-related processes as shown in this work, which then answered the research question as proposed early in the chapter. It is highly interesting to correlate NFRA with surface analysis tools, which should give more information on the physical processes, especially during LiB ageing. As one has seen that the frequency response methods show some degree of correlation to the LiB ageing, it might be practically beneficial to use the frequency response analysis method to predict the state of the battery, for example, to estimate the SoH and SoC of the battery for optimal and safe operation. Hence, in the upcoming chapter, I am going to focus on exploring the feasibility of the state estimation via frequency response analysis method using both EIS and NFRA, which serves as the next research question to be answered.

# 4 Data-Driven-based Model Analysis [2]

**Research question:** *Is NFRA able to quantify LiBs ageing?*

SoH estimation is extremely essential for an economically viable and safe operation of LiB. The most common method to determine SoH is by integrating the transient current during one complete charge/discharge cycle at a nominal operating current. The major drawback of this method is the long measurement duration. Meanwhile, frequency response-based measurements can be carried out more rapidly than a controlled full charge/discharge. Also, it provides a spectral representation of the dynamics of underlying physicochemical processes in the battery, giving evidence about its internal physical state. Thus, the frequency response methods constitute prospectively more information and perhaps more accurate in determining the SoH of aged LiBs. In the previous chapter, one can see that NFR signals change, to some extent, monotonously with battery ageing. In this context, NFRA might be feasible for the ageing quantification, i.e., SoH estimation of LiB. In this chapter, NFRA's potential will be fully explored and compared with the conventional EIS in terms of the precision and uncertainty of the SoH estimation. For this purpose, an empirical approach will be adopted for EIS and NFRA each and the methodology will be detailed in the following sections.

## 4.1 Introduction

Various SOH estimation models or algorithms have been proposed [136]. A data-driven model involves the training of an empirical model that maps a defined set of ageing parameters to SOH. For example, Zhou et al. defined mean voltage falloff within a specific voltage window as an indicator to predict SOH via simple regression and optimised relevance vector machine approaches [137]. For online SOH estimation, Zhou et al. employed an optimized gray model based on the time interval of equal discharging voltage difference [138], while Li et al. implemented a recurrent neural network with long short-term memory that uses a raw partial charging curve [139]. Examples of other ageing parameters that have been proposed include the voltage at the beginning of discharge [140], CC-CV charging time [141–143], charging/discharging energy and efficiency [141, 144], rate of change of

[2] Parts of this chapter have been published in H.S. Chan, E.J.F. Dickinson, T.P. Heins, J. Park, M. Gaberšček, Y.Y. Lee, M. Heinrich, V. Ruiz, E. Napolitano, P. Kauranen, E. Fedorovskaya, T. Kallio, S. Mousavihashemi, U. Krewer, G. Hinds and S. Seitz, Journal of Power Sources, 2022. DOI of the original article: `https://doi.org/10.1016/j.jpowsour.2022.231814` [135].

CV charging current [142], nominal voltage [141, 142, 144], peak heights/ratio from incremental capacity analysis (ICA) [145], incremental voltage difference [146], characteristic features from the voltage relaxation curve [147], etc.

Besides ageing parameters drawn from the DC voltage response, models resolving the dynamic response of a cell, for example, EIS and NFRA, seem to be highly suitable for such tasks, as they allow extraction of characteristic time constants and features from the dynamic experimental response, which can be correlated to physical processes and states, such as SOH. Efforts to date on SOH prediction using EIS have been reviewed comprehensively by Mc Carthy et al. [148], including online estimation challenges. One simple approach is the direct correlation of a spectral feature with cell degradation. For example, Zhang et al. showed that, for a particular data instance, the impedances at 17.8 Hz and 2.16 Hz had the strongest correlation to the degradation, and so could be used for SOH estimation [149]. Wang et al. demonstrated that the phase shift at 79.4 Hz correlated positively to the internal temperature of the cell [150]. A more involved impedance-based approach is SOH estimation using parameterisation from equivalent circuit models. Here, changes in circuit fit parameters are correlated to SOH. For example, both ohmic and charge transfer resistances have been shown to be reliable SOH predictors, as they increase consistently and significantly during cell ageing [151–153]. Other researchers have demonstrated promising SOH estimation accuracy by considering additional EC parameters, namely SEI layer resistance, capacitance dispersion, inductance, and double layer capacitance [154–156]. Eddahech et al. pointed out that by considering operating conditions such as temperature, cycling profile and DoD variation in conjunction with ageing-relevant parameters such as equivalent series resistance, the established SOH estimation model is more general to different applications and operating conditions [157]. Examples of this wider approach include the work of Wang et al., who established an SOH estimation model based on charge transfer resistance fitted from an EC model, including temperature and SOC variation [158], and Li et al., who extracted ohmic resistance from an EC model via particle swarm optimisation and implemented it as an indicator for online SOH prediction in a cloud-based BMS [159].

Harting et al. revealed that higher harmonic signals are sensitive to ageing [109]; not only do nonlinear responses increase with decreasing SOH but the higher harmonics also change in a different way with the underlying ageing process, e.g., Li plating vs. SEI growth. Quantitatively, correlation between NFRA and SOH has been achieved using various features of the response amplitude either directly or with machine learning. In Ref. [108], a support vector machine model for SOH prediction based on the summation of the second and third harmonics gave prediction accuracies below 5%.

In this chapter, I am going to explore the feasibility of both EIS and NFRA in SOH prediction. Since these various previous studies used different experimental conditions, making the direct comparisons of the methodologies impossible. Here, in this chapter, for each of the investigated methods, I follow a common, systematic framework, progressing through data collection, data processing, parameter selection, model training, and model validation. Here, all methods are tested under equivalent experimental conditions, using a consistent source for the tested cells, with measurements undertaken

at multiple institutions in parallel to demonstrate robustness of the methods with respect to hardware variation. Each of the methods is thoroughly evaluated in terms of its practical feasibility and estimation accuracy.

## 4.2 Battery Testing Protocols

Life-cycle tests (LCTs) were conducted by four different measurement institutions[3] on cylindrical 18650 batteries (9 batteries in total, obtained from LG Chem) with a nominal capacity of 3 A h. The selected battery chemistry has a lithium nickel manganese cobalt oxide ($LiNi_{0.8}Co_{0.1}Mn_{0.1}O_2$) positive electrode and a silicon-graphite composite negative electrode (Si content estimated as $2.8 \pm 0.5$ wt.% from post-mortem SEM-EDX analysis). The batteries were cycled between 3.0 V and 4.2 V (Depth-of-Discharge (DoD) 100 %) at 45 °C and 4 A ($\approx$ 1.33C), with a CC-CV protocol in the charging direction (current cut-off at 300 mA) and CC in the discharging direction. Different battery cyclers were used at different institutions (Modulab-MACCOR, BaSyTec XCTS, BioLogic MPG-205). At 50- or 100-cycle intervals, the capacity of each battery was measured under consistent, repeatable conditions considered practical for a future standard measurement method, at 23 °C and 1.25 A ($\approx$ 0.4C). SoH is computed by taking the ratio of the discharge capacity of the aged battery to the initially measured capacity of the fresh battery. Following each capacity measurement, the internal state of the batteries was characterised via EIS and NFRA. Dynamic measurements were carried out under the same conditions as capacity measurement, at specified SoC values using various electrochemical workstations at different institutions (MACCOR, Zahner Zennium, BioLogic SP-200, BioLogic MPG-205). SoC was adjusted by discharging the batteries at 1.25 A from the end-of-charge voltage, with the required extent of discharge being adapted according to the most recently measured capacity. After SoC adjustment, the batteries were allowed to rest for at least 30 minutes before dynamic measurements were conducted.

Measurements at Institute 2 (KIT), which will be focussed in the evaluation in the later section, were performed by Y.Y. Lee and the evaluation of the measurements was performed by the author. Measurement parameters for the EIS and NFR measurements are shown in Table 4.1 and Table 4.2, respectively. For the NFR measurement, the AC excitation amplitude is chosen at 5 A to ensure an excitation of harmonic signals with a good signal-to-noise ratio while avoiding significant battery heating that could induce additional ageing [106]. The investigated SoC range is restricted from SoC 20 to 80 % to avoid overcharging due to the higher AC amplitude. The frequency range has a lower boundary of $10^{-1}$ Hz to avoid drift in the battery state over a longer measurement duration [110].

[3] Measurements were performed within the project framework 17IND10-LiBforSecUse by four different institutions - Institute 1: Joint Reseach Centre (JRC), Institute 2: Karlsruhe Institute of Technology (KIT), Institute 3: National Institute of Chemistry (NIC), Institute 4: National Physical Laboratory (NPL)

**Table 4.1:** EIS measurement parameters and conditions.

| EIS measurement parameters | |
|---|---|
| Temperature / °C | 23 |
| Excitation AC amplitude / A | 0.5 (C/6) |
| SoC / % | 20, 35, 50, 65, 80, 100 |
| Frequency range / Hz | $10^{-2}$ to $10^{4}$ |
| Frequency discretisation (log scale) | 10 points/ decade |

**Table 4.2:** NFR measurement parameters and conditions.

| NFR measurement parameters | |
|---|---|
| Temperature / °C | 23 |
| Excitation AC amplitude / A | 5 (1.66C) |
| SoC / % | 20, 35, 50, 65, 80 |
| Frequency range / Hz | $10^{-1}$ to $10^{3}$ |
| Frequency discretisation (log scale) | Above 66 Hz: 10 points/ decade<br>Below 66 Hz: 5 points/ decade |

## 4.3 Data set and analysis methods

### 4.3.1 Qualitative observations

Figure 4.1 plots the SoH evolution for all batteries against the number of elapsed cycles. A consistent trend is observed for the data from all four institutions (Institute 1: JRC, Institute 2: KIT, Institute 3: NIC and Institute 4: NPL), indicating reproducibility of battery behaviour and SoH measurement. Stronger battery-to-battery variation is noted principally at SoH < 75 %, in which divergence in the rate of accelerated ageing arises across all batteries. The corresponding variation in the EIS spectra is plotted in Figure 4.2. The variation in the EIS spectra at different SoCs during battery ageing (representative data for battery (○) from Institution 2) are shown in Figure 4.3 (a), (b) and (d). A notable impedance increase occurs during battery ageing, especially for the lower-frequency arc (ca. 0.02 Hz to 10 Hz), which is attributable to a charge transfer process for lithium insertion in the active material at one or both electrodes of the battery. The impedance increase within this frequency range is more prominent when measuring at higher SoC. From the EIS data in Figure 4.3, there is a promising indication that the impedance spectrum is sensitive to the SoH fade of the battery, and therefore it is suitable to investigate quantitative models to correlate the impedance data to SoH fade.

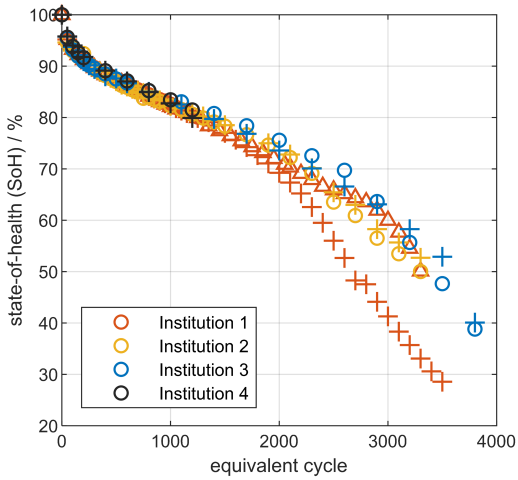


**Figure 4.1:** Dependence of measured SoH on the number of cycles (data for 9 batteries total at 4 institutions - Institute 1: JRC, Institute 2: KIT, Institute 3: NIC and Institute 4: NPL). Batteries are distinguished by colour according to the institution at which experiments were performed. Distinct symbols ('$\circ$', '$+$', '$\triangle$') are used to identify individual batteries measured at each institute. The expected useful range is 70 % to 95 % SoH, corresponding to $< 2000$ cycles.

Unlike EIS, which probes the linear response of the battery, NFRA utilises the higher harmonic signals that are generated when the battery responds nonlinearly to a larger perturbation [99, 106]. Figure 4.3 (c) and (e) show some typical examples of NFR spectra of the corresponding EIS during battery ageing. Notable higher harmonic responses occur only in the frequency range of 0.1 Hz to 2 Hz. For all SoC, the voltage amplitudes of the second ($Y_2$) and third ($Y_3$) harmonics increase monotonically with decreasing SoH. As for the EIS results, higher SoCs give a higher magnitude response. Nonlinear responses are only expected for nonlinear processes, such as charge transfer reactions; slow transport processes can cause additional nonlinearities [112]. The presence of significant nonlinear responses in the frequency range 0.1 Hz to 2 Hz strengthens the inference that the EIS response in this frequency range is attributable to the charge transfer process for lithium insertion in one or both electrode active materials. An increase in the nonlinear response in turn can be correlated to worsening charge transfer kinetics of the LiB, as has been illustrated by mechanistic modelling studies [110]. As the amplitudes of both $Y_2$ and $Y_3$ show a stronger increase during ageing at higher SoC, the high SoC and low-frequency range appears to be most suitable for correlating NFR signals to the SoH fade. This encourages the development of an SoH model that utilises the NFR data directly.

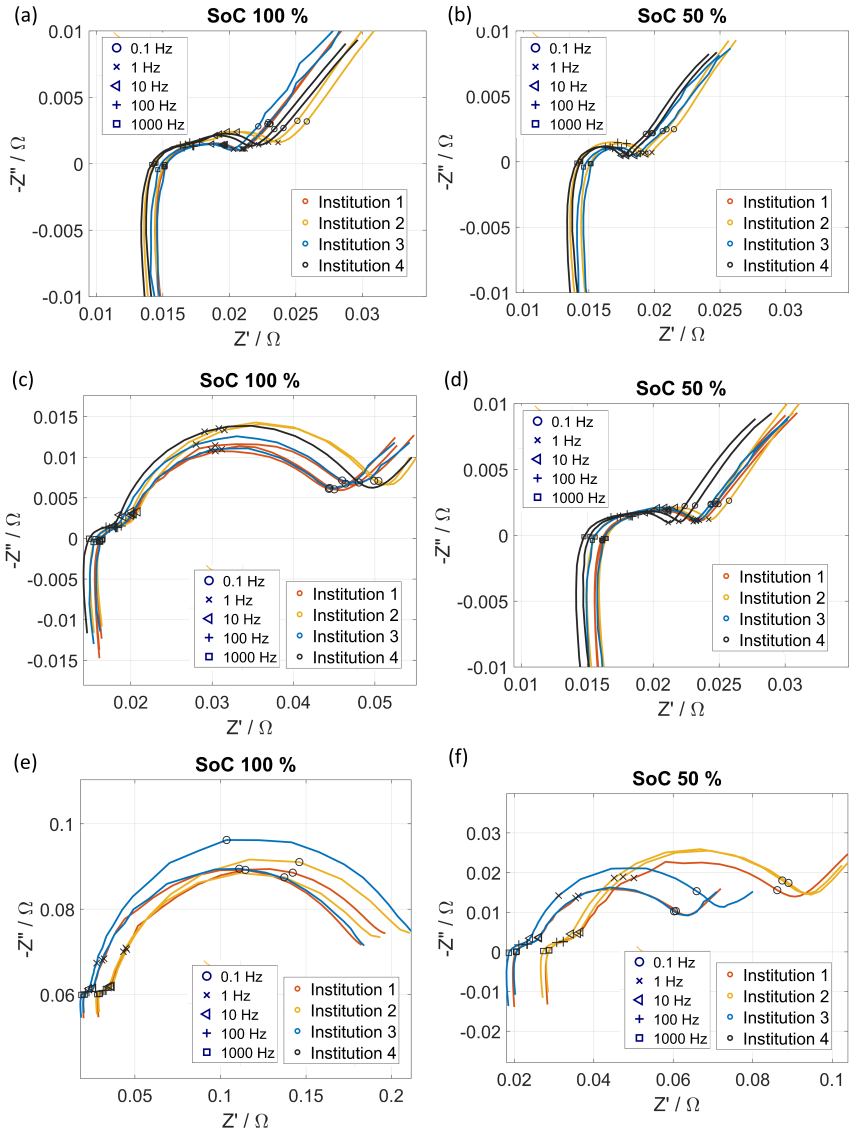


**Figure 4.2:** Comparison of EIS spectra recorded at different institutions under similar measurement conditions but different SoCs and different ageing extent: (a) and (b) before LCT, (c) and (d) after 600 cycles, (e) and (f) after 2900 cycles.

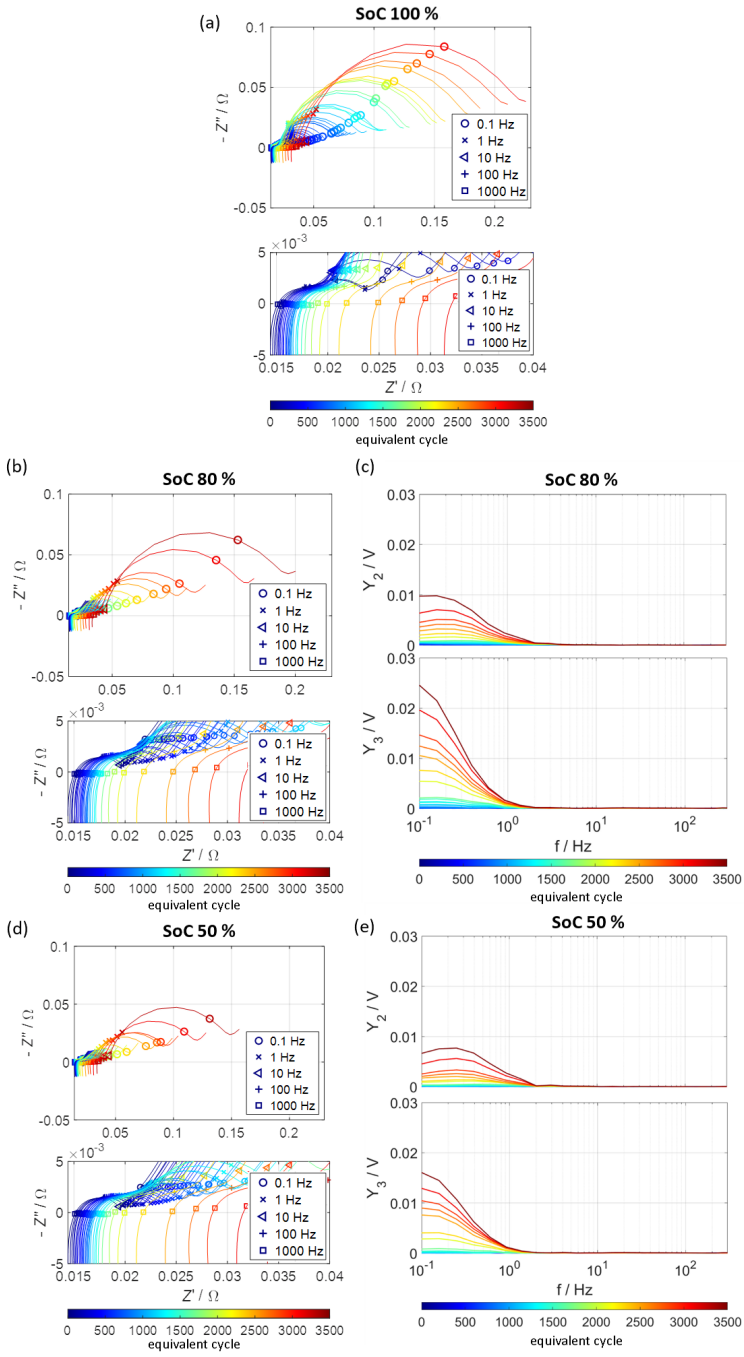


**Figure 4.3:** Example of EIS and NFR spectra during battery ageing recorded at different SoCs for battery (○) at Institution 2 in Figure 4.1. LCTs were conducted at 4 A (CC-CV, cut-off current below 300 mA) and 45 °C. EIS was measured in galvanostatic mode (0.5 A) between $10^{-2}$ and $10^{4}$ Hz at 23 °C. NFRA was measured in galvanostatic mode (5 A) between $10^{-1}$ and $10^{3}$ Hz at 23 °C.

### 4.3.2 Methodology for SoH estimation model training

In this section, a consistent methodology for creating SoH estimation models using EIS or NFRA measurement data will be described in detail. All numerical methods were implemented in MATLAB (MathWorks, version. R2019b or later).

#### 4.3.2.1 Data reduction

To aid model training, data reduction is undertaken using various approaches; following data reduction, highly correlated ageing parameters are selected. Here, only data from experiments where the measured SoH is between 70 % and 95 % are considered. This restriction ensures that the SoH models are applicable in the practical range of interest for real-life applications. To predict the highly nonlinear or anomalous ageing behaviour observed (Figure 4.1) for fresh batteries (SoH > 95 %) and highly aged batteries (SoH < 70 %) would require a much more complicated and, overall, less accurate model, without providing additional insight in the SoH range of primary interest.

#### 4.3.2.2 Ageing parameter selection

Following data reduction according to SoH, suitable ageing parameters that correlate with the SoH fade are identified from each of the frequency response methods. The ageing parameters take the following forms: for the direct impedance-based SoH model, raw EIS spectral data, namely real ($Z'$) and imaginary ($Z''$) impedances at the characterised SoCs and frequencies (Table 4.1); for the NFRA-based SoH model, raw NFR spectral data, namely second ($Y_2$) and third ($Y_3$) harmonics at the characterised SoCs and frequencies (Table 4.2).

For each method, consideration was given to whether a model could be prepared using a single choice of SoC so that only one spectrum would need to be recorded in practice. Priority was given to models using impedance data at SoC 100 % for practical reasons since this battery condition can be more easily achieved than other SoCs (it is attainable by charging to a defined voltage). It is aware that the high sensitivity of impedance to SoC at this SoC extreme might be an argument to discourage this selection; this issue should be evaluated more fully by future work.

The strength of the correlation between the ageing parameters and the SoH fade was assessed via Spearman rank correlation, a generalised correlation method that has been used for battery SoH correlation analysis previously [108]. Spearman rank correlation evaluates the monotonic relation (linear or nonlinear) between the ageing parameter and SoH fade. The Spearman rank coefficient

$\rho_s$ can be computed via Equation (4.1), where d is the difference between the ranks of the ageing parameter and SoH fade and m is the number of experiments.

$$\rho_s = 1 - \frac{6\sum_{i=1}^{m} d_i^2}{m(m^2-1)} \tag{4.1}$$

Absolute values of $\rho_s$ close to 1 indicate a strong monotonic relation, while values close to 0 indicate an absence of correlation. Spearman rank correlation analysis can be complemented with Pearson correlation analysis if an explicitly linear correlation is sought.

#### 4.3.2.3 Model definition and training

The model training approach was proposed by E.J.F. Dickinson. Once ageing parameters had been selected with the support of the correlation coefficient information, an empirical model was developed using the training data set. Models were trained using stepwise linear regression to coefficients of a quadratic function of SoH on ageing parameters $x_i$, combined with binary crosswise terms as the product of pairs of ageing parameters $x_i$ and $x_j$ (Equation (4.2)).

$$\mathrm{SoH} = a_0 + \sum_{i=1}^{m} a_i x_i + \sum_{i=1}^{m} \sum_{j=1, j\neq i}^{m} b_{ij} x_i x_j + \sum_{i=1}^{m} c_i x_i^2 \tag{4.2}$$

Terms with $|a_i| > 0$ or $|b_{ij}| > 0$ or $|c_i| > 0$ are included only if the model with the additional term fits the SoH data to a better accuracy, to a statistically significant extent, than the model with the corresponding term zeroed out. The implementation of the stepwise regression used the `MATLAB` `stepwiselm` function with default settings, in which the statistical criterion for inclusion of a model term is based on *"the p-value for an F-test of the change in the sum of squared error that results from adding or removing the term"*; $p > 0.1$ triggers automatic removal of the term and $p < 0.05$ triggers automatic inclusion of the term. This particular regression approach was chosen to provide a simple and repeatable model applicable to all impedance-based methods.

#### 4.3.2.4 Model validation

Cross-validation is conventionally used to assess model fit quality empirically when only one training data set is available — the data are repeatedly divided into a portion of training data used to establish fit coefficients and independent test data which are used to quantify the accuracy of that fit [160]. A four-fold cross-validation procedure is applied to each of the models, by partitioning at random the data set of experiments (in the form of ageing parameters computed for each experiment) into four

subsets (approximately 25 % of input in each). Four regression models were then trained for each method; each model successively uses one of the four subsets as test data for validation, while the model is trained on the combination of the three remaining subsets. Root mean square error (RMSE) is computed for the model SoH predictions on the test data, by comparison to the corresponding measured SoH values. The mean of the RMSE for all four trained models gives an estimate of the combined aleatoric and epistemic uncertainties for SoH estimation. This quantity is used below as a quality criterion for model comparison.

## 4.4 Development and evaluation of SoH estimation models

In this section, the proposed framework for developing an SoH estimation model (Section 4.3.2) is applied to EIS and NFRA, using the data set described in Section 4.3.1. The resulting models are evaluated, compared, and discussed in terms of their estimation accuracy, uncertainty, and practical implementation.

In the following, a model based on raw impedance data is developed and evaluated. To establish a reduced set of frequencies at which raw impedance data show a good correlation to SoH, the impedance data at all measured SoCs and frequency points were analysed against the SoH fade via Spearman rank correlation. Figure 4.4 (a) and (b) show the correlation coefficients: light colours indicate that the absolute magnitude of the correlation coefficient is close to 1, which means that impedance values in this region are strongly correlated to the SoH fade. In general, $Z'$ shows a strong correlation across a larger frequency and SoC range. This shows that $Z'$ is strongly correlated to the SoH fade at most frequencies, but the correlation is strongest for $Z'$ at high SoC and low frequency. Similarly, $Z''$ at high SoC and low frequency also shows a strong and linear correlation to the SoH fade. From this correlation analysis, the following four spectral features were identified as the best-correlated ageing parameters to the SoH fade for the direct impedance-based SoH model: 1) $Z'$ at SoC = 100 % and 0.03 Hz, 2) $Z'$ at SoC = 100 % and 0.01 Hz, 3) $Z''$ at SoC = 100 % and 0.2 Hz, 4) $Z''$ at SoC = 100 % and 0.5 Hz. All identified ageing parameters are at SoC 100 %, due to the high sensitivity towards the degradation behaviour of the battery, as also qualitatively visible from Figure 4.3. This is especially helpful in consideration of the practical implementation of the impedance-based SoH estimation, due to the straightforward experimental accessibility of the SoC 100 % state (see Section 4.3.2).

Secondly, an SoH estimation based on NFRA measurements (input data set as described in Section 4.3.1) is developed and evaluated according to the methodology of Section 4.3.2. Similar to the impedance-based model, sensitivities to SoH of the raw data (in this case, higher harmonic voltage magnitudes $Y_2$ and $Y_3$) were evaluated for data across all characterised SoCs and frequencies via Spearman rank correlation as described in Section 4.3.2 to obtain ageing parameters for the NFRA-based model. The correlation coefficients are shown in Figure 4.4 (c) and (d) and confirm

the qualitative observations (Section 4.3.1) that the NFR signals at low frequency and high SoC show the strongest correlation to the SoH fade. The following most strongly correlated ageing parameters were identified: 1) $Y_2$ at SoC 80 % and 8.13 Hz, 2) $Y_2$ at SoC 80 % and 0.25 Hz, 3) $Y_3$ at SoC 80 % and 5.89 Hz, 4) $Y_3$ at SoC 80 % and 0.25 Hz.

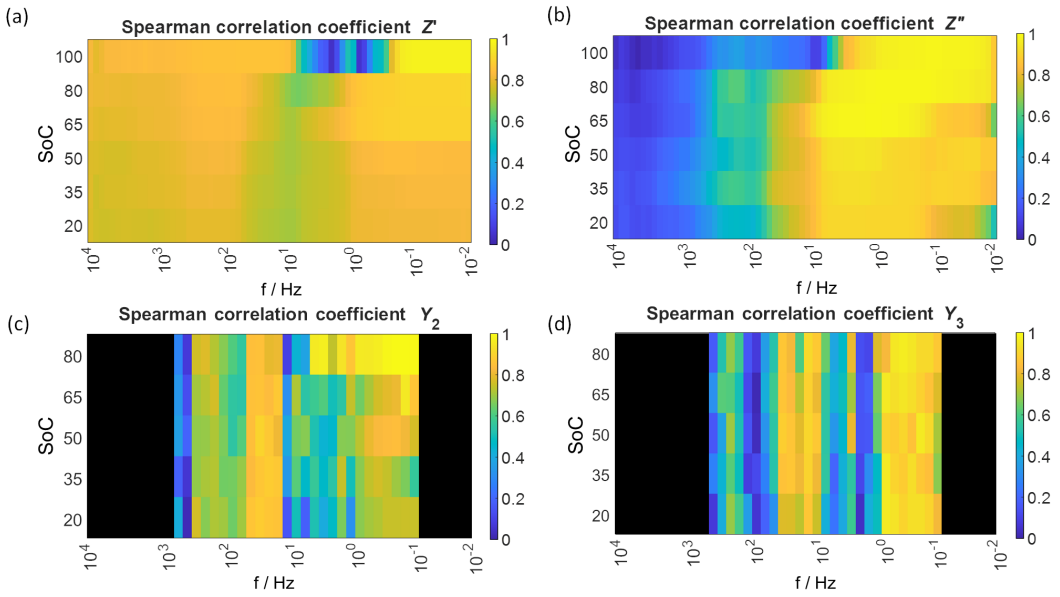


**Figure 4.4:** Absolute value of Spearman correlation coefficients for the spectral parameters of (a) $Z'$, (b) $Z''$, (c) $Y_2$ and (d) $Y_3$ to SoH as a function of frequency and SoC. Experimental data are identical to those shown in Figure 4.3. The black region of the heatmap plot indicates the unavailability of NFR data outside the NFR measurement frequency range.

Instead of taking the absolute value of the selected impedance and NFR data points as the model predictors, the model takes as input the difference between the impedance and NFR signals at a certain aged state and the initial value at a pristine state. This is to avoid the systematic error that could arise from the measurement setup, as the LCTs were conducted with different devices at different institutions.

The considered training and test data sets were the impedance spectra of the 9 batteries from four different institutions (Figure 4.1). Firstly, impedance points were selected from these data based on the four identified ageing parameters. Figure 4.5 plots the results of the four-fold cross-validation and demonstrates that an average root mean square (RMS) error of < 1 % SoH units can be attained. This suggests that a full impedance spectrum is not required; instead only a few selected impedance points, i.e., at low frequency and high SoC range, are needed to achieve an acceptable SoH prediction accuracy.

Meanwhile, the mean RMS error for SoH estimation with the NFRA-based model from four-fold cross-validation is approximately 1.1 % SoH units (Figure 4.5), which is in the same range of prediction accuracy as EIS-based approaches. Using this method would thus be feasible to estimate the SoH from a battery. Adjustment to SoC 80 % would mean that the battery need not be fully charged for the measurement; yet it would imply that the SoC can be reliably measured, e.g., by correlation to voltage. Whether an application of the method at a high SoC value of 100 % is possible without harming the battery would need to be evaluated.

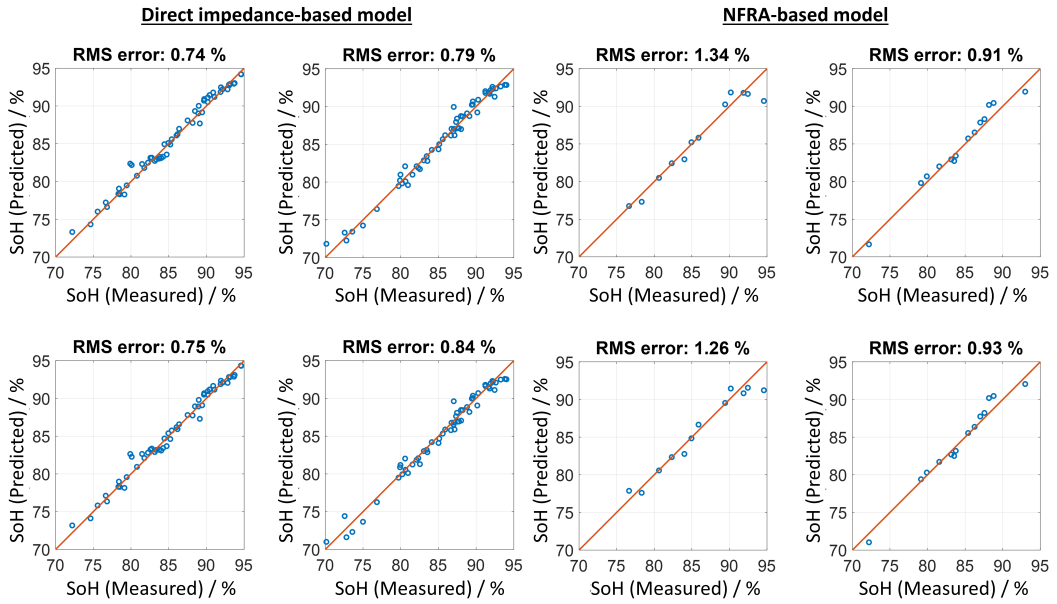


**Figure 4.5:** RMS errors of the trained linear regression model based on the identified ageing features from the direct impedance-based model (four-fold cross-validation, input at SoC 100 % only) and NFRA-based model (four-fold cross-validation, input at SoC 80 % only).

## 4.5 Comparison between EIS and NFRA-based SoH model

All models show promising performance for SoH prediction from EIS or NFRA data (four-fold cross-validation mean RMSE < 1.5 % SoH units). In absolute terms, for the specific data set used, the EIS-based SoH model offers the best SoH prediction accuracy (RMSE 0.74 % SoH units). A clear advantage of methods using raw data (EIS- and NFRA-based) is the simplicity of data gathering, as only a few discrete measurement frequencies are required, rather than a full spectrum. Moreover, no pre-processing is required. In all methods developed for data measured at a fixed SoC (SoC 100

% for EIS, SoC 80 % for NFRA), selected ageing parameters arose in the low-frequency part of the spectrum (f < 100 Hz): discrete low frequencies were selected in the EIS-based and the NFRA-based models. From the presence of significant nonlinear responses in the NFR spectra in this frequency range, the observed ageing parameters are associated with the progressive slowing of the charge transfer (lithium insertion or de-insertion) process in one of the electrodes of the battery, which is strongly correlated to its SoH fade. From frequency response data alone, it is not possible to state definitively whether these parameters measure a process responsible for SoH fade, or simply evidence a parallel degradation that is strongly correlated during continuous cycling to SoH fade arising due to other processes. The additional experimental investigation, including post-mortem analysis, is required to lend further insight.

## 4.6 Conclusion

A consolidated data set was generated by recording EIS and NFR spectra alongside coulometric measurement of SoH during life cycle testing. All SoH models demonstrate the feasibility of predicting SoH of aged batteries from rapid experiments (EIS, NFRA) alone (mean RMS error from cross-validation in the range 0.74 % to 1.34 % SoH units), once correlations have been established through life cycle testing. For models utilising measurement at only one SoC (for EIS, SoC 100 % or for NFRA, SoC 80%, obtainable by voltage measurement alone), the implied measurement time is shorter than a conventional capacity measurement (i.e., full charge-discharge cycle). Over the majority of the SoH range studied, overall SoH prediction uncertainty is principally governed by battery-to-battery variation.

It is emphasised that the predictive performance relies on a sufficient quantity of training data, gathered under a relevant ageing regime. The range of applicability of any SoH model prepared through the methodology presented here (inclusive of all data analysis methods studied) depends on the availability and quality of the training data. The proposed methodology indicates that up-front electrochemical data provision by primary producers of batteries could significantly reduce the experimental overhead for accurate characterisation of aged batteries, with concomitant advantages to LiB asset valuation and the economics of battery second use.

For future development of this work, it will be essential to establish the robustness and training data requirements for SoH models applied to more varied (realistic) cycling conditions. The preliminary data measured with the same type of batteries used here indicate that the impedance–capacity relation will vary depending on ageing conditions, including operating temperature as well as cycling regime (e.g., DoD).

Likewise, supplementary data would be required to consider other battery formats or chemistries, as well as the extent to which modules can be characterised as a whole, compared to battery-by-battery characterisation. The establishment of a consistent methodology for SoH estimation on a

battery-by-battery basis is also a useful precursor to a rigorous comparison of online SoH estimation methods as deployed at module-scale in BMS development. Such extended analyses would allow the more general applicability of this methodology to be validated, to support rapid, optimised SoH characterisation of aged batteries by utilisation of electrochemical data.

In a nutshell, I have answered the early posed research question in this chapter by proving that both EIS and NFRA are relatively good in SoH estimation with promising prediction accuracy. Again, this shows that both EIS and NFRA are equally powerful diagnostic tools for the characterisation of LiBs during ageing. Encouraged by the positive outcome via the data-driven model based on EIS and NFRA, in the next chapter, I am going to dive into a physical model-based study to explore for more potential in NFRA in deriving additional nonlinear information, which is not able to be extracted from EIS.

# 5 Mechanistic Model-based Analysis [4]

**Research question:** *What kind of additional nonlinear information could be extracted via model-assisted study?*

From the phenomenological assessment of the changes in LiB ageing behaviour with particle size distributions, harmonics arising from NFRA seem to provide additional information compared to EIS regarding changes in interfacial processes, specifically the nonlinear charge transfer process, in terms of their kinetics and symmetric behaviour during ageing. In addition, in the previous chapter, NFRA has been shown to be capable of quantifying the ageing extent of LiB, i.e., SoH estimation, with a promising prediction accuracy using the black-box approach. However, such a black-box model could not provide further details such as the underlying LiB ageing mechanisms, which could only be achieved via a physical model - the P2D battery model. For an accurate analysis, it is crucial to first parameterise the P2D battery model. In this chapter, I will demonstrate how to systematically parameterise the P2D battery model. For this, I propose a new multi-step parameterisation strategy that incorporates NFRA and I showed that via the new multi-step parameterisation strategy, a unique parameter set that better describes battery dynamics can be attained.

## 5.1 Introduction

For a reliable and accurate simulation of the battery behaviour with the P2D model, a reliable parameterisation is essential. The model parameters are either individually determined under specially designed experiments or batch-wise fitted via multistep parameterisation. Examples for the first case are the solid diffusion coefficient, which is determined via the galvanostatic intermittent titration technique (GITT) [162–164]. OCV is similarly measured via GITT and fitted in the form of the Redlich–Kister equation [76]. Solid electric conductivity can be determined using the four-point probe method [165]. Electrolyte properties such as ionic conductivities are determined in platinum microelectrode setup via EIS [75]. Lithium-ion binary diffusion coefficient and transference number are determined in lithium metal symmetrical coin cells using pulse experiments [75]. Kinetic parameters such as exchange current densities are extracted from EIS [165–167].

[4] This chapter has been published in H.S. Chan, Y.Y. Lee, D. Witt, J. Ulrich, A. Weber and U. Krewer, Batteries & Supercaps, 2025. DOI of the original article: `https://doi.org/10.1002/batt.202500179` [161].

For multistep parameterisation using electrochemical methods on a full cell, the model parameters are grouped and sequentially fitted using a series of electrochemical characterisation methods. In conjunction with this, identifiability studies for the P2D model or a simplified version—the single particle model are conducted. Laue et al. concluded that EIS is a crucial complementary electrochemical characterisation method as compared to C-rate tests, as some parameters remain ambiguous when using only the conventional OCV and C-rate parameterisations [168]. Bizeray et al. pointed out that EIS at a single SoC is not sufficient to parameterise the model due to the flat nature of the thermodynamic OCV behavior [169]. Laue et al. recommended a multistep parameterisation procedure, which includes OCV, C-rate, and EIS, for the full parameterisation of the P2D model. The author used OCV to identify mainly static parameters, such as solid concentration in electrodes; C-rate tests for quasi-static parameters, such as diffusion coefficients, tortuosities, electronic conductivities, and exchange current densities; EIS for the fine tuning of dynamic parameters, like double-layer capacitances and electronic conductivities as well as exchange current densities [65, 168]. Witt et al. extended the parameterisation strategy proposed by Laue et al. to the SEI-extended P2D model to parameterise SEI-related kinetic parameters via EIS [65].

Yet, the charge transfer coefficient is not assessable via the current parameterisation procedure even with advanced dynamic analysis such as EIS. Murbach et al. and Wolff et al. showed in their studies that the charge transfer coefficient is not sensitive to EIS [112, 113]. Murbach et al. further derived analytical solutions of the voltage response signals with respect to EIS as well as higher harmonics and showed that the charge transfer coefficient cannot be uniquely determined via EIS, but the second harmonics may allow a unique identification [113]. Alternatively, EIS with applied bias currents was shown to be able to identify the charge transfer coefficient as implemented in Ecker et al.'s work [165]. Nevertheless, this method is challenging because it infringes the time invariance criterion as SoC drifts during the measurement [165, 170]. Thus, the charge transfer coefficient is usually assumed to be constant at 0.5 in most of the simulations. Further methods were used to determine the charge transfer coefficients. The most common approach is via Tafel plot fitting at a single SoC, and the charge transfer coefficient can be assessed through the slope of the Tafel plot [171]. Hess et al. suggested that the charge transfer coefficient can be obtained through the fitting of Butler–Volmer equations using GITT measurement [172]. Also, theoretical approaches like density functional theory were used [173]. However, they require a very deep and accurate understanding of reaction and materials.

In this chapter, I perform parameterisation on a full P2D battery model with SEI, which considers, besides electrode kinetics, also the kinetics of the interfacial process at the SEI layer as well as the transport through it. To better delineate the process kinetics, I carry out parameterisation based on three-electrode measurements, which consist of OCV, C-rate tests, EIS, and NFRA. With NFRA, I target a unique and quantitative identification of the kinetic parameters, specifically the charge transfer coefficients. Firstly, the P2D-SEI model of Li-ion battery will be shortly summarised and the proposed multistep parameterisation strategy will be detailed. Next, a parameter study is carried out

to reveal the relationship between the kinetic parameters and the electrochemical response. Lastly, uniqueness analysis is conducted to reveal the significance of incorporating NFRA into the multistep parameterisation strategy.

## 5.2 Multi-step parameterisation strategy

The SEI-extended P2D model from Chapter 2.5 will be parameterised using an extended multi-step parameterisation strategy as compared to the former studies by Laue et al. [168] and Witt et al. [65]. Firstly, the multi-step parameterisation strategy begins using a low C-rate discharge (e.g. C/10) to extract information on Li inventory (cell balancing) such as maximum Li concentration in active material $c_{max}$ and SEI thickness $d_{SEI}$. Afterwards, a high C-rate discharge experiment (here: 1C, 2C) is used for parameterising Li transport parameters, for instance, solid diffusion coefficients $D_s$ and tortuosities $\tau$. Next, parameters that are sensitive to EIS are determined. These include rate constants for every interfacial reaction $k_0$, contact resistances $R_{cc}$, double-layer capacitances $C^{DL}$, solid electronic conductivities $\sigma_s$, as well as the ionic conductivity of the SEI $\kappa_{SEI}$. Lastly, I further extended the multi-step parameterisation strategy by taking NFRA into consideration. Here, kinetic parameters are refined, in particular, the charge transfer coefficient $\alpha$ is identified using its distinctive sensitivity towards the second harmonics as mentioned in [112], and the kinetic parameters obtained from the previous parameterisation step (EIS) are further fine-tuned. The proposed multi-step parameterisation strategy is illustrated in Figure 5.1.

The multi-step parameterisation strategy was performed via nonlinear least-squares optimisation in `MATLAB`. For this purpose, an objective function that describes the squared relative difference between experiment and simulation for each parameterisation step is defined. An optimal parameter set X is identified by minimising the objective function. The definition of the objective functions from step 1 to 3 of the multi-step parameterisation strategy is similar to the previous work by Witt et al. [65], where the half-cell discharge curves and EIS, in the frequency range from 5 Hz to 1 kHz, are used for parameter identification. For step 4, NFRA is used at full cell level and at positive electrode. Here, the NFR spectrum of the negative electrode is neglected as the NFR response arises mainly at low frequency range, where in the EIS, one can see a measurement artefact (see also Lee et al. [174]). Here, I assume that the NFR is also impacted. Hence, the objective function for the NFRA parameterisation is defined as follows:

$$F_{NFRA}(X) = \sum_{j\in\{full,pos\}} \sum_{k=1}^{n} \left( \frac{(Y_{2,exp,j}(k) - Y_{2,sim,j}(k))^2}{\max(Y_{2,exp,j})^2} + \frac{(Y_{3,exp,j}(k) - Y_{3,sim,j}(k))^2}{\max(Y_{3,exp,j})^2} \right) \tag{5.1}$$

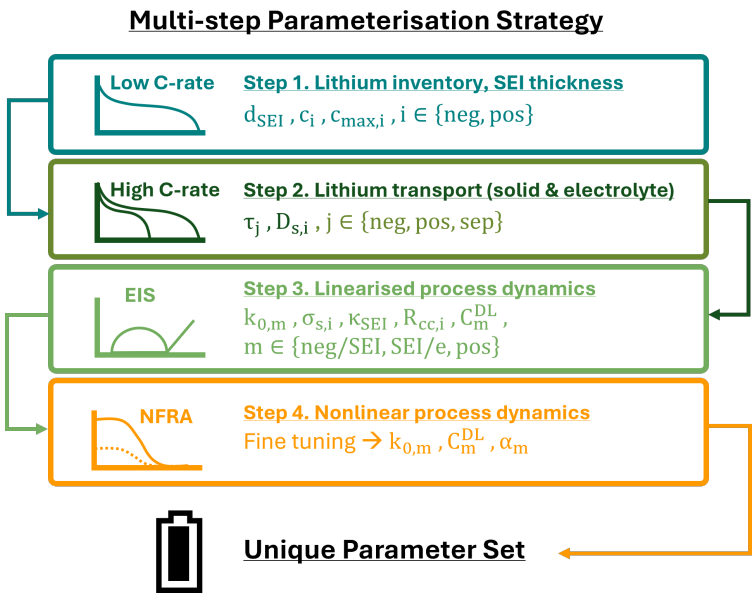


**Figure 5.1:** Multi-step parameterisation strategy with NFRA extension after C-rate and EIS parameterisation for the P2D-SEI model.

n frequencies between 1 Hz and 300 Hz at full cell level as well as at half-cell positive electrode are considered.

## 5.3 Uniqueness analysis

The uniqueness of the identified kinetic parameters from parameterisation without NFRA, i.e. omitting the last parameterisation step, is evaluated. Similar to the work by Laue et al. [168], an indirect sample-based identifiability test is used. In this approach, EIS is simulated via various combinations of parameter sets, which are iteratively sampled in a defined parameter space $\Omega$. Here, all other parameters are kept constant to the identified parameter set while kinetic parameters (rate constant $k_0$ and charge transfer coefficient $\alpha$) are investigated due to the qualitatively similar impact on EIS spectra. In this study, $k_0$ varies by orders of magnitude and the corresponding parameter space is logarithmically varied while $\alpha$ is equidistantly varied.

$$\Omega_\alpha \in [\alpha_{min}, \alpha_{max}] \tag{5.2}$$

$$\Omega_{k_0} \in [\log k_{0,min}, \log k_{0,max}] \tag{5.3}$$

Each parameter range is discretised into 50 points. This results in 50×50 combinations of $\alpha$ and $k_0$, for a total of 2500 EIS simulations. In these simulations, EIS spectra are simulated with the same frequency points as the experiment, i.e., 10 points per decade above 66 Hz and 5 points per decade below 66 Hz. The residuum between the simulated and the experimental EIS spectra is summed over the probed frequencies $f_i$ for each parameter sample. A parameter is not unique when more than one set of parameter variations show a similar residuum $\Delta Z$.

$$\Delta Z = \sum_{i=1}^{m} \sqrt{\left(Z'_{sim}(f_i) - Z'_{exp}(f_i)\right)^2 + \left(Z''_{sim}(f_i) - Z''_{exp}(f_i)\right)^2} \tag{5.4}$$

All simulations in this work, including multi-step parameterisation and uniqueness analysis, are performed in `MATLAB` (MathWorks, version. R2019b or later).

## 5.4 Experiment

The measurement in this chapter was performed by Y.Y. Lee. A three-electrode setup (PAT-Cell) from EL-Cell GmbH was built with electrode materials, i.e., lithium nickel manganese cobalt oxides - 811 for the positive electrode and blends of silicon-graphite for the negative electrode (Si content estimated as $2.8 \pm 0.5$ wt. % from post mortem SEM-EDX analysis), extracted from a commercial cylindrical cell (LG 18650 HG2), which has a nominal capacity of 3 A h. This is the same cell that has been studied in Chapter 4. The extracted electrode materials were double-sided coated and therefore, one side of the electrode coating was removed using N-Methyl-2-Pyrrolidone. After that, the electrode was rinsed several times with dimethyl carbonate and dried under an argon atmosphere before punching into discs with a diameter of 18 mm for the PAT-Cell set-up. A 220 µm thick commercial separator (EL-CELL GmbH, ECC1-00-0210 V/X) of polypropylene and polyethylene with a built-in lithium reference ring was used. 103 µL mixtures of ethylene carbonate and dimethyl carbonate with a ratio of 1:1 (v/v) and 1M lithium hexafluorophosphate were used as the electrolyte. The whole cell assembly process was done inside an argon-filled glovebox ($O_2$ and $H_2O < 0.1$ ppm). After that, the cell was first rested for 12 hours in a temperature chamber (MMM Friocell 55) at 25 °C and then subjected to formation and cycled using a battery cycler (BaSyTec CTS Lab). During the formation step, the cells were charged and discharged with C/10 without a constant voltage (CV) phase for two cycles; in the third cycle, a constant current followed by CV until C/20 was applied in the charge direction between 3.0 V and 4.2 V at 25 °C. Next, a C-rate test was performed on the cell via a similar measurement setup. After a rest time, EIS and NFRA measurements were carried out using a Zahner Zennium potentiostat under galvanostatic mode. The measurement parameters for the characterisations are shown in Table 5.1.

**Table 5.1:** Measurement parameter and condition for the C-rate test, EIS and NFRA.

| **C-rate test** | | |
|---|---|---|
| Voltage range | 3.0 V to 4.2 V | |
| Charge current[a] | C/2 (CC-CV, current cut-off at C/20) | |
| Discharge current[a] | C/2, 1C, 2C (CC) | |
| Temperature | 25 °C | |
| | **EIS** | **NFRA** |
| Excitation amplitude | 500 µA (C/12) | 10 mA (1.5C) |
| Frequency range | 10 mHz to 1 MHz | 100 mHz to 1 kHz |
| Voltage | 4.151 V(about SoC 90 %) | |
| Temperature | 23 °C | |

[a] dis-/charge current is defined according to the measured capacity of the cell after formation.

## 5.5 Parameter and state analysis

In this section, the quality of the result from the multi-step parameterisation strategy will be analysed. Next, a parameter study is performed based on the obtained parameter set for the given battery, followed by a uniqueness evaluation to check the sensitivity and uniqueness of the obtained parameter set based on the proposed parameterisation strategy.

### 5.5.1 Parameterisation results via multi-step parameterisation strategy

Via the proposed parameterisation strategy, a parameter set that can reproduce the experimental discharge behaviour at different C-rates, EIS and NFRA in both, full-cell and half-cells, is identified and the comparison between the simulation and the experimental curves is depicted in Figure 5.2. Table 5.2 shows the important parameters that were obtained from the multi-step parameterisation. A complete parameter set can be found in Appendix A.3.

From Figure 5.2 (a), (d) and (g), one can observe that a good agreement between simulated and experimental discharge behaviour at different C-rates is obtained in full-cell as well as half-cell. Meanwhile, a promising match between simulated and experimental EIS and NFR spectra at the full-cell level is shown in Figure 5.2 (b) and (c). Note that at the negative electrode, a measurement artefact, i.e., inductive loop, arises in the frequency range below 10 Hz as shown in Figure 5.2 (e). These are known to occur for many measurements with Li reference electrode, also in this set-up [174]. Therefore, parameterisation of the half-cell level especially at the negative electrode is not reliable and will

not be focused here. The region, where the measurement artefact arises, is highlighted in red in the corresponding NFR spectrum in Figure 5.2 (f).

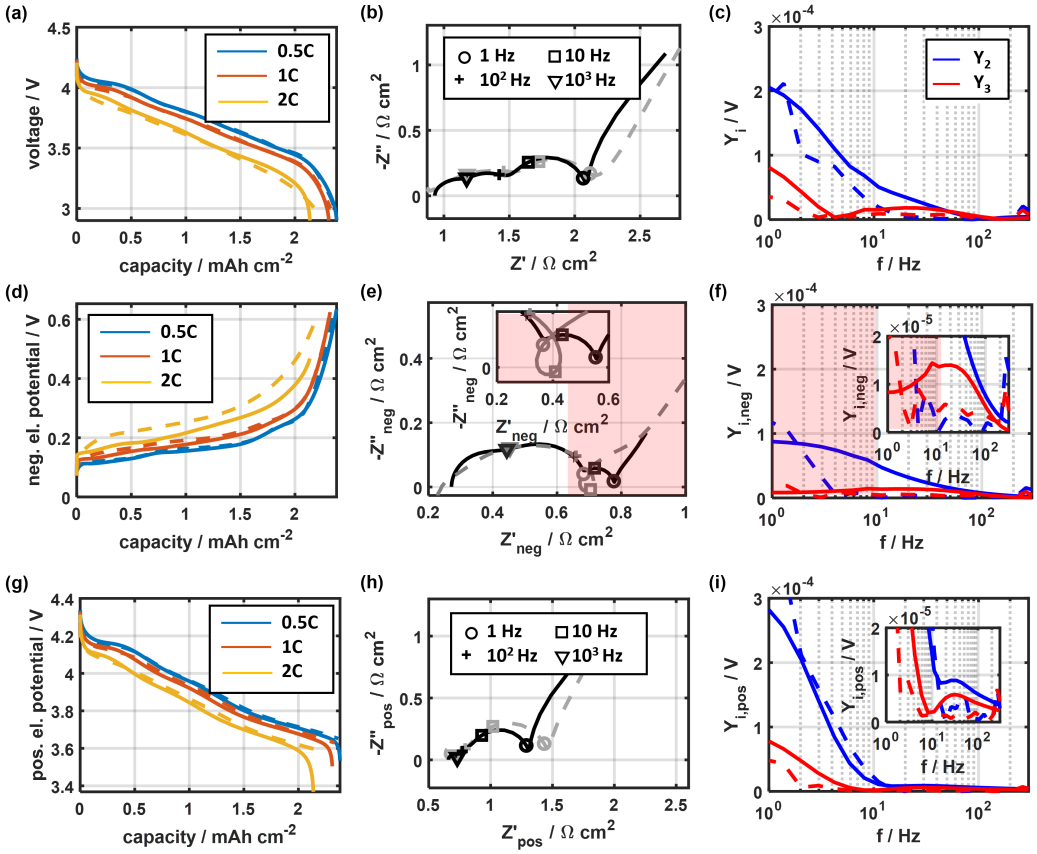


**Figure 5.2:** Simulation results reproducing experimental characterisation after multi-step parameterisation strategy: discharge curves at 0.5C, 1C and 2C, EIS and NFRA at SoC 90% in full cell (a) – (c), negative electrode (d) – (f) and positive electrode (g) – (i). Solid lines indicate the simulated and dashed lines the experimental results. The red-highlighted regions indicate the region that corresponds to the frequency range of EIS, in which the measurement artefacts, i.e., inductive loops appear (see inset of (e)).

Furthermore, it is noted that the charge transfer coefficient for the de-/intercalation at the positive electrode, which is additionally parameterised via NFRA, is no longer 0.50 but 0.55. By comparing the full-cell and half-cells EIS and NFR spectra, an assignment of the underlying processes is possible and interpreted according to the work by Lee et al. [174]. Firstly, one could notice the full-cell EIS comprises three semicircles, and the diffusion arc starts below 1 Hz (Figure 5.2 (b)). The low-frequency semicircle (1 Hz – $10^2$ Hz) is predominantly impacted by the positive electrode and only slightly from the negative electrode. By comparing with the NFR spectra, one can identify that the process within this frequency range is a charge transfer process as nonlinear signals are visible in the

**Table 5.2:** List of parameters obtained from the multi-step parameterisation strategy.

| Parameter | Unit | Negative | Separator | Positive |
|---|---|---|---|---|
| Maximum active material concentration, $c_{s,max}$ | $mol\,m^{-3}$ | 33345 | - | 29822 |
| Initial active material concentration, $c_{s,0}$ | $mol\,m^{-3}$ | 32629 | - | 1524 |
| Solid diffusion coefficient, $D_s$ | $m^2\,s^{-1}$ | $1.8 \cdot 10^{-14}$ | - | $3.0 \cdot 10^{-15}$ |
| Tortuosity, $\tau$ | - | 14.25 | 1.36 | 4.44 |
| Electrical conductivity, $\sigma_s$ | $S\,m^{-1}$ | 209.6 | - | 0.07 |
| Contact resistance, $R_{cc}$ | $\Omega\,m^2$ | $1.5 \cdot 10^{-4}$ | - | $6.9 \cdot 10^{-5}$ |
| SEI thickness, $d_{SEI}$ | nm | 85.8 | - | |
| Reaction rate constant, $k_0$ | $s^{-1}$ (negative)<br>$m\,s^{-1}$ (positive) | 30 (neg/SEI)<br>$3.0 \cdot 10^6$ (SEI/e) | - | $2.6 \cdot 10^{-9}$ |
| Double-layer capacitance, $C^{DL}$ | $F\,m^{-2}$ | 20 (neg/SEI)<br>0.41 (SEI/e) | - | 2 |
| Charge transfer coefficient, $\alpha$ | - | 0.50 (neg/SEI)<br>0.50 (SEI/e) | - | 0.55 |

designated frequency range. Meanwhile, the mid-frequency ($10^2$ Hz – $10^3$ Hz) and high-frequency semicircles (above $10^3$ Hz) in the full-cell EIS originate mainly from the negative electrode. Similar findings have also been reported in other publication [26, 174]. As these processes do not show nonlinearities in the NFR spectrum, linear processes can be assigned to these semicircles: $10^2$ Hz – $10^3$ Hz is the ad-/desorption process at the SEI/electrolyte interphase and across the SEI layer. Further, the process above $10^3$ Hz is attributed to the contact resistance between active material particles as well as at current collectors. The assignment of this frequency range to the contact resistance can also be observed in other publications [129, 175].

As mentioned previously in the multi-step parameterisation, kinetic parameters have been refined via NFRA. In the next section, I am going to study how these kinetic parameters influence the different characterisation methods, i.e., C-rate, EIS and NFRA.

### 5.5.2 Kinetic parameter study

To gain a deeper understanding of the relationship between kinetic parameters and different characterisation methods, a parameter study focusing on the kinetic parameter is performed.

As shown in Figure 5.3 (a) to (c), the rate constant of the charge transfer process at the positive electrode $k_{0,pos}$ has a significant impact on the frequency response analysis; this is especially notable in the frequency range attributed to the charge transfer process at the positive electrode (1 Hz to 10 Hz) for EIS and NFRA. In contrast, it has a negligible impact on the C-rate performance and impacts mainly at higher C-rate. By lowering $k_{0,pos}$, the impedance and NFR signals increase due to

the decrease in the exchange current density, thus, leading to an increase in the overpotential for the respective process.

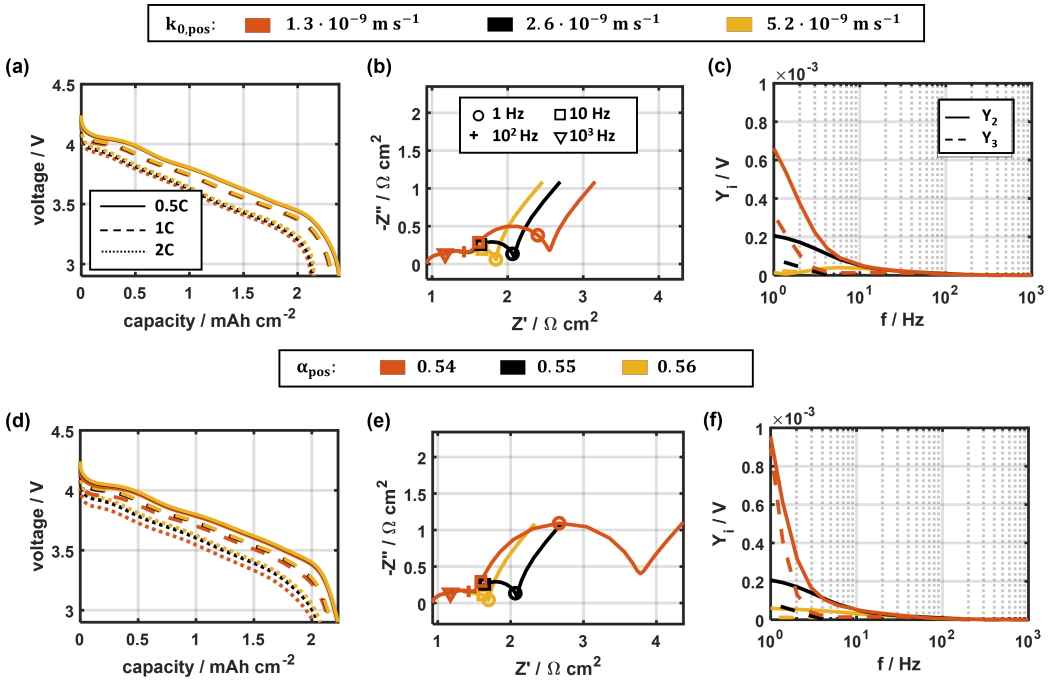


**Figure 5.3:** The impact of the rate constant of the de-/intercalation process at the positive electrode $k_{0,pos}$ (a - c) and the charge transfer coefficient at the positive electrode $\alpha_{pos}$ on full cell (d) C-rates, (e) EIS, (f) NFRA at SoC 90%.

Besides the rate constant, it is also interesting to study the impact of the charge transfer coefficient at the positive electrode $\alpha_{pos}$ as the parameterisation has resulted in a value of 0.55, not 0.50. As shown in Figure 5.3 (d) to (f), a slight change in $\alpha_{pos}$ shows a stronger impact than $k_{0,pos}$ as $\alpha_{pos}$ appears as an exponent in the exchange current density exponent as compared to the linearly related $k_{0,pos}$. In general, impedance and NFR signals, predominantly between 1 Hz and 10 Hz, increase significantly. Also, the discharge behaviour at different C-rates is impacted. It shows a stronger drop in the initial voltage and hence a vertical shift of the voltage profile when $\alpha_{pos}$ decreases.

Here, the variation in $\alpha_{pos}$ impacts all frequency responses in EIS and NFRA unlike previous findings by Wolff et al. [112] and Murbach et al. [113, 114], which showed that $\alpha_{pos}$ has distinct sensitivity towards second harmonics only. This is because the expression for the exchange current density used in this work is different from the above-mentioned publications. The exchange current density implemented by Wolff et al. and Murbach et al. is a constant. Meanwhile, here, the exchange current density is dependent on species concentrations and $\alpha_{pos}$, considering the kinetics of the involved species at the interfaces as proposed by Doyle & Newman [50] and Smith & Wang's prior work

[176, 177]. Therefore, a variation in $\alpha_{pos}$ not only changes the charge transfer symmetry – $Y_2$ but also affects the kinetics, i.e., high $\alpha_{pos}$ leads to large exchange current density, thus, small overpotential, impedance and $Y_3$.

In addition, contrary to the work by Wolff et al., the variation in $k_{0,pos}$ is also shown to be impacting not only EIS and $Y_3$ but also $Y_2$ in NFRA. This is because the parameter study here is performed based on the asymmetrical case, i.e. $\alpha_{pos}$ is equal to 0.55. If $\alpha_{pos}$ is set to 0.50, $k_{0,pos}$ only impacts EIS and $Y_3$ in NFRA while $Y_2$ remains the same, which is similar to Wolff et al. [112].

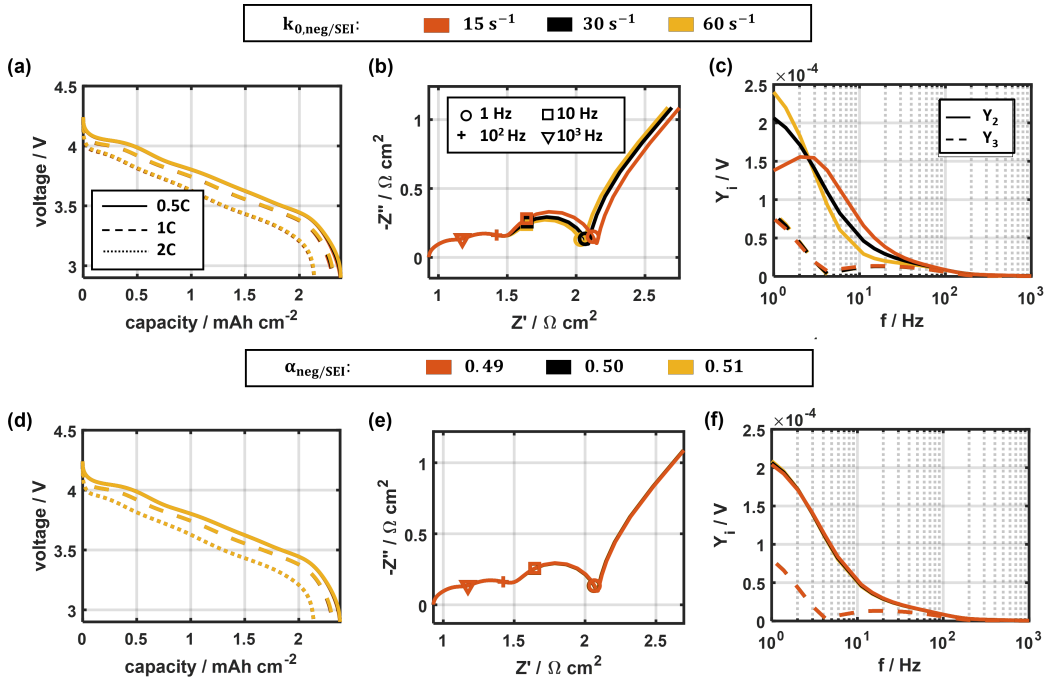


**Figure 5.4:** The impact of the rate constant of the de-/intercalation process at the negative electrode $k_{0,neg/SEI}$ (a - c) and the charge transfer coefficient at the negative electrode $\alpha_{neg/SEI}$ on full cell (d) C-rates, (e) EIS, (f) NFRA at SoC 90%.

The rate constant of the de-/intercalation process at the negative electrode $k_{0,neg/SEI}$ is not as sensitive as the positive electrode for the investigated cell here. In Figure 5.4 (a) to (c), one can notice that with the same relative variation in $k_{0,neg/SEI}$ as $k_{0,pos}$, there is no visible change in the C-rate simulation while there is only a slight increase in the EIS and NFR signals in the frequency range attributed to the charge transfer process at the negative electrode (1 Hz – $10^2$ Hz) when decreasing the rate constant. It is also shown here that $k_{0,neg/SEI}$ simultaneously impacts $Y_2$ besides EIS and $Y_3$, although $\alpha_{neg/SEI}$ equals 0.50 in this parameter study. This is because the rate expression used for the charge transfer process here, unlike Butler-Volmer equation, is not symmetrical in nature.

Further, as shown in Figure 5.4 (d) to (f), the charge transfer coefficient $\alpha_{neg/SEI}$ is not as sensitive as compared to $\alpha_{pos}$: It is shown that a similar quantitative change in $\alpha_{neg/SEI}$ as $\alpha_{pos}$ does not result in any change in C-rates, EIS and NFR spectra.

Meanwhile, a change in the rate constant of the ad-/desorption process between the electrolyte and SEI layer $k_{0,SEI/e}$ has stronger sensitivity than $k_{0,neg/SEI}$. Especially, it shows higher sensitivity in EIS and NFRA than C-rate performance as can be seen in Figure 5.5 (a) to (c). A decrease in $k_{0,SEI/e}$ results in an increase in the high frequency ($10^2$ Hz – $10^3$ Hz) semicircles in EIS, indicating that the process at the SEI/electrolyte interphase is impacted. It is also shown that the impedance of the de-/intercalation at the negative electrode (1 Hz – $10^2$ Hz) is mainly shifted horizontally towards a higher impedance but not increase in semicircle. This indicates that a change in ad-/desorption process at SEI/electrolyte shifts the quasi-steady state but does not change the dynamic of the de-/intercalation at the negative electrode.

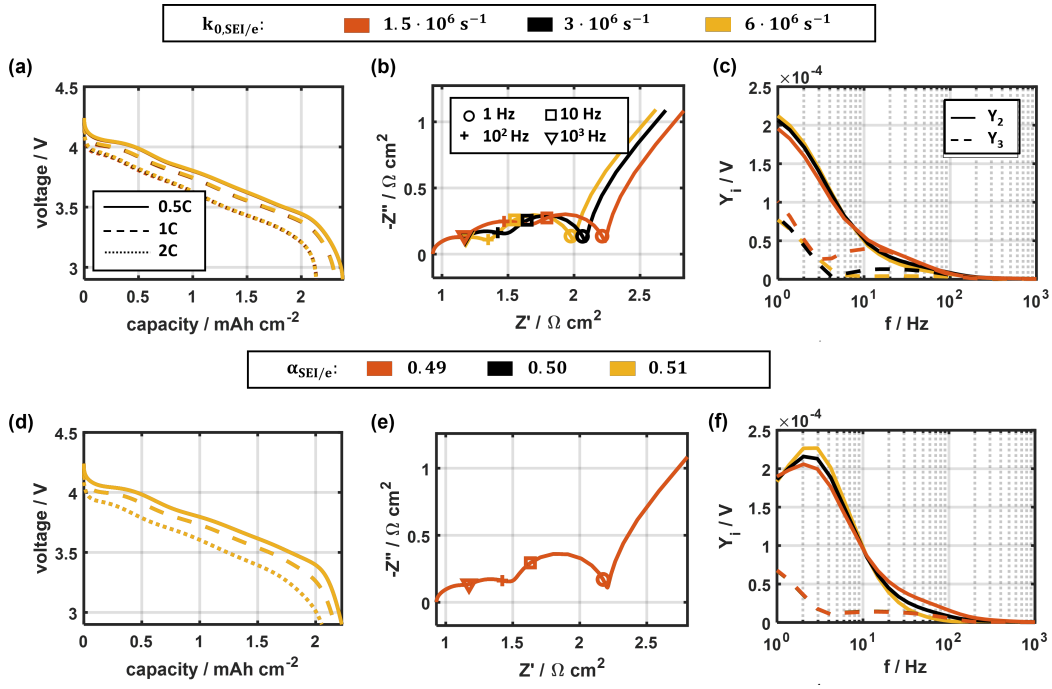


**Figure 5.5:** The impact of the rate constant of the ad-/desorption process at the SEI layer $k_{0,SEI/e}$ (a - c) and the charge transfer coefficient at the SEI layer $\alpha_{SEI/e}$ on full cell (d) C-rates, (e) EIS, (f) NFRA at SoC 90%.

A variation in the charge transfer coefficient in the corresponding process $\alpha_{SEI/e}$ with the similar extent as $\alpha_{pos}$ and $\alpha_{neg/SEI}$ also shows a slight impact mainly on NFRA ($Y_2$) as shown in Figure 5.5 (f), which indicates mainly the charge transfer symmetry is affected. This outcome agrees with the

finding of Wolff et al. [112] and Murbach et al. [113, 114] that a change in charge transfer coefficient impacts only the second harmonics.

From the parameterisation above, one could notice that for the analysed cell the kinetic parameters at the negative electrode are not as sensitive as at the positive electrode. Furthermore, it could be seen that the C-rate has a comparably lower sensitivity to the kinetic parameters. Therefore, EIS and NFRA are essential tools to identify these kinetic parameters. In general, the kinetic parameters, i.e. the rate constant and the charge transfer coefficient manifest complicated interactions in EIS and NFRA. Thus, in the subsequent section, a uniqueness study is carried out to distinguish the impact of the charge transfer coefficient and at the same time to demonstrate how to best identify these kinetic parameters.

### 5.5.3 Uniqueness study

To understand how unique is the parameter set obtained from the multi-step parameterisation strategy and how to best identify the kinetic parameters, a uniqueness study is conducted. In the work by Laue et al. [168], such a study was performed on the C-rate test to resolve the identifiability of selected transport parameters such as solid diffusion coefficient and electronic conduction; in this study, I focus the uniqueness study on EIS to investigate the identifiability of the kinetic parameters, i.e. the rate constants and charge transfer coefficients.

Here, the identified parameter set is taken as the reference case. The rate constant and charge transfer coefficient are varied while all other parameters are kept constant. The outcome of the EIS simulation is then compared using the residual calculation defined in method section. Additionally, for EIS simulations with similar low residuals, the corresponding NFR spectra are further simulated and compared.

Firstly, Figure 5.6 shows the outcome of the uniqueness study on EIS based on the kinetic parameters at the positive electrode, i.e. rate constant $k_{0,pos}$ and charge transfer coefficient $\alpha_{pos}$. From Figure 5.6 (a), one could notice a dark blue diagonal line, which gives similarly minimal residuals. This means that multiple pairs of $k_{0,pos}$ and $\alpha_{pos}$ with the identified parameter set could deliver simulated full-cell EIS that best match with experimental ones. $k_{0,pos}$ and $\alpha_{pos}$ are thus not identifiable with EIS only. To further illustrate this, C-rate tests, EIS and NFR spectra are simulated based on several pairs of $k_{0,pos}$ and $\alpha_{pos}$ that lie along the dark blue diagonal line as shown in Figure 5.6 (a). As expected, the EIS spectra with the selected $k_{0,pos}$ and $\alpha_{pos}$ pairs show no difference and give a good match to the experimental data (Figure 5.6 (c)). There are also only marginal differences in the C-rate performance (Figure 5.6 (b)). In NFR spectra, as shown in Figure 5.6 (d) inset, $Y_3$ is the same as EIS. Meanwhile, $Y_2$ shows changes with a minimum when $\alpha_{pos}$ approaches 0.50. In particular, one could see that $\alpha_{pos}$ = 0.55 could give a qualitative good agreement to the experimental $Y_2$. This further shows that NFRA could further refine a more unique parameter set that is obtained with EIS.

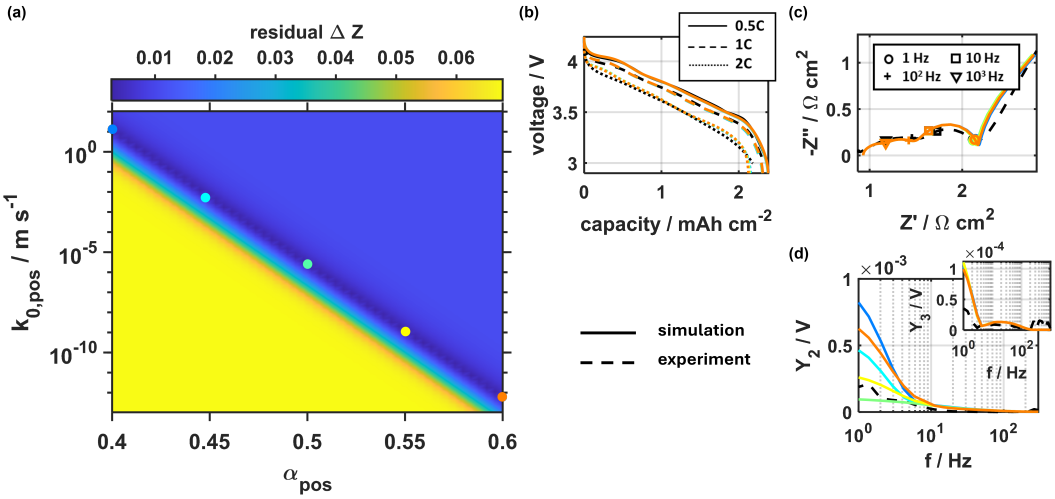


**Figure 5.6:** Uniqueness analysis based on the variation of the kinetic parameters at positive electrode, i.e. rate constant $k_{0,pos}$ and charge transfer coefficient $\alpha_{pos}$: (a) residuals from the difference between simulated and experimental full-cell EIS, respective simulated and experimental (b) discharge curves at several C-rates, (c) EIS and (d) NFR spectra at SoC 90% based on the selected $k_{0,pos}$ and $\alpha_{pos}$ pairs along the dark blue diagonal line.

Next, Figure 5.7 shows the result of the uniqueness study on EIS based on the kinetic parameters at the negative electrode: rate constant $k_{0,neg/SEI}$ and charge transfer coefficient $\alpha_{neg/SEI}$. Similar to the positive electrode, the result also shows a dark blue line that gives minimal residual from the comparison between simulated and experimental full-cell EIS (Figure 5.7 (a)). However, in this case, $k_{0,neg/SEI}$ varies only slightly between $13\,s^{-1}$ and $20\,s^{-1}$. On the contrary, multiple optimal $\alpha_{neg/SEI}$ exist that give simulated EIS that match to experiments. Hence, $k_{0,neg/SEI}$ can be better determined as compared to $\alpha_{neg/SEI}$. Figure 5.7 (b) to (d) show further the simulated curves based on $k_{0,neg/SEI}$ and $\alpha_{neg/SEI}$ pairs that lie along the dark blue diagonal line. C-rate performance, EIS and NFR spectra remain unchanged and give good match to the experimental result. This outcome matches well with the kinetic parameter study as shown previously that for the current cell $\alpha_{neg/SEI}$ is insensitive to both EIS and NFRA characterisation methods. Thus, it cannot be identified via these methods.

Meanwhile, the result of the uniqueness study of the kinetic parameters at the SEI/electrolyte interphase, rate constant $k_{0,SEI/e}$ and charge transfer coefficient $\alpha_{SEI/e}$, is depicted in Figure 5.8. The result is similar to the uniqueness outcome of the kinetic parameters at the negative electrode: the optimal $k_{0,SEI/e}$ of about $3 \times 10^{6}\,s^{-1}$ is identified via EIS parameterisation whereas $\alpha_{SEI/e}$ could not be identified by EIS alone. Figure 5.8 (b) to (d) show the simulated C-rate performance, EIS and NFR spectra based on the selected $k_{0,SEI/e}$ and $\alpha_{SEI/e}$ pairs that lie along the dark blue line. It is shown that $\alpha_{SEI/e}$ is possible to be determined via $Y_2$, as $Y_2$ varies with the change in $\alpha_{SEI/e}$ while C-rate tests, EIS and $Y_3$ remain almost constant. Here, it can be seen that $\alpha_{SEI/e}$ is identified to be 0.50 that gives the best match to the experimental results.

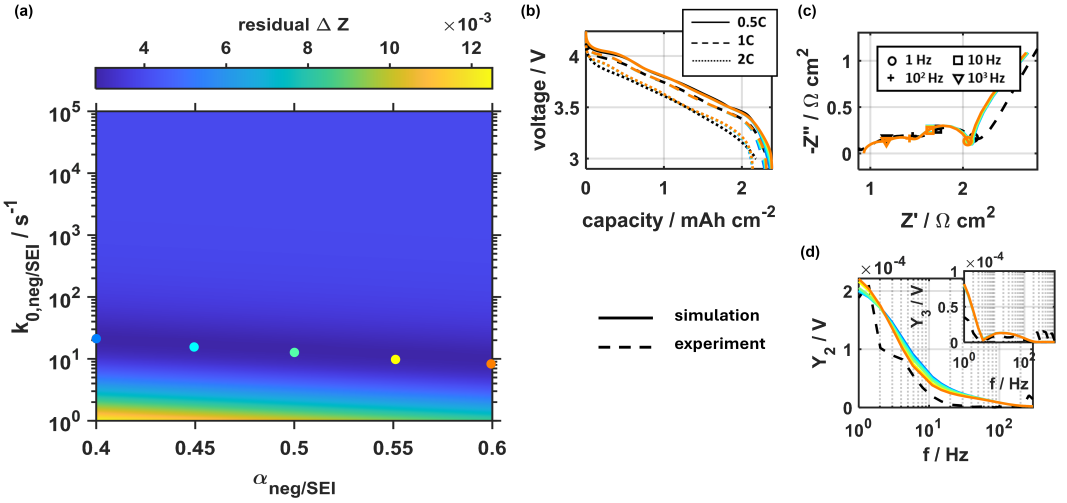


**Figure 5.7:** Uniqueness analysis based on the variation of the kinetic parameters at negative electrode, i.e. rate constant $k_{0,neg/SEI}$ and charge transfer coefficient $\alpha_{neg/SEI}$: (a) residuals from the difference between simulated and experimental full-cell EIS, respective simulated and experimental (b) discharge curves at several C-rates, (c) EIS and (d) NFR spectra at SoC 90% based on the selected $k_{0,neg/SEI}$ and $\alpha_{neg/SEI}$ pairs along the dark blue diagonal line.

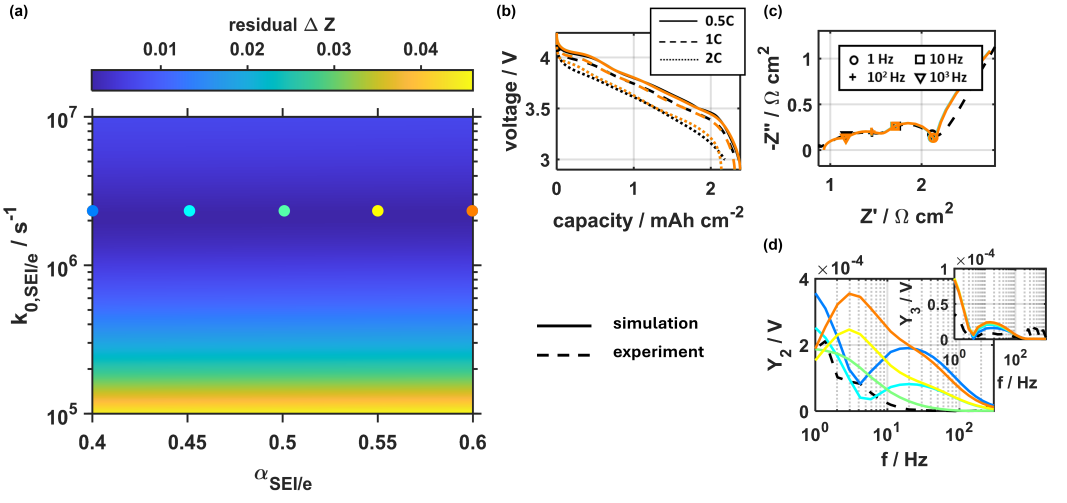


**Figure 5.8:** Uniqueness analysis based on the variation of the kinetic parameters at SEI interphase, i.e. rate constant $k_{0,SEI/e}$ and charge transfer coefficient $\alpha_{SEI/e}$: (a) residuals from the difference between simulated and experimental full-cell EIS, respective simulated and experimental (b) discharge curves at several C-rates, (c) EIS and (d) NFR spectra at SoC 90% based on the selected $k_{0,SEI/e}$ and $\alpha_{SEI/e}$ pairs along the dark blue diagonal line.

In conclusion, the kinetic parameter pairs at the positive electrode requires both EIS and NFRA methods for a unique identification. At the negative electrode/SEI interphase as well as SEI/electrolyte interphase, the rate constant can be identified by EIS. The charge transfer coefficient at the SEI/electrolyte interphase can be further identified via NFRA whereas the charge transfer coefficient at the negative electrode is insensitive to either EIS or NFRA method, therefore it cannot be identified here. It should be noted that here obtained sensitivities may be cell-specific, i.e. a change in active material or cell balancing might lead to different limitations and sensitivities.

### 5.5.4 Comparison to literature values

In the following, the charge transfer coefficients that were obtained from the multi-step parameterisation strategy will be compared with the literature values.

For positive electrode, the obtained charge transfer coefficient in this work (0.55) coincides with the reported ranges of charge transfer coefficients (0.48 – 0.58) regardless of the active materials. For instance, Hess et al. reported a charge transfer coefficient between 0.56 and 0.58 for lithium cobalt oxides (via GITT analysis) [172] and Heubner et al. obtained a charge transfer coefficient of 0.55 for lithium iron phosphates via Tafel plot analysis [178]. Ecker et al. determined a charge transfer coefficient of 0.517 for lithium nickel cobalt oxide using EIS superimposed with different bias currents and fit the charge transfer resistance with the Butler-Volmer equation [165]. Recently, Kirk et al. reported a small charge transfer coefficient of 0.48 via parameterisation of Single Particle Model [179]. Nevertheless, the author only performed parameterisation on full cell measurement as half-cell measurements are not assessable in commercial cell. Ji et al. identified a change in charge transfer coefficient from 0.50 to 0.61 for mixed lithium nickel manganese cobalt oxide with lithium manganese oxide when the cell aged [119]. However, there are only few works reported on the charge transfer coefficient for the active material – lithium nickel manganese cobalt oxides - 811.

For negative electrode, there are discrepancies between the obtained charge transfer coefficient in this work (0.50) and the reported literature values (0.28 – 2.03). The reported charge transfer coefficients vary more significantly as compared to the one of positive electrode. Piao et al. used a charge transfer coefficient dependent exchange current density. By measuring and fitting the exchange current densities at different lithium concentrations in graphite and in electrolyte, a charge transfer coefficient of 0.65 is determined [180]. Via the similar method, Chang et al. obtained the same charge transfer coefficient of 0.65 for graphite electrode [181]. Meanwhile, Dokko et al. used tafel analysis method and found out a range of charge transfer coefficients between 0.28 and 0.40 depending on the lithium concentration in the graphite electrode [171]. Ecker et al. found a charge transfer coefficient of 0.489 for the graphitic electrode via EIS with DC biased [165]. Nevertheless, there are very little studies on the kinetic characterisation of the silicon-graphitic electrode. For example, Durdel et al. performed kinetic characterisation on silicon-graphitic electrode (Si – 69.7 wt.%) and determined a

charge transfer coefficient of 0.50 [182]. Meanwhile, Chandrasekaran et al. identified a charge transfer coefficient of 2.03 for silicon electrode, which is much larger than the graphite electrode [183]. In general, for the graphite negative electrode, it is shown that there are widespread values for the charge transfer coefficient. This indicates that, as shown in this work, the charge transfer coefficient for the negative electrode cannot be easily determined.

On the contrary, the charge transfer coefficient for the reaction at SEI/electrolyte interphase was barely investigated and mostly assumed to be symmetric: $\alpha_{\mathrm{SEI/e}} = 0.50$ [184–186]. Only one work by Kindermann et al. that took asymmetrical charge transfer coefficient (0.95) in the established SEI growth model [60]. Nonetheless, the model that established in this work differentiates from the model by Kindermann et al. as here I focus on state estimation of the battery rather than a SEI growth degradation model of the battery. Also, Kindermann et al. did not parameterise the charge transfer coefficient but rather assumed a highly irreversibility of the degradation process by taking a large charge transfer coefficient. Therefore, discrepancy in the charge transfer coefficient arises, and the charge transfer coefficient for the ad-/desorption process at the SEI/electrolyte interphase is for the first-time in this work determined.

### 5.5.5 Conclusion

In this chapter, the multi-step parameterisation strategy for enhanced estimation of the kinetic parameter in the battery model has been introduced. It is shown in the uniqueness study that the kinetic parameter set obtained via EIS only is not unique, i.e. several pairs of rate constant and charge transfer coefficient can reproduce the experimental EIS. However, it can be improved by extending the parameterisation procedure to include EIS and NFRA. With EIS+NFRA parameterisation, the charge transfer coefficient can be further fine-tuned via $Y_2$.

The kinetics at the negative electrode for the investigated cell here shows comparably low sensitivity compared to the positive electrode. As a result, the low sensitivity increases the uncertainty of the obtained parameter set at the negative electrode. To enhance the sensitivity, EIS and NFRA characterisations can be performed at different SoC as shown in the previous chapter the EIS and NFR spectra appear to be different at different SoC. Also, a possible future investigation could include the sensitivity analysis of the phase of the harmonics as well.

Furthermore, measurement artefacts like inductive loops, as shown in the half-cell data of the negative electrode exist, which might affect the accuracy of the parameterisation outcome, not only impacting the negative electrode but also the positive electrode as well. Half-cell measurements from symmetrical cells can be conducted with NFRA also, which could theoretically eliminate the measurement artefact. Yet, the second harmonic in this case will be cancelled out [174]. Therefore, parameterisation via symmetrical cell configuration will not benefit from NFRA. As an outlook, for a unique parameterisation of Li-ion battery which incorporates NFRA, another approach of half-cell

measurements has to be developed, which has to be free from measurement artefacts, for example, a three-electrode set-up with meshed reference electrode [187].

In summary, I can conclude that by incorporating NFRA, a more unique parameter set could be attained. Simultaneously, additional information about the charge transfer coefficient can be determined via NFRA. Hence, I thereby answered the proposed research question and also showed the uniqueness and importance of NFRA as compared to other characterisation methods. With the fully parameterised battery model, a useful predictions on the battery behaviours such as ageing under a defined circumstance can made. Also, the root causes of the battery ageing can be captured and thus, minimise the ageing by optimising the operational strategy of the battery. In the subsequent chapter, I will be using the parameterised battery model to systematically assess the different degradation modes that results in the ageing of LiBs. In particular, I am going to observe how the different degradation modes in LiBs affect discharge behaviour, EIS and NFRA respectively.

# 6 Model-assisted Ageing Analysis

**Research question:** *How can the combination of EIS and NFRA help in studying the ageing phenomenon of LiBs via modelling?*

In Chapter 4, I have established a black-box model based on NFRA, which could estimate the SoH of a battery with promising accuracy. Before analysing the ageing mechanism of LiBs in more detail, I have parameterised the P2D battery model with additional NFR data as described in Chapter 5 and showed that the battery model can only be uniquely parameterised with the help of additional information offered by NFRA. Now, with this parameterised P2D battery model, I am going to go deeper into studying the ageing behaviour of LiB. In this chapter, a parameter study will be firstly performed. Specifically, selected battery parameters are varied to resemble the different degradation modes and the respective changes in the discharge behaviour, EIS and NFRA are observed and discussed. Learnt from the parameter study outcome, the possible degradation modes in the ageing of the real 18650 cell as observed in Chapter 4 are hypothesised and quantitatively reproduced to estimate the actual degradation in the cell.

## 6.1 Parametric ageing study

A conceptual parametric ageing study is performed using the parameterised battery model. Here, different ageing scenarios such as loss of active material, increase in SEI thickness, etc. are simulated to study their impacts independently on the characterisation measurements: discharge behaviour at different C-rates, EIS and NFRA. Such parametric ageing study is beneficial and could serve as a fundamental basis for a better understanding in the later ageing analysis in a real cell as the characterisation measurements are usually tedious and complicated, whereby the measured spectrum features a combination of multiple ageing mechanisms simultaneously.

In this section, different ageing mechanisms commonly known in LiB are individually studied via the parameterised battery model. These ageing mechanisms include SEI growth, loss of active material as well as loss in electrical conductivity. This model-based study aims to investigate the change in the battery behaviour due to the variations in the parameter which are related to the different ageing scenarios (state estimation model). Thus, this is not a study to monitor the ageing course of the battery from one-time stamp to the other (degradation model).

### 6.1.1 SEI ageing

SEI ageing is the most common ageing mechanism in LiBs, either due to the increase in SEI thickness, i.e., a longer transport path for lithium-ion before reaching the electrode surface, or due to the increase in the fraction of SEI components with poor ionic conductivity, i.e., a larger transport loss for the transfer of lithium-ion across the SEI layer. Here, the suggested two possible SEI degradations are studied independently from each other via a model-based approach.

Figure 6.1 (a) to (c) show the SEI degradation for the case with variation in the SEI thickness. In Figure 6.1 (a), the variation in the SEI thickness impacts barely the discharge behaviour at low C-rate (0.5C and 1C) but leads to small changes in the discharge behaviour at high C-rate (2C). With larger SEI thickness, the cell discharges faster as the voltage drops faster and a smaller discharge capacity is attained. From EIS in Figure 6.1 (b), one could further observe that the whole EIS spectra shift horizontally towards a higher impedance region when the SEI thickness increases. Meanwhile, in NFRA, interesting trends could be observed. On one hand, the development of $Y_3$ relates to the EIS: $Y_3$ in the frequency range between 6 Hz and $10^2$ Hz which is correlated to the charge transfer process at the negative electrode increases with the SEI thickness. On the other hand, $Y_2$ decreases with an increase in the SEI thickness, which is opposite to the development in EIS and $Y_3$. However, when one looks at the half-cell NFR spectrum at the negative electrode in the inset in Figure 6.1 (c), $Y_2$ shows an increasing tendency when the SEI thickness increases. This is because unlike EIS and $Y_3$, which are the sum of the half-cell responses from positive and negative electrodes, $Y_2$ is the difference between positive and negative electrodes's responses. Such correlation has also been reported by Ji et al. [118]. This leads to the total $Y_2$ decrease in full-cell response while the half-cell $Y_{2,neg}$ increases and this only applies when the $Y_{2,pos}$ is greater than $Y_{2,neg}$.

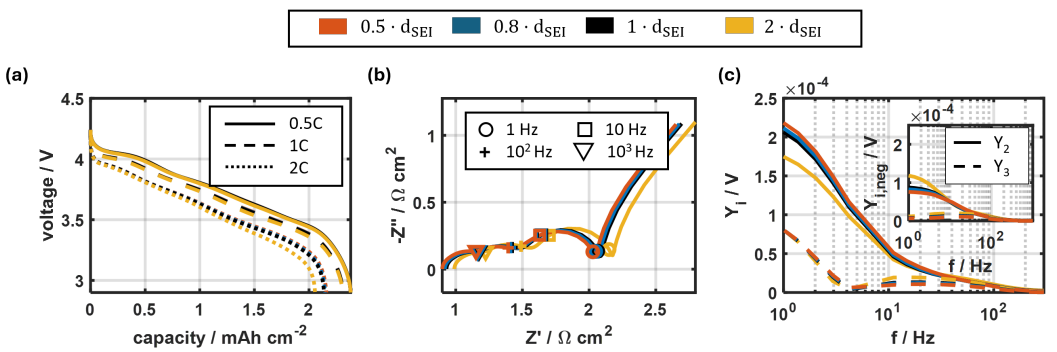


**Figure 6.1:** Impact of SEI thickness variation on (a) C-rate performance, (b) EIS and (c) NFRA at SoC 90% and 25 °C.

Conversely, for the second case, the model-based study on the SEI with different ionic conductivities does not show significant sensitivity to discharge behaviours and NFR spectra (see Figure 6.2 (a) and (c)). The only deviation is visible in the high-frequency impedance as shown in Figure 6.1 (b),

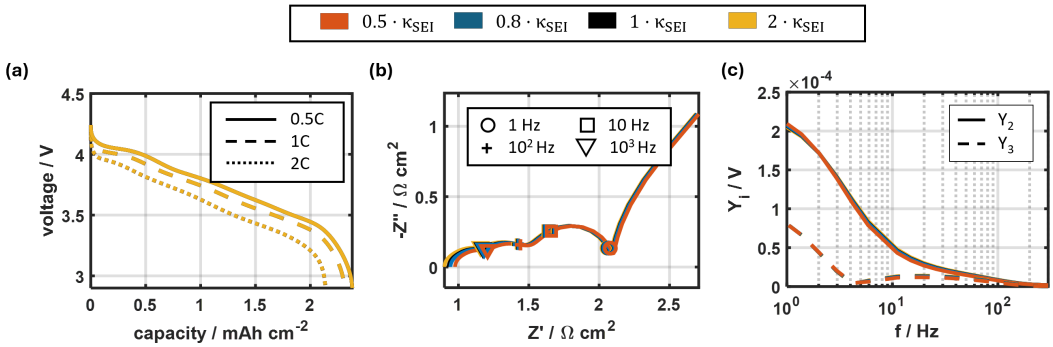


**Figure 6.2:** Impact of SEI with different ionic conductivities on (a) C-rate performance, (b) EIS and (c) NFRA at SoC 90% and 25 °C.

indicating that mainly the ohmic contribution is impacted. Here, one could observe that a smaller SEI ionic conductivity leads to a larger ohmic contribution.

The resulting difference in EIS and NFRA due to the variation in the SEI thickness and SEI with different ionic conductivity is due to the reason that a change in SEI thickness changes the lithium transport between the interfaces neg/SEI and SEI/e ($\dot{n}_{\mathrm{negSEI/SEIe}}$) as formulated in Equation 2.39. Therefore, the surface coverages at both interfaces and thus, the corresponding interfacial processes are impacted. Meanwhile, the SEI ionic conductivity only influences the potential drop in the SEI ($\Delta\Phi_{\mathrm{SEI}}$) layer as indicated in Equation 2.42. Hence, a change in SEI ionic conductivity mainly affects the ohmic contribution in the EIS and no change could be observed in NFRA.

## 6.1.2 Loss of active material

LiB ageing is also often accompanied by a loss of active material in the electrode, which could be due to the dissolution of the metal oxide at the positive electrode [30] or mechanical damage from the cycling stresses such as particle cracking that leads to the inability of the electrode to host active lithium [74]. In this work, the model-based study on active material loss is simulated by varying the volume fraction of the active material at the negative and positive electrodes separately while other parameters such as electrode conductivity and porosity remain unchanged. This means that I only consider isolated inactive particles in the case of active material loss here.

From Figure 6.3 (a) and (d), one can observe that loss of active material at both electrodes has a significant influence on the discharge behaviour, mainly the cell discharges faster, and the attained discharge capacity reduces significantly for all investigated C-rates. From the EIS in Figure 6.3 (b) and (e), it is noticeable that the impact of active material loss at the positive electrode is more significant than at the negative electrode. It can be seen that the loss of active material mainly impairs the

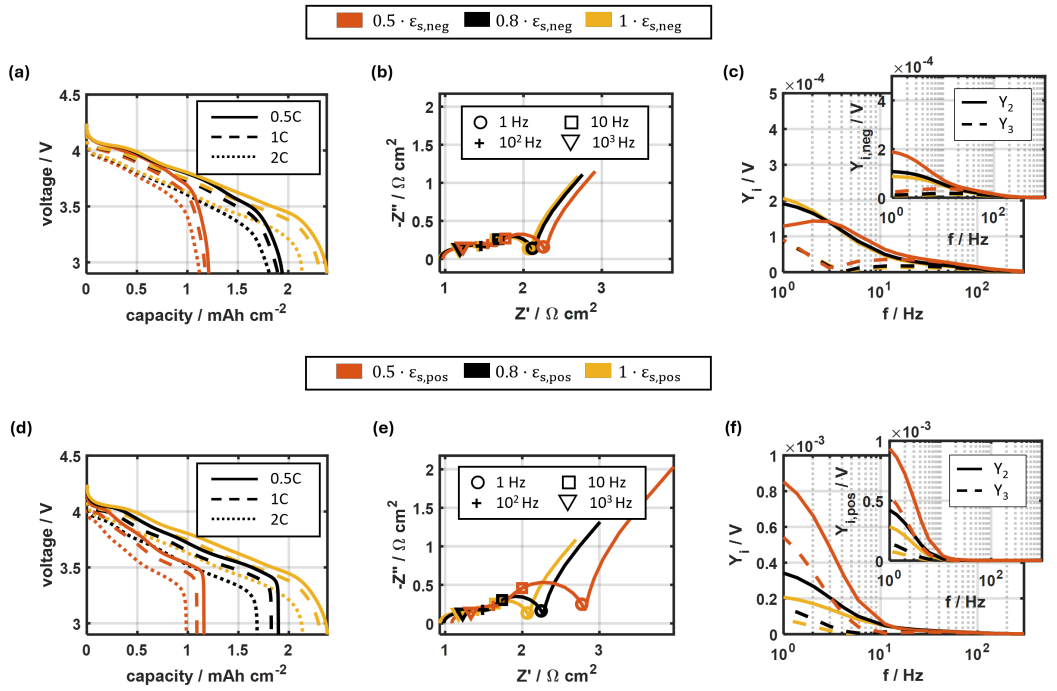


**Figure 6.3:** Impact of different active material proportion at the negative electrode (a) - (c) and at the positive electrode on (d) C-rate performance, (e) EIS and (f) NFRA at SoC 90% and 25 °C.

charge transfer process, resulting in the impedance increase at the lower frequency range. Furthermore, as the loss of active material increases, the volume fraction of the inactive components also increases. The inactive components are no longer contributing to any hosting, shuttling of lithium-ion or any electrical conduction. Therefore, one could see that ohmic resistance at high frequency $-Z'' = 0$ increases especially when it is more significant at the positive electrode. In NFRA as shown in Figure 6.3 (c) and (f), one could notice that $Y_3$ behaves similarly to EIS, which increases when the loss of active material at either negative or positive electrode also increases. Meanwhile, $Y_2$ shows a different behaviour: when the loss of active material at the negative electrode increases, $Y_2$ decreases; vice versa, $Y_2$ increases when the loss of active material at the positive electrode increases. In fact, while observing the half-cell $Y_{2,\mathrm{neg/pos}}$ responses in the insets of Figure 6.3 (c) and (f), both $Y_{2,\mathrm{neg}}$ and $Y_{2,\mathrm{pos}}$ increase with the loss of active material. However, due to the aforementioned subtraction relation between positive and negative half-cell responses, i.e. $Y_{2,\mathrm{pos}} - Y_{2,\mathrm{neg}}$, the development in full-cell $Y_2$ is different than EIS and $Y_3$. In this case, NFRA shows an interesting feature for LiB ageing analysis as one could easily identify the dominance of losses either at the negative or positive electrode by observing the development of full-cell $Y_2$ response in NFRA: kinetic losses dominate at the positive electrode when $Y_2$ increases or kinetic losses are more significant at the negative electrode when $Y_2$ decreases.

### 6.1.3 Loss of electrical conductivity

As mentioned previously, battery ageing is not only due to the loss of active material but could also be due to the degradation of additives in the electrodes such as a binder, carbon black or other conductivity additives that deteriorates the battery performance. The additive degradation then causes the active material to be dislocated from the connectivity matrix, therefore, the active material is no longer able to conduct either lithium ion or electron, losing its electrical conductivity.

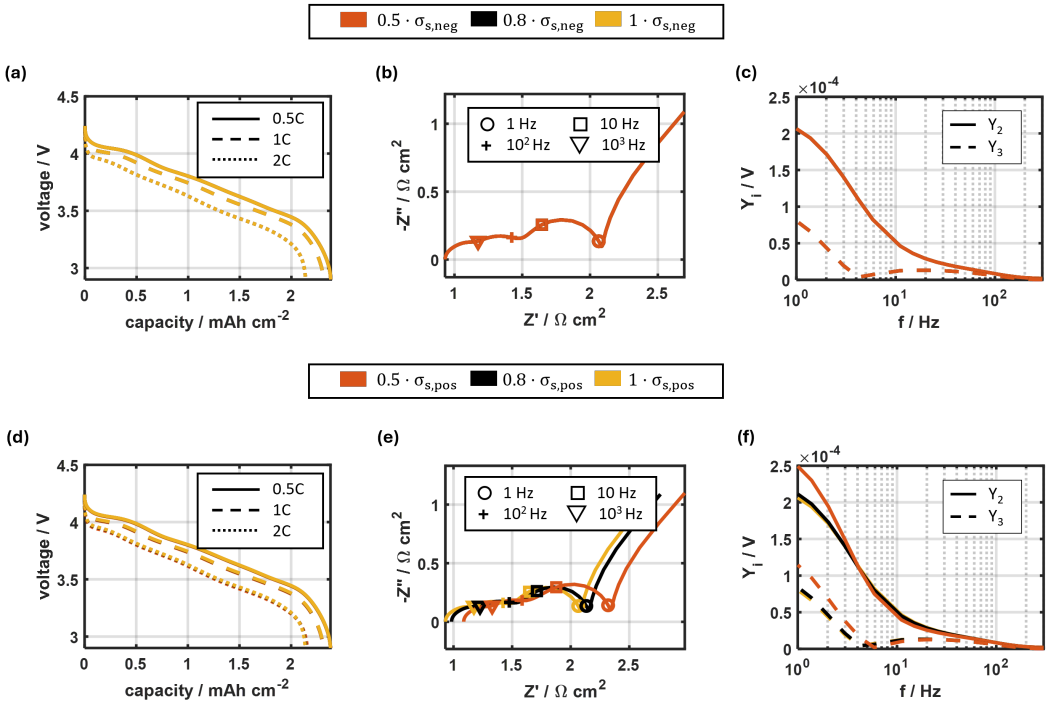


**Figure 6.4:** Impact of loss of electrical conductivity at the negative electrode (a) - (c) and the positive electrode on (d) C-rate performance, (e) EIS and (f) NFRA at SoC 90% and 25 °C.

As shown in Figure 6.4 (a) - (c), the loss of electrical conductivity at the negative electrode is insensitive and has no impact on all characterisation methods. On the contrary, the loss of electrical conductivity at the positive electrode impacts mainly EIS and NFRA but not the discharge behaviour as indicated in Figure 6.4 (d) - (f). One could notice that the loss of electrical conductivity results in a significant shift in the high-frequency impedance due to ohmic contribution and the whole EIS shifts horizontally to the right-hand side. The NFR signals at the low-frequency range that relate to the charge transfer process at the positive electrode increase correspondingly.

### 6.1.4 Comparison of different ageing scenarios

The simulative outcomes from the model-based ageing study above are summarised in Table 6.1.

**Table 6.1:** Overview of model-assisted parametric ageing study.

| | $C_{dch}$ | **Z** ($10^3$ Hz) | **Z** ($10^2$ Hz) | **Z** (6 Hz) | $Y_2$ | $Y_3$ |
|---|---|---|---|---|---|---|
| $d_{SEI}$ increases | ↓ | ↑ | ↑ | ↑ | ↓ | ↑ |
| $\kappa_{SEI}$ decreases | - | ↑ | - | - | - | - |
| $\varepsilon_{s,neg}$ decreases | ↓↓ | ↑ | - | ↑ | ↓ | ↑ |
| $\varepsilon_{s,pos}$ decreases | ↓↓ | ↑ | - | ↑↑↑ | ↑↑↑ | ↑↑↑ |
| $\sigma_{s,neg}$ decreases | - | - | - | - | - | - |
| $\sigma_{s,pos}$ decreases | - | ↑↑ | - | ↑↑ | ↑↑ | ↑↑ |

From Table 6.1, one could conclude that a decrease in discharge capacity could be due to several reasons such as an increase in SEI thickness or loss of active materials in both electrodes. For the case of the increase in SEI thickness, the decrease in discharge capacity is more obvious at higher C-rate performance.

In EIS, different transport and kinetic losses can be better separated and identified, ranging from ohmic contribution at high frequency (1 kHz), adsorption/desorption at the SEI interphase at middle range frequency ($10^2$ Hz) and charge transfer process at the electrode at low frequency (6 Hz). Ohmic contribution is mainly due to transport losses, arising from a thicker SEI with poor ionic conductivity, reduced active material and electrical conductivity in the electrodes. The impedance at the middle-frequency range attributed to the process kinetic at SEI interphase is mainly affected by a thicker SEI layer. Lastly, charge transfer impedance is shown to be sensitive under all ageing modes except for the reduction in the SEI ionic conductivity and the loss of electrical conductivity at the negative electrode.

The sensitivity of NFRA towards different ageing modes is similar to EIS, i.e. NFRA is sensitive to almost all ageing modes except the change in SEI ionic conductivity and electrical conductivity of the negative electrode. But with NFRA, one can clearly distinguish that ageing resulted from either negative or positive electrodes. For example, when degradation originates mainly from the negative electrode, $Y_3$ increases but $Y_2$ decreases or when degradation dominates at the positive electrode, both $Y_2$ and $Y_3$ increases.

In the upcoming section, I will transfer the knowledge that have learnt from this parameter study and compare it with the actual ageing behaviour of a real battery. To be specific, I will discuss the possible underlying ageing mechanisms of the real battery qualitatively and then quantitatively by

observing the change in the battery parameters via model parameterisation, performing at different ageing intervals.

## 6.2 Model-assisted ageing study on 18650 battery

This section presents a model-assisted analysis of the ageing behaviour of the 18650 battery (cell '○' — Institution 2 in Figure 4.1) shown in Chapter 4. For selected cycle numbers, the ageing-induced changes on the discharge curve, EIS and NFRA are interpreted.

In this study, the battery model incorporated with SEI modelling is used. This battery model was fully parameterised via an experimental cell, which was built using electrodes harvested from the 18650 battery as shown in Chapter 5. This parameterised battery model is set as a reference and will be used to parameterise for the initial state of the 18650 battery, i.e. before cycling, via the multi-step parameterisation strategy. For the different ageing states at different cycle numbers, defined parameters from the parameter set that describes the initial state of the 18650 battery will be tuned. Specifically, the selected parameters from the previous parametric ageing study will be adjusted to match the experimental results of different electrochemical characterisations. First, for the discharge curve, the volume fraction of active material in electrodes $\varepsilon_{s,pos/neg}$ and SEI thickness $d_{SEI}$ are adjusted. Followed by EIS, the SEI thickness $d_{SEI}$ is further refined together with other parameters such as SEI ionic conductivity $\kappa_{SEI}$, electrical conductivity of electrodes $\sigma_{s,pos/neg}$. Here, the rate constant of the charge transfer processes $k_0$ and the respective double layer capacitances $C^{DL}$ are also adjusted in EIS. In the last step, the charge transfer coefficient $\alpha$ is parameterised via NFRA while $k_0$ and $C^{DL}$ are further refined.

The evolution in the model parameters during ageing is then analysed. The model-based approach aims to quantify the observed ageing behaviours, which are visible in the discharge curve, EIS and NFRA, and relate them to the change in internal underlying processes or parameters. Thus, they can be monitored without destroying the cells.

Figure 6.5 (a) shows the SoH fade trajectory for the selected 18650 battery that was cycled between 3.0 V and 4.2 V (DoD 100%) at 45 °C and 4 A (≈1.33C). Meanwhile, Figure 6.5 (b) shows the discharges curves at 23 °C and 1.25 A (≈ 0.4C), (c) EIS and (d) NFR spectra under 23 °C and SOC 80% at the selected cycle numbers: begin-of-life (BOL), 500$^{th}$, 1000$^{th}$, 2000$^{th}$, and 3000$^{th}$ cycle. Selected battery parameters from the model parameterisation are displayed in Table 6.2. A complete parameter set can be found in Appendix A.4.

During ageing, the discharge capacity has been significantly reduced by almost 50 % at the 3000$^{th}$ cycle, which is relatable to the SoH fade. Furthermore, the impedance at about 60 Hz shifts horizontally towards a higher impedance due to an increased ohmic resistance. Simultaneously, the

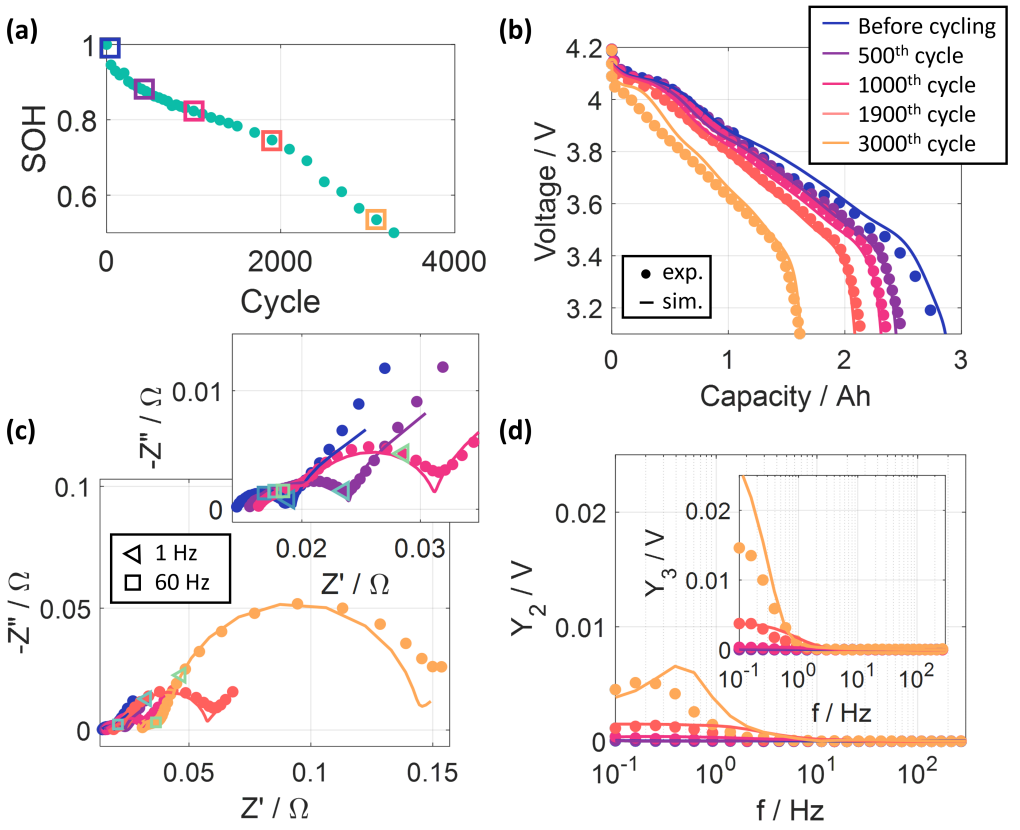


**Figure 6.5:** (a) SoH fade of the ageing of 18650 battery that was cycled between 3.0 V and 4.2 V at 4 A under 45 °C. At defined cycle number, characterisation measurements were performed: (b) discharge behaviour at 1.25C, (c) EIS and (d) NFRA ($Y_2$ and $Y_3$ in inset) at SoC 80%. All characterisation measurements are performed under 23 °C. The solid line indicates the simulated and the dashed line indicates the experimental results.

semicircle at the lower frequency of 1 Hz in EIS increases significantly, which indicates the worsening of the charge transfer process at the electrodes. In NFRA, $Y_2$ and $Y_3$ increase specifically in the lower frequency range as the SoH decreases. As advised from the previous parametric ageing study, the increase in both $Y_2$ and $Y_3$ indicates that the ageing impact of the positive electrode dominates; otherwise, $Y_2$ will decrease if the ageing impact of the negative electrode is stronger than the positive electrode.

From the model-assisted analysis in Table 6.2, it is shown that the loss of active material $\varepsilon_s$ is increasing at both electrodes. At the 3000$^{\text{th}}$ cycle, about $55-60\%$ of active material is lost as the battery ages. The loss of active material in both electrodes results in the observed decrease in discharge capacity, an increase in ohmic resistance, and charge transfer impedance in the low-frequency semicircle of EIS as well as $Y_3$ in NFRA as shown in previous parametric ageing study. Although in the previous study, the loss of active material at the negative electrode shows a decrease in $Y_2$, $Y_2$ in this

**Table 6.2:** Model-assisted ageing analysis of 18650 battery.

| Parameters | BOL | 500$^{th}$ | 1000$^{th}$ | 2000$^{th}$ | 3000$^{th}$ |
|---|---|---|---|---|---|
| $\varepsilon_{s,pos}$ [-] | 0.67 | 0.58 | 0.53 | 0.48 | 0.37 |
| $\varepsilon_{s,neg}$ [-] | 0.57 | 0.49 | 0.47 | 0.43 | 0.34 |
| $d_{SEI}$ [nm] | 78 | 200 | 300 | 340 | 350 |
| $\kappa_{SEI}$ [S m$^{-1}$] | $2.61 \cdot 10^{-4}$ | $2.61 \cdot 10^{-4}$ | $2.61 \cdot 10^{-4}$ | $2.61 \cdot 10^{-4}$ | $2.61 \cdot 10^{-4}$ |
| $\sigma_{s,pos}$ [S m$^{-1}$] | 0.02 | 0.02 | 0.02 | 0.02 | 0.02 |
| $\sigma_{s,neg}$ [S m$^{-1}$] | 15.39 | 15.39 | 15.39 | 0.30 | 0.04 |
| $k_{0,pos}$ [m s$^{-1}$] | $4.21 \cdot 10^{-9}$ | $2.31 \cdot 10^{-9}$ | $7.36 \cdot 10^{-10}$ | $1.79 \cdot 10^{-10}$ | $4.21 \cdot 10^{-11}$ |
| $k_{0,s/SEI}$ [s$^{-1}$] | 100 | 100 | 60 | 3 | 2.5 |
| $k_{0,SEI/e}$ [s$^{-1}$] | $4 \cdot 10^{6}$ | $4 \cdot 10^{6}$ | $4 \cdot 10^{6}$ | $4 \cdot 10^{6}$ | $2 \cdot 10^{6}$ |
| $\alpha_{pos}$ [-] | 0.55 | 0.55 | 0.55 | 0.55 | 0.55 |
| $\alpha_{s/SEI}$ [-] | 0.50 | 0.50 | 0.50 | 0.50 | 0.50 |
| $\alpha_{SEI/e}$ [-] | 0.50 | 0.50 | 0.50 | 0.50 | 0.50 |

case has shown to be steadily increasing as the cell ages. This is because here other parameters such as those from the positive electrode are simultaneously varied as well. The impact of the change in other parameters especially those from the positive electrode is stronger than those from the negative electrode despite the extent of active material loss at positive and negative electrode is almost similar.

Besides, the increase in the SEI thickness $d_{SEI}$ at the negative electrode shows an accelerated growth rate in the beginning, i.e. almost double the original SEI thickness after 500 cycles, and slow down afterwards. This behaviour is similar to many reported square-root time dependence of the SEI growth on graphite electrodes [57]. At the 3000$^{th}$ cycle, the SEI thickness has increased about four times as compared to the initial state. Even though it is expected that the increase in SEI thickness would lead to a decrease in $Y_2$, here again, it is due to the simultaneous change in parameters at the positive electrode, which has a stronger impact than the negative electrode and thus, the effect due to the change in the negative electrode is no longer visible. Apart from the increase in SEI thickness, the ionic conductivity of SEI layer $\kappa_{SEI}$ remains constant throughout the battery ageing.

In addition, in the outcome of the model-assisted analysis, one could also see a loss in electrical conductivity $\sigma_s$ in electrodes that leads to the ohmic shift of the EIS spectrum. Here, the loss of electrical conductivity for the model-based assessment is omitted at the positive electrode $\sigma_{s,pos}$. This assumption is made based on observation from the post-mortem analysis that the negative electrode has significantly delaminated from the copper current collector during battery opening, on the contrary, the positive electrode is still well-intact. One possible reason that the loss of electrical conductivity at

the negative electrode is more significant than positive electrode could be due to the significant volume expansion especially silicon, which expands approximately 300 % larger than graphite, leading to particle detachment, fracture, delamination or other mechanical degradations [188, 189].

Furthermore, it is also shown that the rate constants of the charge transfer processes $k_0$ at both electrodes show significant decrease, which lead to the increase in charge transfer impedance and NFR signals at the low-frequency range. Whereas the charge transfer coefficients do not change during cell ageing according to the model-assisted analysis. Although charge transfer coefficients remain the same and one might question the necessity of including NFRA characterisation into the model-assisted ageing analysis, in the following I will show that NFRA is still crucial in uniquely estimating the change in battery kinetic during cell ageing, particularly without the half-cell measurements.

Here, I consider the ageing state at the $3000^{\text{th}}$ cycle. The outcome of the model-assisted ageing analysis at the selected ageing state is plotted in Figure 6.6 indicated by the green curve (parameter set 1) and this time the half-cell simulations are plotted in Figure 6.6 (c) and (d). By comparing the full and half-cell EIS simulations, one could notice that the semicircle in the full-cell EIS simulation is mainly dominated by the contribution from the positive electrode, and the contribution from the negative electrode is almost ten times smaller than the positive electrode. Next, to test the uniqueness of this parameter set, I attempt to identify another parameter set that could also give a promising match to the experimental discharge curve and full-cell EIS, where the contribution of the negative electrode is stronger than the positive electrode. In this case, the rate constant of the charge transfer process at the positive electrode is doubled and the rate constant of the charge transfer process at the negative electrode is readjusted while other parameters remain unchanged. It is shown that when the rate constant at the positive electrode is doubled, the rate constant for the charge transfer process at the negative electrode has to be reduced five times from $2.5\,\text{s}^{-1}$ to $0.5\,\text{s}^{-1}$. The corresponding simulation result based on the second identified parameter set is plotted in Figure 6.6 indicated with the blue curve. First, one could notice that the discharge curves based on parameter sets 1 and 2 are the same while a slight deviation in full-cell EIS between the two parameter sets is noticeable, but both still give a sufficiently good match with the experiment. Meanwhile, in the half-cell EIS simulation, one could see a significant difference between parameter sets 1 and 2: parameter set 1 delivers half-cell EIS simulations that show a larger contribution at the positive electrode than the negative electrode, and the half-cell EIS simulations based on parameter set 2 give equivalently large contributions at the positive and negative electrodes. Hence, it is shown that the full-cell discharge curve and EIS alone are not unique to characterise the battery state subjected to a specific ageing interval when the half-cell information is not available. Different contributions of positive and negative electrodes will still end up in almost similar development in full-cell EIS as shown here.

In such a case, NFRA helps to better characterise the battery state without the presence of half-cell information. Figure 6.7 (a) and (b) show the simulated full-cell $Y_2$ and $Y_3$ based on parameter sets 1 (green) and 2 (blue) in comparison with the experimental outcome. Unlike parameter set 1, the simulation outcome based on parameter set 2 shows an extremely strong nonlinear response

| | $\mathbf{k_{0,pos}}$ / m $\mathbf{s^{-1}}$ | $\mathbf{k_{0,neg/SEI}}$ / $\mathbf{s^{-1}}$ |
|---|---|---|
| **Parameter set 1** | $4.21 \cdot 10^{-11}$ | 2.5 |
| **Parameter set 2** | $8 \cdot 10^{-11}$ | 0.5 |

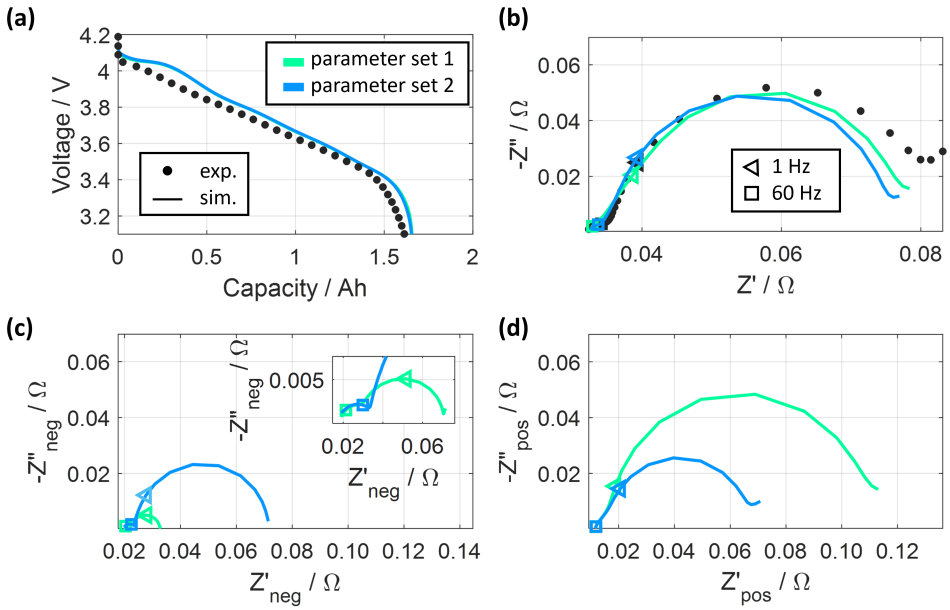


**Figure 6.6:** The comparison of simulation outcome based on parameter set 1 (green) and 2 (blue) with experimental curve in terms of (a) discharge curve at 1.25C, (b) full cell and respective half-cell EIS at (c) negative electrode and (d) positive electrode at SoC 80 % under 25 °C.

and does not agree with the experiment. From the half-cell NFR signals shown in Figure 6.7 (c) - (d), it is clear that strong nonlinear signals arise from the negative electrode. This indicates that the negative electrode has a stronger nonlinear response than the positive electrode although both of them show the same linear response. Therefore, it is shown that even though the different contributions of positive and negative electrodes could deliver almost similar development in full-cell EIS, the resulting full-cell NFRA is different, which again proves the importance of NFRA in model-assisted ageing analysis for a more unique characterisation of the battery.

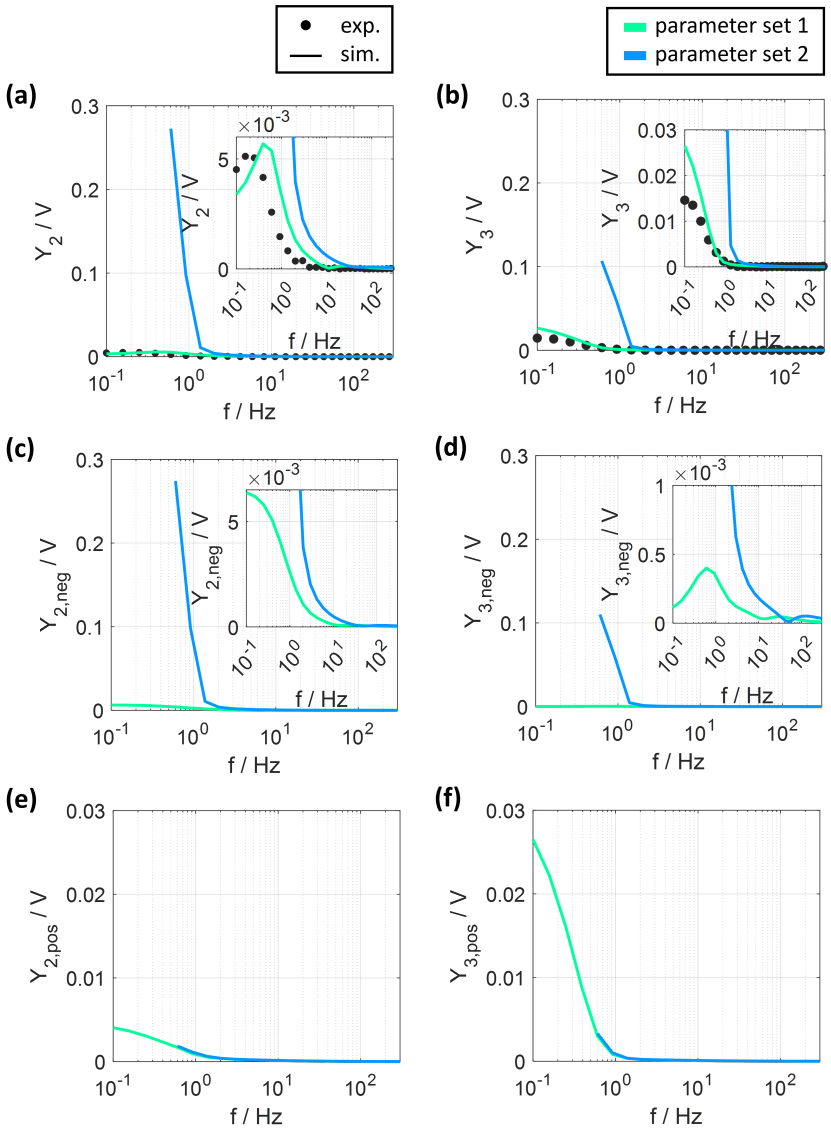


**Figure 6.7:** The comparison of simulated NFR signals based on parameter set 1 (green) and 2 (blue) with experimental outcome shown in full cell (a) $Y_2$ together with the corresponding half-cell simulation at (c) negative electrode and (e) positive electrode as well as (b) $Y_3$ with its half-cell signal in (d) - (f) at SoC 80 % under 25 °C. The simulated NFR signals based on parameter set 2 terminate at 0.6 Hz. Below 0.6 Hz the signal oscillation is stark distorted and not reliable for interpretation.

## 6.3 Conclusion

The model-assisted ageing analysis enables the quantification of the battery state and of the underlying processes within the battery. Such information is not easily assessed by a purely experimental approach.

Firstly, a parametric ageing analysis was performed. Here, different ageing scenarios were simulated by varying a specific set of related parameters, and the impact on different characterisation methods was investigated. It is then shown that the discharge behaviour at different C-rates has the lowest sensitivity as compared to EIS and NFRA as it mainly shows sensitivity towards the ageing occurrence due to the loss of active material in the electrodes. On the contrary, EIS shows a higher sensitivity. By probing the impedance responses at different frequencies, EIS shows a stronger sensitivity towards a wider range of ageing scenarios that correspond to different time constants. For example, loss of electrical conductivity in the electrode and loss of SEI ionic conductivity lead to higher ohmic resistance, an increase in SEI thickness results in larger impedance in the middle-frequency range that is related to the ad-/desorption process at the SEI, and loss of active material impacts impedance at a lower frequency range that is related to the charge transfer process at the electrode interphase. As compared to EIS, a different sensitivity of $Y_2$ in NFRA could be observed. $Y_2$ can help in identifying which electrode shows a stronger ageing impact, without using the half-cell information: $Y_2$ increases when the ageing impact at the positive electrode is stronger or otherwise, decreases when the negative electrode shows a stronger ageing impact.

Next, the knowledge learnt from the parametric ageing analysis is used to study the real ageing behaviour of an 18650 battery. It is shown that accompanied by the loss of active materials at both negative and positive electrodes, the SEI increases in thickness, which shows a square-root time dependency as reported commonly in many studies. In addition, loss of electrical conductivity (here assumed at the negative electrode from post-mortem observation) is also detected. Further, the kinetics of both charge transfer processes at the positive and negative electrodes have significantly decreased during ageing. Importantly, I have shown that full-cell information, i.e. discharge curve and EIS alone, are not sufficient to uniquely characterise the defined battery state. In specific, I have found two parameter sets that can give simulation outcomes that have a good match with the experimental full-cell discharge curve and EIS, but the half-cell EIS is different. This difference in the half-cell EIS is further amplified in the NFR signals due to the difference in the degree of nonlinearities exhibited by the positive and negative electrodes. This proves that NFRA is superior to other characterisation methods without the necessity of half-cell information.

Overall, in this chapter, it is shown that NFRA is a powerful diagnostic tool, which helps to uniquely interpret the ageing behaviour of LiBs even if the half-cell information is not available. Besides, the model-assisted ageing analysis provides one possible interpretation of the causes that underly behind the ageing of the 18650 battery. In reality, there could be other interpretations for the ageing of the 18650 battery. For example, the SEI ionic conductivity might not stay constant throughout the battery

ageing as estimated from this model-assisted ageing analysis. This is because as known in many publications the constituents and the distribution of the bilayer structure of SEI would change at different ageing intervals. In addition, in the model-assisted analysis, the loss of electrical conductivity of the electrode is attributed mainly to the negative electrode due to the observation from the post-mortem analysis. From there, one can observe a significant delamination of the active material at the negative electrode from the current collector, which makes the validation measurement such as a four-point probe difficult to perform. Lastly, it could also be seen that the rate constants of the charge transfer process at the electrode have been significantly reduced possibly due to the presence of other parasitic reactions that are not included in the simulation model such as lithium plating. As an outlook, it is therefore interesting to extend the physical battery model, incorporating different degradation modes not only SEI but also lithium plating and particle cracking. Based on this model, a model-assisted ageing analysis that includes discharge curves at different C-rates, EIS and NFRA can be performed which could hopefully provide a clearer understanding and more unique identification of the root causes of the battery ageing.

# 7 Conclusion and Outlook

The unavoidable ageing is the major problem in LiBs. Efforts to minimise the ageing impact with a longer and safer user application, prediction of premature death, estimation of residual useful life, etc. have been the main research issues in the past years. All these efforts require a deeper understanding of the ageing behaviour in LiBs. Dynamic measurements such as frequency response methods have shown to be beneficial in this topic as ageing can be distinguished and quantified in terms of different correlated processes in the battery. In particular, NFRA is shown to be a good complement to EIS as it can reveal additional information that has been masked under the conventional linear EIS. Hence, NFRA could be a practical tool for the ageing study, which is the focus of this thesis.

In this thesis, the feasibility of NFRA on LiBs ageing is assessed from different perspectives, which are underlined in four research questions:

- *How does NFRA respond to the LiBs ageing as compared to other characterisation methods?*
  In Chapter 3, for the showcase of different particle size distributions at the negative electrode, it is shown that NFRA offers more information than EIS. First, NFRA can better differentiate the underlying processes in the battery according to their nonlinearities. Also, via NFRA, one could have noticed that the positive electrode shows a stronger charge transfer asymmetry or larger $Y_2$ whereas the negative electrode shows a stronger charge transfer kinetics or larger $Y_3$. During ageing, $Y_2$ shows a different ageing trend than $Y_3$, which is believed could be related to the change in the charge transfer symmetry.

- *Is NFRA able to quantify the ageing?*
  In Chapter 4, it is shown that the NFRA-based model delivers a promising SoH prediction accuracy with a mean RMS error of less than 2 % SoH unit. As compared to the conventional capacity measurement, the measurement time for the remaining capacity estimation via NFRA can be significantly reduced. Nevertheless, the predictive performance relies on a sufficient quantity of training data, gathered under a relevant ageing regime, which means a large batch of data is required to account for the batteries under different operating conditions.

- *What kind of additional nonlinear information could be extracted via model-assisted study?*
  In Chapter 5, via the proposed multi-step parameterisation using experimental C-rate performance, EIS and NFR data, a unique parameter set can be obtained. It is shown that parameterisation that only considers C-rate performance and EIS is not unique as multiple parameter sets with different combinations of rate constant and charge transfer coefficient could give a good

match to the experimental C-rate performance and EIS. By extending the multi-step parameterisation to NFRA, the charge transfer coefficient is further parameterized and showed that it is no longer equal to 0.50 as assumed in many simulation works.

- *How can the combination of EIS and NFRA help in studying the ageing phenomenon of LiBs via modelling?*
  In Chapter 6, a model-assisted ageing analysis is performed and shows that NFRA has different sensitivities to different ageing phenomena. In particular, for the investigated cell in this thesis, the second harmonic $Y_2$ decreases when the ageing effect dominates at the negative electrode or increases when at the positive electrode. Furthermore, NFRA is shown to be superior in uniquely characterising the battery state at different ageing intervals when the half-cell information is not available. This is very beneficial especially for analysing the commercial cell, where no reference electrode is present.

In general, NFRA has shown to be a good complementary analysis tool to conventional EIS. The model-assisted analysis with NFRA could be useful assistance for studying and understanding the evolution of the internal states during battery ageing. However, there are still several issues that have to be addressed.

- Firstly, NFRA can be extended to include the investigation in the phase shift of harmonics as up to date, NFRA only focuses on the amplitude of the harmonic signals.
- Secondly, the analytical derivation of the harmonics via a model-based approach is worthy of study for several reasons:
  1. to have a clear overview of the constitution of harmonics,
  2. to eliminate artefacts due to Fast Fourier Transformation such as windowing and signal leakage problems,
  3. to avoid transient state analysis, i.e., one does not need to contemplate at which oscillation is valid for steady-state analysis.
- Thirdly, the model-assisted study can include an additional degradation mode — lithium plating to investigate its impact on harmonics.
- It is also of great interest not only to look at the full cell investigation but also electrode-resolved analysis for a clearer separation of the contributions from the positive and negative electrodes. However, it is expected that in-operando electrode-resolved analysis is challenging in the commercial battery at the current state but it is still possible in the foreseeable advancement in future diagnostic technology.

To date, the demonstration of NFRA in LiBs has shown to be feasible and promising. It is also interesting to apply NFRA not only in a single cell but also in a battery module or stack, which is more

practical in real-world applications. Of course, the measurement technique by this means needs to be scaled up as well, which might be challenging but realisable. Lastly, the application of NFRA in other battery chemistries (solid-state batteries, sodium-ion batteries) or electrochemical systems (supercapacitors, electrolyzers) is intriguing. Based on the current evidence in LiBs, a better comprehension of electrochemical systems other than LiBs is of interest to today's research community.

# Bibliography


[1] F. M. for Economic Affairs and C. Action. (2020) European energy policy. [Online]. Available: https://www.bmwk.de/Redaktion/EN/Artikel/Energy/european-energy-policy.html

[2] E. Commission. (2024) Renewable energy targets. [Online]. Available: https://energy.ec.europa.eu/topics/renewable-energy/renewable-energy-directive-targets-and-rules/renewable-energy-targets_en

[3] F. M. for Economic Affairs and C. Action. (2024) European framework - making energy efficiency a european objective. [Online]. Available: https://www.bmwk.de/Redaktion/EN/Dossier/energy-efficiency.html

[4] A. Breiter, E. Horetsky, M. Linder, and R. Rettig. (2022) Power spike: How battery makers can respond to surging demand from EVs. [Online]. Available: https://www.mckinsey.com/capabilities/operations/our-insights/power-spike-how-battery-makers-can-respond-to-surging-demand-from-evs

[5] M. V. Reddy, A. Mauger, C. M. Julien, A. Paolella, and K. Zaghib, "Brief History of Early Lithium-Battery Development," *Materials*, vol. 13, no. 8, 2020. [Online]. Available: https://www.mdpi.com/1996-1944/13/8/1884

[6] J. Asenbauer, T. Eisenmann, M. Kuenzel, A. Kazzazi, Z. Chen, and D. Bresser, "The success story of graphite as a lithium-ion anode material – fundamentals, remaining challenges, and recent developments including silicon (oxide) composites," *Sustainable Energy Fuels*, vol. 4, pp. 5387–5416, 2020. [Online]. Available: http://dx.doi.org/10.1039/D0SE00175A

[7] P. Nzereogu, A. Omah, F. Ezema, E. Iwuoha, and A. Nwanya, "Anode materials for lithium-ion batteries: A review," *Applied Surface Science Advances*, vol. 9, p. 100233, 2022. [Online]. Available: https://www.sciencedirect.com/science/article/pii/S2666523922000253

[8] F. F. C. Bazito and R. M. Torresi, "Cathodes for lithium ion batteries: the benefits of using nanostructured materials," *Journal of the Brazilian Chemical Society*, vol. 17, no. 4, p. 627–642, Aug 2006. [Online]. Available: https://doi.org/10.1590/S0103-50532006000400002

[9] M. Strafela, "Entwicklung von Kathoden für Lithium-Ionen-Dünnschichtbatterien im System Lithium-Nickel-Mangan-Kobalt-Sauerstoff, hergestellt mittels HF-Magnetronzerstäubung," Ph.D. dissertation, Karlsruher Institut für Technologie (KIT), 2019, 37.01.04; LK 01.

[10] C. M. Julien, A. Mauger, K. Zaghib, and H. Groult, "Comparative Issues of Cathode Materials for Li-Ion Batteries," *Inorganics*, vol. 2, no. 1, pp. 132–154, 2014. [Online]. Available: https://www.mdpi.com/2304-6740/2/1/132

[11] Q. Li, J. Chen, L. Fan, X. Kong, and Y. Lu, "Progress in electrolytes for rechargeable Li-based batteries and beyond," *Green Energy & Environment*, vol. 1, no. 1, pp. 18–42, 2016. [Online]. Available: https://www.sciencedirect.com/science/article/pii/S2468025716300218

[12] J. Zhang, D.-W. Wang, W. Lv, L. Qin, S. Niu, S. Zhang, T. Cao, F. Kang, and Q.-H. Yang, "Ethers Illume Sodium-Based Battery Chemistry: Uniqueness, Surprise, and Challenges," *Advanced Energy Materials*, vol. 8, no. 26, p. 1801361, 2018. [Online]. Available: https://onlinelibrary.wiley.com/doi/abs/10.1002/aenm.201801361

[13] M. Nie, J. Demeaux, B. T. Young, D. R. Heskett, Y. Chen, A. Bose, J. C. Woicik, and B. L. Lucht, "Effect of Vinylene Carbonate and Fluoroethylene Carbonate on SEI formation on Graphitic Anodes in Li-Ion Batteries," *Journal of The Electrochemical Society*, vol. 162, no. 13, p. A7008, jul 2015. [Online]. Available: https://dx.doi.org/10.1149/2.0021513jes

[14] H. Yuan, J. Luan, Z. Yang, J. Zhang, Y. Wu, Z. Lu, and H. Liu, "Single Lithium-Ion Conducting Solid Polymer Electrolyte with Superior Electrochemical Stability and Interfacial Compatibility for Solid-State Lithium Metal Batteries," *ACS Applied Materials & Interfaces*, vol. 12, no. 6, pp. 7249–7256, 2020, pMID: 31916745. [Online]. Available: https://doi.org/10.1021/acsami.9b20436

[15] L. Wang, J. Li, G. Lu, W. Li, Q. Tao, C. Shi, H. Jin, G. Chen, and S. Wang, "Fundamentals of Electrolytes for Solid-State Batteries: Challenges and Perspectives," *Frontiers in Materials*, vol. 7, 2020. [Online]. Available: https://www.frontiersin.org/articles/10.3389/fmats.2020.00111

[16] P. Peljo and H. H. Girault, "Electrochemical potential window of battery electrolytes: the HOMO–LUMO misconception," *Energy Environ. Sci.*, vol. 11, pp. 2306–2309, 2018. [Online]. Available: http://dx.doi.org/10.1039/C8EE01286E

[17] J. Vetter, P. Novák, M. Wagner, C. Veit, K.-C. Möller, J. Besenhard, M. Winter, M. Wohlfahrt-Mehrens, C. Vogler, and A. Hammouche, "Ageing mechanisms in lithium-ion batteries," *Journal of Power Sources*, vol. 147, no. 1, pp. 269–281, 2005. [Online]. Available: https://www.sciencedirect.com/science/article/pii/S0378775305000832

[18] S. J. An, J. Li, C. Daniel, D. Mohanty, S. Nagpure, and D. L. Wood, "The state of understanding of the lithium-ion-battery graphite solid electrolyte interphase (SEI) and its

relationship to formation cycling," *Carbon*, vol. 105, pp. 52–76, 2016. [Online]. Available: https://www.sciencedirect.com/science/article/pii/S0008622316302676

[19] E. Peled and S. Menkin, "Review—SEI: Past, Present and Future," *Journal of The Electrochemical Society*, vol. 164, no. 7, p. A1703, jun 2017. [Online]. Available: https://dx.doi.org/10.1149/2.1441707jes

[20] P. B. Balbuena and Y. Wang, *Lithium-Ion Batteries*. published by Imperial College Press and distributed by World Scientific Publishing Co., 2004. [Online]. Available: https://www.worldscientific.com/doi/abs/10.1142/p291

[21] F. A. Soto, Y. Ma, J. M. Martinez de la Hoz, J. M. Seminario, and P. B. Balbuena, "Formation and Growth Mechanisms of Solid-Electrolyte Interphase Layers in Rechargeable Batteries," *Chemistry of Materials*, vol. 27, no. 23, pp. 7990–8000, 2015. [Online]. Available: https://doi.org/10.1021/acs.chemmater.5b03358

[22] H. Ge, T. Aoki, N. Ikeda, S. Suga, T. Isobe, Z. Li, Y. Tabuchi, and J. Zhang, "Investigating Lithium Plating in Lithium-Ion Batteries at Low Temperatures Using Electrochemical Model with NMR Assisted Parameterization," *Journal of The Electrochemical Society*, vol. 164, no. 6, p. A1050, mar 2017. [Online]. Available: https://dx.doi.org/10.1149/2.0461706jes

[23] H. Adenusi, G. A. Chass, S. Passerini, K. V. Tian, and G. Chen, "Lithium Batteries and the Solid Electrolyte Interphase (SEI)—Progress and Outlook," *Advanced Energy Materials*, vol. 13, no. 10, p. 2203307, 2023. [Online]. Available: https://onlinelibrary.wiley.com/doi/abs/10.1002/aenm.202203307

[24] W. Huang, Y. Ye, H. Chen, R. A. Vilá, A. Xiang, H. Wang, F. Liu, Z. Yu, J. Xu, Z. Zhang, R. Xu, Y. Wu, L.-Y. Chou, H. Wang, J. Xu, D. T. Boyle, Y. Li, and Y. Cui, "Onboard early detection and mitigation of lithium plating in fast-charging batteries," *Nature Communications*, vol. 13, no. 1, p. 7091, Nov 2022. [Online]. Available: https://doi.org/10.1038/s41467-022-33486-4

[25] A. S. Mussa, A. Liivat, F. Marzano, M. Klett, B. Philippe, C. Tengstedt, G. Lindbergh, K. Edström, R. W. Lindström, and P. Svens, "Fast-charging effects on ageing for energy-optimized automotive $LiNi_{1/3}Mn_{1/3}Co_{1/3}O_2$/graphite prismatic lithium-ion cells," *Journal of Power Sources*, vol. 422, pp. 175–184, 2019. [Online]. Available: https://www.sciencedirect.com/science/article/pii/S0378775319302265

[26] L. Bläubaum, F. Röder, C. Nowak, H. S. Chan, A. Kwade, and U. Krewer, "Impact of Particle Size Distribution on Performance of Lithium-Ion Batteries," *ChemElectroChem*, vol. 7, no. 23, pp. 4755–4766, 2020. [Online]. Available: https://chemistry-europe.onlinelibrary.wiley.com/doi/abs/10.1002/celc.202001249

[27] Sungjemmenla, V. S. K., C. B. Soni, V. Kumar, and Z. W. Seh, "Understanding the Cathode–Electrolyte Interphase in Lithium-Ion Batteries," *Energy Technology*, vol. 10, no. 9, p. 2200421, 2022. [Online]. Available: https://onlinelibrary.wiley.com/doi/abs/10.1002/ente.202200421

[28] G. Zampardi and F. La Mantia, "Solid–Electrolyte Interphase at Positive Electrodes in High-Energy Li-Ion Batteries: Current Understanding and Analytical Tools," *Batteries & Supercaps*, vol. 3, no. 8, pp. 672–697, 2020. [Online]. Available: https://chemistry-europe.onlinelibrary.wiley.com/doi/abs/10.1002/batt.201900177

[29] T. J. Lee, H.-S. Kim, H. S. Hwang, J. Soon, J. Jung, J. H. Ryu, and S. M. Oh, "Solid Permeable Interface (SPI) on a High-Voltage Positive Electrode of Lithium-Ion Batteries," *Journal of The Electrochemical Society*, vol. 165, no. 3, p. A575, feb 2018. [Online]. Available: https://dx.doi.org/10.1149/2.0821803jes

[30] T. Li, X.-Z. Yuan, L. Zhang, D. Song, K. Shi, and C. Bock, "Degradation Mechanisms and Mitigation Strategies of Nickel-Rich NMC-Based Lithium-Ion Batteries," *Electrochemical Energy Reviews*, vol. 3, no. 1, pp. 43–80, Mar 2020. [Online]. Available: https://doi.org/10.1007/s41918-019-00053-3

[31] H. Shin, J. Park, A. M. Sastry, and W. Lu, "Degradation of the solid electrolyte interphase induced by the deposition of manganese ions," *Journal of Power Sources*, vol. 284, pp. 416–427, 2015. [Online]. Available: https://www.sciencedirect.com/science/article/pii/S0378775315004553

[32] J. Li, G. Liang, W. Zheng, S. Zhang, K. Davey, W. K. Pang, and Z. Guo, "Addressing cation mixing in layered structured cathodes for lithium-ion batteries: A critical review," *Nano Materials Science*, 2022. [Online]. Available: https://www.sciencedirect.com/science/article/pii/S2589965122000496

[33] S. Hwang, S. M. Kim, S.-M. Bak, K. Y. Chung, and W. Chang, "Investigating the Reversibility of Structural Modifications of $Li_xNi_yMn_zCo_{1-y-z}O_2$ Cathode Materials during Initial Charge/Discharge, at Multiple Length Scales," *Chemistry of Materials*, vol. 27, no. 17, pp. 6044–6052, 2015. [Online]. Available: https://doi.org/10.1021/acs.chemmater.5b02457

[34] P. Teichert, G. G. Eshetu, H. Jahnke, and E. Figgemeier, "Degradation and Aging Routes of Ni-Rich Cathode Based Li-Ion Batteries," *Batteries*, vol. 6, no. 1, 2020. [Online]. Available: https://www.mdpi.com/2313-0105/6/1/8

[35] A. Pfrang, A. Kersys, A. Kriston, D. Sauer, C. Rahe, S. Käbitz, and E. Figgemeier, "Long-term cycling induced jelly roll deformation in commercial 18650 cells," *Journal of Power Sources*, vol. 392, pp. 168–175, 2018. [Online]. Available: https://www.sciencedirect.com/science/article/pii/S0378775318303100

[36] X. Fleury, M. Noh, S. Geniès, P. Thivel, C. Lefrou, and Y. Bultel, "Fast-charging of Lithium Iron Phosphate battery with ohmic-drop compensation method: Ageing study," *Journal of Energy Storage*, vol. 16, pp. 21–36, 2018. [Online]. Available: https://www.sciencedirect.com/science/article/pii/S2352152X17303304

[37] A. Gabryelczyk, S. Ivanov, A. Bund, and G. Lota, "Corrosion of aluminium current collector in lithium-ion batteries: A review," *Journal of Energy Storage*, vol. 43, p. 103226, 2021. [Online]. Available: https://www.sciencedirect.com/science/article/pii/S2352152X21009233

[38] J. W. Braithwaite, A. Gonzales, G. Nagasubramanian, S. J. Lucero, D. E. Peebles, J. A. Ohlhausen, and W. R. Cieslak, "Corrosion of Lithium-Ion Battery Current Collectors," *Journal of The Electrochemical Society*, vol. 146, no. 2, p. 448, feb 1999. [Online]. Available: https://dx.doi.org/10.1149/1.1391627

[39] D. E. Demirocak and B. Bhushan, "Probing the aging effects on nanomechanical properties of a $LiFePO_4$ cathode in a large format prismatic cell," *Journal of Power Sources*, vol. 280, pp. 256–262, 2015. [Online]. Available: https://www.sciencedirect.com/science/article/pii/S0378775315001305

[40] M.-C. Pang, K. Yang, R. Brugge, T. Zhang, X. Liu, F. Pan, S. Yang, A. Aguadero, B. Wu, M. Marinescu, H. Wang, and G. J. Offer, "Interactions are important: Linking multi-physics mechanisms to the performance and degradation of solid-state batteries," *Materials Today*, vol. 49, pp. 145–183, 2021. [Online]. Available: https://www.sciencedirect.com/science/article/pii/S1369702121000572

[41] Y. Wu, L. Xie, H. Ming, Y. Guo, J.-Y. Hwang, W. Wang, X. He, L. Wang, H. N. Alshareef, Y.-K. Sun, and J. Ming, "An Empirical Model for the Design of Batteries with High Energy Density," *ACS Energy Letters*, vol. 5, no. 3, pp. 807–816, 2020. [Online]. Available: https://doi.org/10.1021/acsenergylett.0c00211

[42] D. Chen, J. Meng, H. Huang, J. Wu, P. Liu, J. Lu, and T. Liu, "An Empirical-Data Hybrid Driven Approach for Remaining Useful Life prediction of lithium-ion batteries considering capacity diving," *Energy*, vol. 245, p. 123222, 2022. [Online]. Available: https://www.sciencedirect.com/science/article/pii/S0360544222001256

[43] L. Lam and P. Bauer, "Practical Capacity Fading Model for Li-Ion Battery Cells in Electric Vehicles," *IEEE Transactions on Power Electronics*, vol. 28, no. 12, pp. 5910–5918, 2013. [Online]. Available: https://doi.org/10.1109/TPEL.2012.2235083

[44] N. Yang, Y. Fu, H. Yue, J. Zheng, X. Zhang, C. Yang, and J. Wang, "An improved semi-empirical model for thermal analysis of lithium-ion batteries," *Electrochimica Acta*, vol. 311, pp. 8–20, 2019. [Online]. Available: https://www.sciencedirect.com/science/article/pii/S0013468619308175

[45] T. Wang, K. Tseng, and J. Zhao, "Development of efficient air-cooling strategies for lithium-ion battery module based on empirical heat source model," *Applied Thermal Engineering*, vol. 90, pp. 521–529, 2015. [Online]. Available: https://www.sciencedirect.com/science/article/pii/S1359431115007176

[46] B. Yann Liaw, G. Nagasubramanian, R. G. Jungst, and D. H. Doughty, "Modeling of lithium ion cells—a simple equivalent-circuit model approach," *Solid State Ionics*, vol. 175, no. 1, pp. 835–839, 2004, fourteenth International Conference on Solid State Ionics. [Online]. Available: https://www.sciencedirect.com/science/article/pii/S0167273804006678

[47] H. He, R. Xiong, and J. Fan, "Evaluation of Lithium-Ion Battery Equivalent Circuit Models for State of Charge Estimation by an Experimental Approach," *Energies*, vol. 4, no. 4, pp. 582–598, 2011. [Online]. Available: https://www.mdpi.com/1996-1073/4/4/582

[48] T. Feng, L. Yang, X. Zhao, H. Zhang, and J. Qiang, "Online identification of lithium-ion battery parameters based on an improved equivalent-circuit model and its implementation on battery state-of-power prediction," *Journal of Power Sources*, vol. 281, pp. 192–203, 2015. [Online]. Available: https://www.sciencedirect.com/science/article/pii/S0378775315001706

[49] M.-K. Tran, M. Mathew, S. Janhunen, S. Panchal, K. Raahemifar, R. Fraser, and M. Fowler, "A comprehensive equivalent circuit model for lithium-ion batteries, incorporating the effects of state of health, state of charge, and temperature on model parameters," *Journal of Energy Storage*, vol. 43, p. 103252, 2021. [Online]. Available: https://www.sciencedirect.com/science/article/pii/S2352152X2100949X

[50] M. Doyle, T. F. Fuller, and J. Newman, "Modeling of Galvanostatic Charge and Discharge of the Lithium/Polymer/Insertion Cell," *Journal of The Electrochemical Society*, vol. 140, no. 6, p. 1526, jun 1993. [Online]. Available: https://dx.doi.org/10.1149/1.2221597

[51] J. Newman, K. E. Thomas, H. Hafezi, and D. R. Wheeler, "Modeling of lithium-ion batteries," *Journal of Power Sources*, vol. 119-121, pp. 838–843, 2003, selected papers presented at the 11th International Meeting on Lithium Batteries. [Online]. Available: https://www.sciencedirect.com/science/article/pii/S0378775303002829

[52] R. Bermejo, "Numerical analysis of a finite element formulation of the P2D model for Lithium-ion cells," *Numerische Mathematik*, vol. 149, no. 3, pp. 463–505, Nov 2021. [Online]. Available: https://doi.org/10.1007/s00211-021-01235-2

[53] J. P. Baboo, M. A. Yatoo, M. Dent, E. Hojaji Najafabadi, C. Lekakou, R. Slade, S. J. Hinder, and J. F. Watts, "Exploring Different Binders for a $LiFePO_4$ Battery, Battery Testing, Modeling and Simulations," *Energies*, vol. 15, no. 7, 2022. [Online]. Available: https://www.mdpi.com/1996-1073/15/7/2332

[54] N. Legrand, S. Raël, B. Knosp, M. Hinaje, P. Desprez, and F. Lapicque, "Including double-layer capacitance in lithium-ion battery mathematical models," *Journal of Power Sources*, vol. 251, pp. 370–378, 2014. [Online]. Available: https://www.sciencedirect.com/science/article/pii/S0378775313018715

[55] A. Wang, S. Kadam, H. Li, S. Shi, and Y. Qi, "Review on modeling of the anode solid electrolyte interphase (SEI) for lithium-ion batteries," *npj Computational Materials*, vol. 4, no. 1, p. 15, Mar 2018. [Online]. Available: https://doi.org/10.1038/s41524-018-0064-0

[56] M. T. Lawder, P. W. C. Northrop, and V. R. Subramanian, "Model-Based SEI Layer Growth and Capacity Fade Analysis for EV and PHEV Batteries and Drive Cycles," *Journal of The Electrochemical Society*, vol. 161, no. 14, p. A2099, oct 2014. [Online]. Available: https://dx.doi.org/10.1149/2.1161412jes

[57] M. B. Pinson and M. Z. Bazant, "Theory of SEI Formation in Rechargeable Batteries: Capacity Fade, Accelerated Aging and Lifetime Prediction," *Journal of The Electrochemical Society*, vol. 160, no. 2, p. A243, dec 2012. [Online]. Available: https://dx.doi.org/10.1149/2.044302jes

[58] P. Ramadass, B. Haran, P. M. Gomadam, R. White, and B. N. Popov, "Development of First Principles Capacity Fade Model for Li-Ion Cells," *Journal of The Electrochemical Society*, vol. 151, no. 2, p. A196, jan 2004. [Online]. Available: https://dx.doi.org/10.1149/1.1634273

[59] M. Safari, M. Morcrette, A. Teyssot, and C. Delacourt, "Multimodal Physics-Based Aging Model for Life Prediction of Li-Ion Batteries," *Journal of The Electrochemical Society*, vol. 156, no. 3, p. A145, dec 2008. [Online]. Available: https://dx.doi.org/10.1149/1.3043429

[60] F. M. Kindermann, J. Keil, A. Frank, and A. Jossen, "A SEI Modeling Approach Distinguishing between Capacity and Power Fade," *Journal of The Electrochemical Society*, vol. 164, no. 12, p. E287, aug 2017. [Online]. Available: https://dx.doi.org/10.1149/2.0321712jes

[61] L. von Kolzenberg, A. Latz, and B. Horstmann, "Solid–Electrolyte Interphase During Battery Cycling: Theory of Growth Regimes," *ChemSusChem*, vol. 13, no. 15, pp. 3901–3910, 2020. [Online]. Available: https://chemistry-europe.onlinelibrary.wiley.com/doi/abs/10.1002/cssc.202000867

[62] F. Single, B. Horstmann, and A. Latz, "Revealing SEI Morphology: In-Depth Analysis of a Modeling Approach," *Journal of The Electrochemical Society*, vol. 164, no. 11, p. E3132, may 2017. [Online]. Available: https://dx.doi.org/10.1149/2.0121711jes

[63] F. Single, B. Horstmann, and A. Latz, "Theory of Impedance Spectroscopy for Lithium Batteries," *The Journal of Physical Chemistry C*, vol. 123, no. 45, pp. 27 327–27 343, 2019. [Online]. Available: https://doi.org/10.1021/acs.jpcc.9b07389

[64] M. Heinrich, N. Wolff, N. Harting, V. Laue, F. Röder, S. Seitz, and U. Krewer, "Physico-Chemical Modeling of a Lithium-Ion Battery: An Ageing Study with Electrochemical Impedance Spectroscopy," *Batteries & Supercaps*, vol. 2, no. 6, pp. 530–540, 2019. [Online]. Available: https://chemistry-europe.onlinelibrary.wiley.com/doi/abs/10.1002/batt.201900011

[65] D. Witt, F. Röder, and U. Krewer, "Analysis of Lithium-Ion Battery State and Degradation via Physicochemical Cell and SEI Modeling," *Batteries & Supercaps*, vol. 5, no. 7, p. e202200067, 2022. [Online]. Available: https://chemistry-europe.onlinelibrary.wiley.com/doi/abs/10.1002/batt.202200067

[66] N. Legrand, B. Knosp, P. Desprez, F. Lapicque, and S. Raël, "Physical characterization of the charging process of a Li-ion battery and prediction of li plating by electrochemical modelling," *Journal of Power Sources*, vol. 245, pp. 208–216, 2014. [Online]. Available: https://www.sciencedirect.com/science/article/pii/S0378775313011373

[67] C. von Lüders, J. Keil, M. Webersberger, and A. Jossen, "Modeling of lithium plating and lithium stripping in lithium-ion batteries," *Journal of Power Sources*, vol. 414, pp. 41–47, 2019. [Online]. Available: https://www.sciencedirect.com/science/article/pii/S0378775318314484

[68] S. Carelli and W. G. Bessler, "Prediction of Reversible Lithium Plating with a Pseudo-3D Lithium-Ion Battery Model," *Journal of The Electrochemical Society*, vol. 167, no. 10, p. 100515, jun 2020. [Online]. Available: https://dx.doi.org/10.1149/1945-7111/ab95c8

[69] D. R. Baker and M. W. Verbrugge, "Modeling Overcharge at Graphite Electrodes: Plating and Dissolution of Lithium," *Journal of The Electrochemical Society*, vol. 167, no. 1, p. 013504, sep 2019. [Online]. Available: https://dx.doi.org/10.1149/2.0042001JES

[70] S. Hein, T. Danner, and A. Latz, "An Electrochemical Model of Lithium Plating and Stripping in Lithium Ion Batteries," *ACS Applied Energy Materials*, vol. 3, no. 9, pp. 8519–8531, 2020. [Online]. Available: https://doi.org/10.1021/acsaem.0c01155

[71] P. Arora, M. Doyle, and R. E. White, "Mathematical Modeling of the Lithium Deposition Overcharge Reaction in Lithium-Ion Batteries Using Carbon-Based Negative Electrodes," *Journal of The Electrochemical Society*, vol. 146, no. 10, p. 3543, oct 1999. [Online]. Available: https://dx.doi.org/10.1149/1.1392512

[72] X.-G. Yang, Y. Leng, G. Zhang, S. Ge, and C.-Y. Wang, "Modeling of lithium plating induced aging of lithium-ion batteries: Transition from linear to nonlinear aging," *Journal of Power Sources*, vol. 360, pp. 28–40, 2017. [Online]. Available: https://www.sciencedirect.com/science/article/pii/S0378775317307619

[73] J. Keil and A. Jossen, "Electrochemical Modeling of Linear and Nonlinear Aging of Lithium-Ion Cells," *Journal of The Electrochemical Society*, vol. 167, no. 11, p. 110535, jul 2020. [Online]. Available: https://dx.doi.org/10.1149/1945-7111/aba44f

[74] S. E. J. O'Kane, W. Ai, G. Madabattula, D. Alonso-Alvarez, R. Timms, V. Sulzer, J. S. Edge, B. Wu, G. J. Offer, and M. Marinescu, "Lithium-ion battery degradation: how to model it," *Phys. Chem. Chem. Phys.*, vol. 24, pp. 7909–7922, 2022. [Online]. Available: http://dx.doi.org/10.1039/D2CP00417H

[75] J. Landesfeind and H. A. Gasteiger, "Temperature and Concentration Dependence of the Ionic Transport Properties of Lithium-Ion Battery Electrolytes," *Journal of The Electrochemical Society*, vol. 166, no. 14, p. A3079, sep 2019. [Online]. Available: https://dx.doi.org/10.1149/2.0571912jes

[76] A. M. Colclasure and R. J. Kee, "Thermodynamically consistent modeling of elementary electrochemistry in lithium-ion batteries," *Electrochimica Acta*, vol. 55, no. 28, pp. 8960–8973, 2010. [Online]. Available: https://www.sciencedirect.com/science/article/pii/S0013468610010789

[77] M. Gaberšček, "Understanding li-based battery materials via electrochemical impedance spectroscopy," *Nature Communications*, vol. 12, no. 1, 2021. [Online]. Available: http://dx.doi.org/10.1038/s41467-021-26894-5

[78] D. D. Macdonald, "Reflections on the history of electrochemical impedance spectroscopy," *Electrochimica Acta*, vol. 51, no. 8, pp. 1376–1388, 2006, electrochemical Impedance Spectroscopy. [Online]. Available: https://www.sciencedirect.com/science/article/pii/S0013468605007991

[79] A. Lasia, *Electrochemical Impedance Spectroscopy and its Applications*. Boston, MA: Springer US, 2002, pp. 143–248. [Online]. Available: https://doi.org/10.1007/0-306-46916-2_2

[80] F. Ciucci, "Modeling electrochemical impedance spectroscopy," *Current Opinion in Electrochemistry*, vol. 13, pp. 132–139, 2019, fundamental and Theoretical Electrochemistry · Physical and Nanoelectrochemistry. [Online]. Available: https://www.sciencedirect.com/science/article/pii/S2451910318301881

[81] D. D. Macdonald, "Review of mechanistic analysis by electrochemical impedance spectroscopy," *Electrochimica Acta*, vol. 35, no. 10, pp. 1509–1525, 1990. [Online]. Available: https://www.sciencedirect.com/science/article/pii/0013468690800059

[82] A. Amirudin and D. Thieny, "Application of electrochemical impedance spectroscopy to study the degradation of polymer-coated metals," *Progress in Organic Coatings*, vol. 26,

no. 1, pp. 1–28, 1995. [Online]. Available: https://www.sciencedirect.com/science/article/pii/0300944095005811

[83] H. Xiao and F. Mansfeld, "Evaluation of Coating Degradation with Electrochemical Impedance Spectroscopy and Electrochemical Noise Analysis," *Journal of The Electrochemical Society*, vol. 141, no. 9, p. 2332, sep 1994. [Online]. Available: https://dx.doi.org/10.1149/1.2055121

[84] S. Feliu, "Electrochemical Impedance Spectroscopy for the Measurement of the Corrosion Rate of Magnesium Alloys: Brief Review and Challenges," *Metals*, vol. 10, no. 6, 2020. [Online]. Available: https://www.mdpi.com/2075-4701/10/6/775

[85] K. Jüttner, "Electrochemical impedance spectroscopy (EIS) of corrosion processes on inhomogeneous surfaces," *Electrochimica Acta*, vol. 35, no. 10, pp. 1501–1508, 1990. [Online]. Available: https://www.sciencedirect.com/science/article/pii/0013468690800048

[86] J. F. Rubinson and Y. P. Kayinamura, "Charge transport in conducting polymers: insights from impedance spectroscopy," *Chem. Soc. Rev.*, vol. 38, pp. 3339–3347, 2009. [Online]. Available: http://dx.doi.org/10.1039/B904083H

[87] M. Ates, "Review study of electrochemical impedance spectroscopy and equivalent electrical circuits of conducting polymers on carbon surfaces," *Progress in Organic Coatings*, vol. 71, no. 1, pp. 1–10, 2011. [Online]. Available: https://www.sciencedirect.com/science/article/pii/S0300944010003607

[88] W. Gomes and D. Vanmaekelbergh, "Impedance spectroscopy at semiconductor electrodes: Review and recent developments," *Electrochimica Acta*, vol. 41, no. 7, pp. 967–973, 1996, electrochemical Impendance Spectroscopy. [Online]. Available: https://www.sciencedirect.com/science/article/pii/0013468695004270

[89] B.-Y. Chang and S.-M. Park, "Electrochemical Impedance Spectroscopy," *Annual Review of Analytical Chemistry*, vol. 3, no. 1, pp. 207–229, 2010, pMID: 20636040. [Online]. Available: https://doi.org/10.1146/annurev.anchem.012809.102211

[90] P. Iurilli, C. Brivio, and V. Wood, "On the use of electrochemical impedance spectroscopy to characterize and model the aging phenomena of lithium-ion batteries: a critical review," *Journal of Power Sources*, vol. 505, p. 229860, 2021. [Online]. Available: https://www.sciencedirect.com/science/article/pii/S0378775321003992

[91] D. Kashyap, P. K. Dwivedi, J. K. Pandey, Y. H. Kim, G. M. Kim, A. Sharma, and S. Goel, "Application of electrochemical impedance spectroscopy in bio-fuel cell characterization: A review," *International Journal of Hydrogen Energy*, vol. 39, no. 35, pp. 20 159–20 170, 2014. [Online]. Available: https://www.sciencedirect.com/science/article/pii/S0360319914028067

[92] S. M. Rezaei Niya and M. Hoorfar, "Study of proton exchange membrane fuel cells using electrochemical impedance spectroscopy technique – a review," *Journal of Power Sources*, vol. 240, pp. 281–293, 2013. [Online]. Available: https://www.sciencedirect.com/science/article/pii/S0378775313006022

[93] T. H. Wan, M. Saccoccio, C. Chen, and F. Ciucci, "Influence of the Discretization Methods on the Distribution of Relaxation Times Deconvolution: Implementing Radial Basis Functions with DRTtools," *Electrochimica Acta*, vol. 184, pp. 483–499, 2015. [Online]. Available: https://www.sciencedirect.com/science/article/pii/S0013468615305090

[94] A. L. Gavrilyuk, D. A. Osinkin, and D. I. Bronin, "The use of Tikhonov regularization method for calculating the distribution function of relaxation times in impedance spectroscopy," *Russian Journal of Electrochemistry*, vol. 53, no. 6, pp. 575–588, Jun 2017. [Online]. Available: https://doi.org/10.1134/S1023193517060040

[95] F. Ciucci and C. Chen, "Analysis of Electrochemical Impedance Spectroscopy Data Using the Distribution of Relaxation Times: A Bayesian and Hierarchical Bayesian Approach," *Electrochimica Acta*, vol. 167, pp. 439–454, 2015. [Online]. Available: https://www.sciencedirect.com/science/article/pii/S0013468615007203

[96] E. Ivers-Tiffée and A. Weber, "Evaluation of electrochemical impedance spectra by the distribution of relaxation times," *Journal of the Ceramic Society of Japan*, vol. 125, no. 4, pp. 193–201, 2017.

[97] N. Schlüter, S. Ernst, and U. Schröder, "Finding the Optimal Regularization Parameter in Distribution of Relaxation Times Analysis," *ChemElectroChem*, vol. 6, no. 24, pp. 6027–6037, 2019. [Online]. Available: https://chemistry-europe.onlinelibrary.wiley.com/doi/abs/10.1002/celc.201901863

[98] M. Saccoccio, T. H. Wan, C. Chen, and F. Ciucci, "Optimal Regularization in Distribution of Relaxation Times applied to Electrochemical Impedance Spectroscopy: Ridge and Lasso Regression Methods - A Theoretical and Experimental Study," *Electrochimica Acta*, vol. 147, pp. 470–482, 2014. [Online]. Available: https://www.sciencedirect.com/science/article/pii/S0013468614018763

[99] T. Vidaković-Koch, T. Miličić, L. A. Živković, H. S. Chan, U. Krewer, and M. Petkovska, "Nonlinear frequency response analysis: a recent review and perspectives," *Current Opinion in Electrochemistry*, vol. 30, p. 100851, 2021. [Online]. Available: https://www.sciencedirect.com/science/article/pii/S2451910321001654

[100] A. Battistel and F. La Mantia, "Nonlinear analysis: The intermodulated differential immittance spectroscopy," *Analytical Chemistry*, vol. 85, no. 14, pp. 6799–6805, 2013, pMID: 23745974. [Online]. Available: https://doi.org/10.1021/ac400907q

[101] B. Bensmann, M. Petkovska, T. Vidaković-Koch, R. Hanke-Rauschenbach, and K. Sundmacher, "Nonlinear Frequency Response of Electrochemical Methanol Oxidation Kinetics: A Theoretical Analysis," *Journal of The Electrochemical Society*, vol. 157, no. 9, p. B1279, jul 2010. [Online]. Available: https://dx.doi.org/10.1149/1.3446836

[102] T. R. Vidaković-Koch, V. V. Panić, M. Andrić, M. Petkovska, and K. Sundmacher, "Nonlinear Frequency Response Analysis of the Ferrocyanide Oxidation Kinetics. Part I. A Theoretical Analysis," *The Journal of Physical Chemistry C*, vol. 115, no. 35, pp. 17 341–17 351, 2011. [Online]. Available: https://doi.org/10.1021/jp201297v

[103] V. V. Panić, T. R. Vidaković-Koch, M. Andrić, M. Petkovska, and K. Sundmacher, "Nonlinear Frequency Response Analysis of the Ferrocyanide Oxidation Kinetics. Part II. Measurement Routine and Experimental Validation," *The Journal of Physical Chemistry C*, vol. 115, no. 35, pp. 17 352–17 358, 2011. [Online]. Available: https://doi.org/10.1021/jp201300a

[104] L. A. Živković, S. Kandaswamy, M. Petkovska, and T. Vidaković-Koch, "Evaluation of Electrochemical Process Improvement Using the Computer-Aided Nonlinear Frequency Response Method: Oxygen Reduction Reaction in Alkaline Media," *Frontiers in Chemistry*, vol. 8, 2020. [Online]. Available: https://www.frontiersin.org/articles/10.3389/fchem.2020.579869

[105] T. Kadyk, R. Hanke-Rauschenbach, and K. Sundmacher, "Nonlinear frequency response analysis of PEM fuel cells for diagnosis of dehydration, flooding and CO-poisoning," *Journal of Electroanalytical Chemistry*, vol. 630, no. 1, pp. 19–27, 2009. [Online]. Available: https://www.sciencedirect.com/science/article/pii/S0022072809000473

[106] N. Harting, N. Wolff, F. Röder, and U. Krewer, "Nonlinear Frequency Response Analysis (NFRA) of Lithium-Ion Batteries," *Electrochimica Acta*, vol. 248, pp. 133–139, 2017. [Online]. Available: https://www.sciencedirect.com/science/article/pii/S0013468617307934

[107] N. Harting, N. Wolff, and U. Krewer, "Identification of Lithium Plating in Lithium-Ion Batteries using Nonlinear Frequency Response Analysis (NFRA)," *Electrochimica Acta*, vol. 281, pp. 378–385, 2018. [Online]. Available: https://www.sciencedirect.com/science/article/pii/S0013468618311848

[108] N. Harting, R. Schenkendorf, N. Wolff, and U. Krewer, "State-of-Health Identification of Lithium-Ion Batteries Based on Nonlinear Frequency Response Analysis: First Steps with Machine Learning," *Applied Sciences*, vol. 8, no. 5, 2018. [Online]. Available: https://www.mdpi.com/2076-3417/8/5/821

[109] N. Harting, N. Wolff, F. Röder, and U. Krewer, "State-of-Health Diagnosis of Lithium-Ion Batteries Using Nonlinear Frequency Response Analysis," *Journal of The Electrochemical Society*, vol. 166, no. 2, p. A277, jan 2019. [Online]. Available: https://dx.doi.org/10.1149/2.1031902jes

[110] N. Wolff, N. Harting, M. Heinrich, and U. Krewer, "Nonlinear frequency response analysis on lithium-ion batteries: Process identification and differences between transient and steady-state behavior," *Electrochimica Acta*, vol. 298, pp. 788–798, 2019. [Online]. Available: https://www.sciencedirect.com/science/article/pii/S0013468618328172

[111] N. Wolff, N. Harting, M. Heinrich, F. Röder, and U. Krewer, "Nonlinear Frequency Response Analysis on Lithium-Ion Batteries: A Model-Based Assessment," *Electrochimica Acta*, vol. 260, pp. 614–622, 2018. [Online]. Available: https://www.sciencedirect.com/science/article/pii/S0013468617326609

[112] N. Wolff, N. Harting, F. Röder, M. Heinrich, and U. Krewer, "Understanding nonlinearity in electrochemical systems," *The European Physical Journal Special Topics*, vol. 227, no. 18, pp. 2617–2640, Apr 2019. [Online]. Available: https://doi.org/10.1140/epjst/e2019-800135-2

[113] M. D. Murbach and D. T. Schwartz, "Extending Newman's Pseudo-Two-Dimensional Lithium-Ion Battery Impedance Simulation Approach to Include the Nonlinear Harmonic Response," *Journal of The Electrochemical Society*, vol. 164, no. 11, p. E3311, jun 2017. [Online]. Available: https://dx.doi.org/10.1149/2.0301711jes

[114] M. D. Murbach, V. W. Hu, and D. T. Schwartz, "Nonlinear Electrochemical Impedance Spectroscopy of Lithium-Ion Batteries: Experimental Approach, Analysis, and Initial Findings," *Journal of The Electrochemical Society*, vol. 165, no. 11, p. A2758, aug 2018. [Online]. Available: https://dx.doi.org/10.1149/2.0711811jes

[115] Q. Mao, U. Krewer, and R. Hanke-Rauschenbach, "Total harmonic distortion analysis for direct methanol fuel cell anode," *Electrochemistry Communications*, vol. 12, no. 11, pp. 1517–1519, 2010. [Online]. Available: https://www.sciencedirect.com/science/article/pii/S1388248110003681

[116] Q. Mao and U. Krewer, "Sensing methanol concentration in direct methanol fuel cell with total harmonic distortion: Theory and application," *Electrochimica Acta*, vol. 68, pp. 60–68, 2012. [Online]. Available: https://www.sciencedirect.com/science/article/pii/S0013468612002058

[117] J. Wilson, D. Schwartz, and S. Adler, "Nonlinear electrochemical impedance spectroscopy for solid oxide fuel cell cathode materials," *Electrochimica Acta*, vol. 51, no. 8, pp. 1389–1402, 2006, electrochemical Impedance Spectroscopy. [Online]. Available: https://www.sciencedirect.com/science/article/pii/S0013468605008017

[118] Y. Ji and D. T. Schwartz, "Second-harmonic nonlinear electrochemical impedance spectroscopy: Part i. analytical theory and equivalent circuit representations for planar and porous electrodes," *Journal of The Electrochemical Society*, vol. 170, no. 12, p. 123511, dec 2023. [Online]. Available: https://dx.doi.org/10.1149/1945-7111/ad15ca

[119] Y. Ji, and D. T. Schwartz, "Second-harmonic nonlinear electrochemical impedance spectroscopy: Part ii. model-based analysis of lithium-ion battery experiments," *Journal of The Electrochemical Society*, vol. 171, no. 2, p. 023504, feb 2024. [Online]. Available: https://dx.doi.org/10.1149/1945-7111/ad2596

[120] G. Instrument. (2023) EIS: Potentiostatoc or Galvanostatic Mode? [Online]. Available: https://www.gamry.com/application-notes/EIS/eis-potentiostatic-galvanostatic-mode/

[121] H. Seng Chan, L. Bläubaum, D. Vijayshankar, F. Röder, C. Nowak, A. Weber, A. Kwade, and U. Krewer, "Revealing the impact of particle size distribution on ageing of lithium-ion batteries with frequency response analysis," *Batteries & Supercaps*, vol. 6, no. 10, p. e202300203, 2023. [Online]. Available: https://chemistry-europe.onlinelibrary.wiley.com/doi/abs/10.1002/batt.202300203

[122] D. Goers, M. E. Spahr, A. Leone, W. Märkle, and P. Novák, "The influence of the local current density on the electrochemical exfoliation of graphite in lithium-ion battery negative electrodes," *Electrochimica Acta*, vol. 56, no. 11, pp. 3799–3808, 2011. [Online]. Available: https://www.sciencedirect.com/science/article/pii/S0013468611002611

[123] M. E. Spahr, D. Goers, W. Märkle, J. Dentzer, A. Würsig, H. Buqa, C. Vix-Guterl, and P. Novák, "Overpotentials and solid electrolyte interphase formation at porous graphite electrodes in mixed ethylene carbonate–propylene carbonate electrolyte systems," *Electrochimica Acta*, vol. 55, no. 28, pp. 8928–8937, 2010. [Online]. Available: https://www.sciencedirect.com/science/article/pii/S001346861001087X

[124] M. Weiss, R. Ruess, J. Kasnatscheew, Y. Levartovsky, N. R. Levy, P. Minnmann, L. Stolz, T. Waldmann, M. Wohlfahrt-Mehrens, D. Aurbach, M. Winter, Y. Ein-Eli, and J. Janek, "Fast charging of lithium-ion batteries: A review of materials aspects," *Advanced Energy Materials*, vol. 11, no. 33, p. 2101126, 2021. [Online]. Available: https://advanced.onlinelibrary.wiley.com/doi/abs/10.1002/aenm.202101126

[125] R. Xiong, Y. Yu, S. Chen, M. Li, L. Li, M. Zhou, W. Zhang, Bo yan, D. Li, H. Yang, Y. Zhang, and H. Zhou, "Overpotential decomposition enabled decoupling of complex kinetic processes in battery electrodes," *Journal of Power Sources*, vol. 553, p. 232296, 2023. [Online]. Available: https://www.sciencedirect.com/science/article/pii/S0378775322012733

[126] S.-M. Park and J.-S. Yoo, "Peer reviewed: Electrochemical impedance spectroscopy for better electrochemical measurements," *Analytical Chemistry*, vol. 75, no. 21, pp. 455 A–461 A, 2003. [Online]. Available: https://doi.org/10.1021/ac0313973

[127] C. Nowak, L. Froboese, M. Winter, T. Placke, W. Haselrieder, and A. Kwade, "Designing graphite-based positive electrodes and their properties in dual-ion batteries using particle size-adjusted active materials," *Energy Technology*, vol. 7, no. 10, p. 1900528, 2019. [Online]. Available: https://onlinelibrary.wiley.com/doi/abs/10.1002/ente.201900528

[128] M. Ender, J. Illig, and E. Ivers-Tiffée, "Three-Electrode Setups for Lithium-Ion Batteries," *Journal of The Electrochemical Society*, vol. 164, no. 2, p. A71, dec 2016. [Online]. Available: https://dx.doi.org/10.1149/2.0231702jes

[129] J. P. Schmidt, T. Chrobak, M. Ender, J. Illig, D. Klotz, and E. Ivers-Tiffée, "Studies on $LiFePO_4$ as cathode material using impedance spectroscopy," *Journal of Power Sources*, vol. 196, no. 12, pp. 5342–5348, 2011, selected papers presented at the $12^{th}$ Ulm ElectroChemical Talks (UECT):2015 Technologies on Batteries and Fuel Cells. [Online]. Available: https://www.sciencedirect.com/science/article/pii/S0378775310019786

[130] J. Illig, M. Ender, A. Weber, and E. Ivers-Tiffée, "Modeling graphite anodes with serial and transmission line models," *Journal of Power Sources*, vol. 282, pp. 335–347, 2015. [Online]. Available: https://www.sciencedirect.com/science/article/pii/S037877531500261X

[131] J. Costard, J. Joos, A. Schmidt, and E. Ivers-Tiffée, "Charge Transfer Parameters of $Ni_xMn_yCo_{1-x-y}$ Cathodes Evaluated by a Transmission Line Modeling Approach," *Energy Technology*, vol. 9, no. 6, p. 2000866, 2021. [Online]. Available: https://onlinelibrary.wiley.com/doi/abs/10.1002/ente.202000866

[132] R. A. House, G. J. Rees, M. A. Pérez-Osorio, J.-J. Marie, E. Boivin, A. W. Robertson, A. Nag, M. Garcia-Fernandez, K.-J. Zhou, and P. G. Bruce, "First-cycle voltage hysteresis in Li-rich 3d cathodes associated with molecular $O_2$ trapped in the bulk," *Nature Energy*, vol. 5, no. 10, pp. 777–785, Oct 2020. [Online]. Available: https://doi.org/10.1038/s41560-020-00697-2

[133] A. Van der Ven, K. A. See, and L. Pilon, "Hysteresis in electrochemical systems," *Battery Energy*, vol. 1, no. 2, p. 20210017, 2022. [Online]. Available: https://onlinelibrary.wiley.com/doi/abs/10.1002/bte2.20210017

[134] P. Shafiei Sabet, A. J. Warnecke, F. Meier, H. Witzenhausen, E. Martinez-Laserna, and D. U. Sauer, "Non-invasive yet separate investigation of anode/cathode degradation of lithium-ion batteries (nickel–cobalt–manganese vs. graphite) due to accelerated aging," *Journal of Power Sources*, vol. 449, p. 227369, 2020. [Online]. Available: https://www.sciencedirect.com/science/article/pii/S037877531931362X

[135] H. S. Chan, E. J. Dickinson, T. P. Heins, J. Park, M. Gaberšček, Y. Y. Lee, M. Heinrich, V. Ruiz, E. Napolitano, P. Kauranen, E. Fedorovskaya, J. Moškon, T. Kallio, S. Mousavihashemi, U. Krewer, G. Hinds, and S. Seitz, "Comparison of methodologies to estimate state-of-health of commercial li-ion cells from electrochemical frequency response data," *Journal of Power Sources*, vol. 542, p. 231814, 2022. [Online]. Available: https://www.sciencedirect.com/science/article/pii/S0378775322008035

[136] M.-F. Ge, Y. Liu, X. Jiang, and J. Liu, "A review on state of health estimations and remaining useful life prognostics of lithium-ion batteries," *Measurement*, vol. 174, p. 109057, 2021. [Online]. Available: https://www.sciencedirect.com/science/article/pii/S0263224121000890

[137] Y. Zhou, M. Huang, Y. Chen, and Y. Tao, "A novel health indicator for on-line lithium-ion batteries remaining useful life prediction," *Journal of Power Sources*, vol. 321, pp. 1–10, 2016. [Online]. Available: https://www.sciencedirect.com/science/article/pii/S037877531630492X

[138] D. Zhou, L. Xue, Y. Song, and J. Chen, "On-line remaining useful life prediction of lithium-ion batteries based on the optimized gray model gm(1,1)," *Batteries*, vol. 3, no. 3, 2017. [Online]. Available: https://www.mdpi.com/2313-0105/3/3/21

[139] W. Li, N. Sengupta, P. Dechent, D. Howey, A. Annaswamy, and D. U. Sauer, "Online capacity estimation of lithium-ion batteries with deep long short-term memory networks," *Journal of Power Sources*, vol. 482, p. 228863, 2021. [Online]. Available: https://www.sciencedirect.com/science/article/pii/S0378775320311678

[140] X. Kong, A. Bonakdarpour, B. T. Wetton, D. P. Wilkinson, and B. Gopaluni, "State of health estimation for lithium-ion batteries," *IFAC-PapersOnLine*, vol. 51, no. 18, pp. 667–671, 2018, 10th IFAC Symposium on Advanced Control of Chemical Processes ADCHEM 2018. [Online]. Available: https://www.sciencedirect.com/science/article/pii/S2405896318320329

[141] M. Huotari, S. Arora, A. Malhi, and K. Främling, "Comparing seven methods for state-of-health time series prediction for the lithium-ion battery packs of forklifts," *Applied Soft Computing*, vol. 111, p. 107670, 2021. [Online]. Available: https://www.sciencedirect.com/science/article/pii/S1568494621005913

[142] H. Feng and G. Shi, "Soh and rul prediction of li-ion batteries based on improved gaussian process regression," *Journal of Power Electronics*, vol. 21, no. 12, pp. 1845–1854, Dec 2021. [Online]. Available: https://doi.org/10.1007/s43236-021-00318-5

[143] C. Kunlong, J. Jiuchun, Z. Fangdan, S. Bingxiang, and Z. Yanru, "Soh estimation for lithium-ion batteries: A cointegration and error correction approach," in *2016 IEEE International Conference on Prognostics and Health Management (ICPHM)*, 2016, pp. 1–6.

[144] S. Shen, B. Liu, K. Zhang, and S. Ci, "Toward fast and accurate soh prediction for lithium-ion batteries," *IEEE Transactions on Energy Conversion*, vol. 36, no. 3, pp. 2036–2046, 2021.

[145] C. P. Lin, J. Cabrera, D. Y. W. Yu, F. Yang, and K. L. Tsui, "Soh estimation and soc recalibration of lithium-ion battery with incremental capacity analysis and cubic smoothing spline," *Journal of The Electrochemical Society*, vol. 167, no. 9, p. 090537, may 2020. [Online]. Available: https://doi.org/10.1149/1945-7111/ab8f56

[146] A. Naha, S. Han, S. Agarwal, A. Guha, A. Khandelwal, P. Tagade, K. S. Hariharan, S. M. Kolake, J. Yoon, and B. Oh, "An incremental voltage difference based technique for online state of health estimation of li-ion batteries," *Scientific Reports*, vol. 10, no. 1, p. 9526, Jun 2020. [Online]. Available: https://doi.org/10.1038/s41598-020-66424-9

[147] J. Zhu, Y. Wang, Y. Huang, R. Bhushan Gopaluni, Y. Cao, M. Heere, M. J. Mühlbauer, L. Mereacre, H. Dai, X. Liu, A. Senyshyn, X. Wei, M. Knapp, and H. Ehrenberg, "Data-driven capacity estimation of commercial lithium-ion batteries from voltage relaxation," *Nature Communications*, vol. 13, no. 1, p. 2261, Apr 2022. [Online]. Available: https://doi.org/10.1038/s41467-022-29837-w

[148] K. Mc Carthy, H. Gullapalli, K. M. Ryan, and T. Kennedy, "Review—use of impedance spectroscopy for the estimation of li-ion battery state of charge, state of health and internal temperature," *Journal of The Electrochemical Society*, vol. 168, no. 8, p. 080517, aug 2021. [Online]. Available: https://doi.org/10.1149/1945-7111/ac1a85

[149] Y. Zhang, Q. Tang, Y. Zhang, J. Wang, U. Stimming, and A. A. Lee, "Identifying degradation patterns of lithium ion batteries from impedance spectroscopy using machine learning," *Nature Communications*, vol. 11, no. 1, p. 1706, Apr 2020. [Online]. Available: https://doi.org/10.1038/s41467-020-15235-7

[150] X. Wang, X. Wei, H. Dai, and Q. Wu, "State estimation of lithium ion battery based on electrochemical impedance spectroscopy with on-board impedance measurement system," in *2015 IEEE Vehicle Power and Propulsion Conference (VPPC)*, 2015, pp. 1–5.

[151] A. Guha and A. Patra, "Online estimation of the electrochemical impedance spectrum and remaining useful life of lithium-ion batteries," *IEEE Transactions on Instrumentation and Measurement*, vol. 67, no. 8, pp. 1836–1849, 2018.

[152] A. Guha, and A. Patra, "State of health estimation of lithium-ion batteries using capacity fade and internal resistance growth models," *IEEE Transactions on Transportation Electrification*, vol. 4, no. 1, pp. 135–146, 2018.

[153] M. Galeotti, L. Cinà, C. Giammanco, S. Cordiner, and A. Di Carlo, "Performance analysis and soh (state of health) evaluation of lithium polymer batteries through electrochemical impedance spectroscopy," *Energy*, vol. 89, pp. 678–686, 2015. [Online]. Available: https://www.sciencedirect.com/science/article/pii/S0360544215007756

[154] Y. Li, B. Dong, T. Zerrin, E. Jauregui, X. Wang, X. Hua, D. Ravichandran, R. Shang, J. Xie, M. Ozkan, and C. S. Ozkan, "State-of-health prediction for lithium-ion batteries via electrochemical impedance spectroscopy and artificial neural networks," *Energy Storage*, vol. 2, no. 5, p. e186, 2020. [Online]. Available: https://onlinelibrary.wiley.com/doi/abs/10.1002/est2.186

[155] W. Haiying, H. Long, S. Jianhua, L. Shuanquan, and W. Feng, "Study on correlation with soh and eis model of li-ion battery," in *Proceedings of 2011 6th International Forum on Strategic Technology*, vol. 1, 2011, pp. 261–264.

[156] C. Lyu, T. Zhang, W. Luo, G. Wei, B. Ma, and L. Wang, "Soh estimation of lithium-ion batteries based on fast time domain impedance spectroscopy," in *2019 14th IEEE Conference on Industrial Electronics and Applications (ICIEA)*, 2019, pp. 2142–2147.

[157] A. Eddahech, O. Briat, N. Bertrand, J.-Y. Delétage, and J.-M. Vinassa, "Behavior and state-of-health monitoring of li-ion batteries using impedance spectroscopy and recurrent neural networks," *International Journal of Electrical Power & Energy Systems*, vol. 42, no. 1, pp. 487–494, 2012. [Online]. Available: https://www.sciencedirect.com/science/article/pii/S0142061512001779

[158] X. Wang, X. Wei, and H. Dai, "Estimation of state of health of lithium-ion batteries based on charge transfer resistance considering different temperature and state of charge," *Journal of Energy Storage*, vol. 21, pp. 618–631, 2019. [Online]. Available: https://www.sciencedirect.com/science/article/pii/S2352152X18305279

[159] W. Li, M. Rentemeister, J. Badeda, D. Jöst, D. Schulte, and D. U. Sauer, "Digital twin for battery systems: Cloud battery management system with online state-of-charge and state-of-health estimation," *Journal of Energy Storage*, vol. 30, p. 101557, 2020. [Online]. Available: https://www.sciencedirect.com/science/article/pii/S2352152X20308495

[160] P. Refaeilzadeh, L. Tang, H. Liu *et al.*, "Cross-validation," *Encyclopedia of database systems*, vol. 5, pp. 532–538, 2009.

[161] H. S. Chan, Y. Y. Lee, D. Witt, J. Ulrich, A. Weber, and U. Krewer, "Improved identifiability of kinetic parameters in lithium-ion batteries via nonlinear frequency response analysis," *Batteries & Supercaps*, vol. 8, no. 11, p. e202500179, 2025. [Online]. Available: https://chemistry-europe.onlinelibrary.wiley.com/doi/abs/10.1002/batt.202500179

[162] I. O. Santos-Mendoza, J. Vázquez-Arenas, I. González, G. Ramos-Sánchez, and C. O. Castillo-Araiza, "Revisiting electrochemical techniques to characterize the solid-state diffusion mechanism in lithium-ion batteries," *International Journal of Chemical Reactor Engineering*, vol. 17, no. 6, p. 20180095, 2019. [Online]. Available: https://doi.org/10.1515/ijcre-2018-0095

[163] K. Chayambuka, G. Mulder, D. L. Danilov, and P. H. Notten, "Determination of state-of-charge dependent diffusion coefficients and kinetic rate constants of phase changing electrode materials using physics-based models," *Journal of Power Sources Advances*, vol. 9, p. 100056, 2021. [Online]. Available: https://www.sciencedirect.com/science/article/pii/S2666248521000111

[164] M. A. Cabañero, N. Boaretto, M. Röder, J. Müller, J. Kallo, and A. Latz, "Direct determination of diffusion coefficients in commercial li-ion batteries," *Journal of The Electrochemical Society*, vol. 165, no. 5, p. A847, mar 2018. [Online]. Available: https://doi.org/10.1149/2.0301805jes

[165] M. Ecker, T. K. D. Tran, P. Dechent, S. Käbitz, A. Warnecke, and D. U. Sauer, "Parameterization of a Physico-Chemical Model of a Lithium-Ion Battery: I. Determination of Parameters," *Journal of The Electrochemical Society*, vol. 162, no. 9, p. A1836, jun 2015. [Online]. Available: https://dx.doi.org/10.1149/2.0551509jes

[166] H. Lee, S. Yang, S. Kim, J. Song, J. Park, C.-H. Doh, Y.-C. Ha, T.-S. Kwon, and Y. M. Lee, "Understanding the effects of diffusion coefficient and exchange current density on the electrochemical model of lithium-ion batteries," *Current Opinion in Electrochemistry*, vol. 34, p. 100986, 2022. [Online]. Available: https://www.sciencedirect.com/science/article/pii/S2451910322000515

[167] J. Schmalstieg, C. Rahe, M. Ecker, and D. U. Sauer, "Full Cell Parameterization of a High-Power Lithium-Ion Battery for a Physico-Chemical Model: Part I. Physical and Electrochemical Parameters," *Journal of The Electrochemical Society*, vol. 165, no. 16, p. A3799, dec 2018. [Online]. Available: https://dx.doi.org/10.1149/2.0321816jes

[168] V. Laue, F. Röder, and U. Krewer, "Practical identifiability of electrochemical P2D models for lithium-ion batteries," *Journal of Applied Electrochemistry*, vol. 51, no. 9, pp. 1253–1265, Sep 2021. [Online]. Available: https://doi.org/10.1007/s10800-021-01579-5

[169] A. M. Bizeray, J. Kim, S. R. Duncan, and D. A. Howey, "Identifiability and parameter estimation of the single particle lithium-ion battery model," *IEEE Transactions on Control Systems Technology*, vol. 27, no. 5, pp. 1862–1877, 2019.

[170] T. Pajkossy, M. U. Ceblin, and G. Mészáros, "Dynamic electrochemical impedance spectroscopy for the charge transfer rate measurement of the ferro/ferricyanide redox couple on gold," *Journal of Electroanalytical Chemistry*, vol. 899, p. 115655, 2021. [Online]. Available: https://www.sciencedirect.com/science/article/pii/S1572665721006810

[171] K. Dokko, N. Nakata, Y. Suzuki, and K. Kanamura, "High-Rate Lithium Deintercalation from Lithiated Graphite Single-Particle Electrode," *The Journal of Physical Chemistry C*, vol. 114, no. 18, pp. 8646–8650, 2010. [Online]. Available: https://doi.org/10.1021/jp101166d

[172] A. Hess, Q. Roode-Gutzmer, C. Heubner, M. Schneider, A. Michaelis, M. Bobeth, and G. Cuniberti, "Determination of state of charge-dependent asymmetric Butler–Volmer kinetics for $Li_xCoO_2$ electrode using GITT measurements," *Journal of Power Sources*, vol. 299, pp. 156–161, 2015. [Online]. Available: https://www.sciencedirect.com/science/article/pii/S0378775315301300

[173] Y. Li and Y. Qi, "Energy landscape of the charge transfer reaction at the complex li/sei/electrolyte interface," *Energy Environ. Sci.*, vol. 12, pp. 1286–1295, 2019. [Online]. Available: http://dx.doi.org/10.1039/C8EE03586E

[174] Y. Y. Lee, H. S. Chan, J. Ulrich, A. Weber, and U. Krewer, "Full-, half-, and symmetrical cell analysis of lithium-ion battery using impedance and nonlinear frequency response," *Journal of The Electrochemical Society*, vol. 171, no. 7, p. 070543, jul 2024. [Online]. Available: https://dx.doi.org/10.1149/1945-7111/ad5ef9

[175] J. Illig, M. Ender, T. Chrobak, J. P. Schmidt, D. Klotz, and E. Ivers-Tiffée, "Separation of charge transfer and contact resistance in lifepo4-cathodes by impedance modeling," *Journal of The Electrochemical Society*, vol. 159, no. 7, p. A952, jul 2012. [Online]. Available: https://dx.doi.org/10.1149/2.030207jes

[176] K. Smith and C.-Y. Wang, "Power and thermal characterization of a lithium-ion battery pack for hybrid-electric vehicles," *Journal of Power Sources*, vol. 160, no. 1, pp. 662–673, 2006. [Online]. Available: https://www.sciencedirect.com/science/article/pii/S0378775306001017

[177] K. A. Smith, C. D. Rahn, and C.-Y. Wang, "Control oriented 1d electrochemical model of lithium ion battery," *Energy Conversion and Management*, vol. 48, no. 9, pp. 2565–2578, 2007. [Online]. Available: https://www.sciencedirect.com/science/article/pii/S0196890407000908

[178] C. Heubner, M. Schneider, and A. Michaelis, "Investigation of charge transfer kinetics of Li-Intercalation in $LiFePO_4$," *Journal of Power Sources*, vol. 288, pp. 115–120, 2015. [Online]. Available: https://www.sciencedirect.com/science/article/pii/S0378775315007600

[179] T. L. Kirk, A. Lewis-Douglas, D. Howey, C. P. Please, and S. J. Chapman, "Nonlinear electrochemical impedance spectroscopy for lithium-ion battery model parameterization," *Journal of The Electrochemical Society*, vol. 170, no. 1, p. 010514, jan 2023. [Online]. Available: https://dx.doi.org/10.1149/1945-7111/acada7

[180] T. Piao, S. Park, C. Doh, and S. Moon, "Intercalation of lithium ions into graphite electrodes studied by ac impedance measurements," *Journal of The Electrochemical Society*, vol. 146, no. 8, p. 2794, aug 1999. [Online]. Available: https://dx.doi.org/10.1149/1.1392010

[181] Y. Chang, J. Jong, and G. T. Fey, "Kinetic characterization of the electrochemical intercalation of lithium ions into graphite electrodes," *Journal of The Electrochemical Society*, vol. 147, no. 6, p. 2033, jun 2000. [Online]. Available: https://dx.doi.org/10.1149/1.1393481

[182] A. Durdel, S. Friedrich, L. Hüsken, and A. Jossen, "Modeling silicon-dominant anodes: Parametrization, discussion, and validation of a newman-type model," *Batteries*, vol. 9, no. 11, 2023. [Online]. Available: https://www.mdpi.com/2313-0105/9/11/558

[183] R. Chandrasekaran and T. F. Fuller, "Analysis of the lithium-ion insertion silicon composite electrode/separator/lithium foil cell," *Journal of The Electrochemical Society*, vol. 158, no. 8, p. A859, jun 2011. [Online]. Available: https://dx.doi.org/10.1149/1.3589301

[184] S. Das, P. M. Attia, W. C. Chueh, and M. Z. Bazant, "Electrochemical kinetics of sei growth on carbon black: Part ii. modeling," *Journal of The Electrochemical Society*, vol. 166, no. 4, p. E107, feb 2019. [Online]. Available: https://dx.doi.org/10.1149/2.0241904jes

[185] L. Liu, J. Park, X. Lin, A. M. Sastry, and W. Lu, "A thermal-electrochemical model that gives spatial-dependent growth of solid electrolyte interphase in a li-ion battery," *Journal of Power Sources*, vol. 268, pp. 482–490, 2014. [Online]. Available: https://www.sciencedirect.com/science/article/pii/S0378775314009045

[186] A. A. Tahmasbi, T. Kadyk, and M. H. Eikerling, "Statistical physics-based model of solid electrolyte interphase growth in lithium ion batteries," *Journal of The Electrochemical Society*, vol. 164, no. 6, p. A1307, apr 2017. [Online]. Available: https://dx.doi.org/10.1149/2.1581706jes

[187] J. Costard, M. Ender, M. Weiss, and E. Ivers-Tiffée, "Three-electrode setups for lithium-ion batteries," *Journal of The Electrochemical Society*, vol. 164, no. 2, p. A80, dec 2016. [Online]. Available: https://dx.doi.org/10.1149/2.0241702jes

[188] V. Müller, R.-G. Scurtu, K. Richter, T. Waldmann, M. Memm, M. A. Danzer, and M. Wohlfahrt-Mehrens, "Effects of Mechanical Compression on the Aging and the Expansion Behavior of Si/C-Composite|NMC811 in Different Lithium-Ion Battery Cell Formats," *Journal of The Electrochemical Society*, vol. 166, no. 15, p. A3796, nov 2019. [Online]. Available: https://dx.doi.org/10.1149/2.1121915jes

[189] F. Tariq, V. Yufit, D. S. Eastwood, Y. Merla, M. Biton, B. Wu, Z. Chen, K. Freedman, G. Offer, E. Peled, P. D. Lee, D. Golodnitsky, and N. Brandon, "In-Operando X-ray Tomography Study of Lithiation Induced Delamination of Si Based Anodes for Lithium-Ion Batteries," *ECS Electrochemistry Letters*, vol. 3, no. 7, p. A76, jan 2014. [Online]. Available: https://dx.doi.org/10.1149/2.0081407eel

[190] E. Lai, "4 - Frequency-domain representation of discrete-time signals," in *Practical Digital Signal Processing*, E. Lai, Ed. Oxford: Newnes, 2003, pp. 61–78. [Online]. Available: https://www.sciencedirect.com/science/article/pii/B9780750657983500047

# List of Figures

# List of Tables

# List of Abbreviations and Symbols

**Symbols**

| | | |
|---|---|---|
| $\Delta G^0$ | Gibb's free enthalpy | $\mathrm{J\,mol^{-1}}$ |
| $\dot{n}$ | Species flux | $\mathrm{mol\,m^{-3}\,s^{-1}}$ |
| $\hat{i}$ | Perturbation current amplitude | A |
| $A_{cell}$ | Length of cell | m |
| $A_m$ | Redlich kister coefficient | m |
| $a_s$ | Volumetric surface area | $\mathrm{m^2\,m^{-3}}$ |
| a | Activity | - |
| $C^{DL}$ | Double layer capacitance | $\mathrm{F\,m^{-2}}$ |
| $C_{theo}$ | Theoretical capacity | $\mathrm{Ah\,m^{-3}}$ |
| c | Species concentration | $\mathrm{mol\,m^{-3}}$ |
| D | Diffusion coefficient | $\mathrm{m^2\,s^{-1}}$ |
| d | Thickness of electrode | m |
| $E_a$ | Activation energy | $\mathrm{J\,mol^{-1}}$ |
| $E_{eq}$ | Equilibrium potential | V |
| F | Faraday's constant | $\mathrm{C\,mol^{-1}}$ |
| f | Frequency | Hz |
| $G(\omega)$ | Frequency response function | - |
| $g(\tau)$ | Distribution function | - |
| I | Current | A |
| $j_0$ | Exchange current density | $\mathrm{A\,m^{-3}}$ |
| j | Volumetric current density | $\mathrm{A\,m^{-3}}$ |
| $k_0$ | Rate constant | $\mathrm{s^{-1}, mol\,s^{-1}}$ |
| $L_{cell}$ | Length of cell | m |
| $R_s$ | Particle radius | m |
| R | Gas constant | $\mathrm{J\,mol^{-1}\,K^{-1}}$ |

| | | |
|---|---|---|
| r | Reaction species flux | $\mathrm{mol\,m^{-3}\,s^{-1}}$ |
| $S_v$ | Volumetric specific surface area | $\mathrm{m^2\,m^{-3}}$ |
| $t_p$ | Transference number | - |
| T | Temperature | K |
| t | Time | s |
| u | Uncertainty | - |
| V | Voltage | V |
| $x_{50}$ | Median particle size | m |
| X | Mole fraction | - |
| Y | Harmonics in voltage output signal | V |
| $Z''$ | Imaginary part of impedance | Ω |
| $Z'$ | Real part of impedance | Ω |

**Greek symbols**

| | | |
|---|---|---|
| $\alpha$ | Charge transfer coefficient | - |
| $\beta$ | Bruggemann exponent | - |
| $\delta$ | Thickness | m |
| $\eta$ | Overpotential | V |
| $\gamma(\tau)$ | Distribution function | - |
| $\Gamma$ | Surface site density | $\mathrm{mol\,m^{-2}}$ |
| $\kappa$ | Ionic conductivity | $\mathrm{S\,m^{-1}}$ |
| $\lambda$ | DRT regularization parameter | - |
| $\Omega$ | Parameter space | - |
| $\omega$ | Angular frequency | Hz |
| $\Phi$ | Potential | V |
| $\phi$ | Mass flux | $\mathrm{mol\,m^{-3}}$ |
| $\rho_s$ | Spearman rank coefficient | - |
| $\sigma$ | Electrical conductivity | $\mathrm{S\,m^{-1}}$ |
| $\tau$ | Tortuosity | - |
| $\theta$ | Surface coverage | - |
| $\varepsilon$ | Porosity | - |

**Indices**

| | |
|---|---|
| $1, 2, 3, \ldots$ | Harmonic orders |
| $c, ML$ | Coating mass loading |
| DL | Double layer |
| eff | Effective value |
| e | Electrolyte phase |
| Li | Lithium ion |
| max | Maximum value |
| neg/SEI | Interphase between negative electrode and SEI |
| neg | Negative electrode |
| pos | Positive electrode |
| ref | Reference value |
| rel | Relative value |
| SEI/e | Interphase between SEI and electrolyte |
| s | Solid phase |

**Abbreviations**

| | |
|---|---|
| BMS | Battery Management System |
| CC | Constant Current |
| CEI | Cathode-Electrolyte Interphase |
| CV | Constant Voltage |
| DFT | Density Functional Theory |
| DMC | Dimethyl Carbonate |
| DoD | Depth-of-Discharge |
| DRT | Distribution of Relaxation Times |
| EC | Ethylene Carbonate |
| ECM | Equivalent Circuit Model |
| EIS | Electrochemical Impedance Spectroscopy |
| FFT | Fast Fourier Transformation |
| FIB-SEM | Focused Ion Beam and Scanning Electron Microscope |
| GITT | Galvanostatic Intermittent Titration Technique |
| LAM | Loss of Active Material |

| | |
|---|---|
| LCT | Life-Cycle Test |
| LiB | Lithium-ion Battery |
| $LiPF_6$ | Lithium Hexafluorophosphate |
| LLI | Loss of Lithium Inventory |
| MCMB | Mesocarbon Microbeads powder |
| NFRA | Nonlinear Frequency Response Analysis |
| NLEIS | Nonlinear Electrochemical Impedance Spectroscopy |
| NMC | Lithium Nickel Manganese Cobalt Oxides |
| NMP | N-Methyl-2-Pyrrolidone |
| P2D | Pseudo-Two-Dimensional model |
| PE | Polyethylene |
| PP | Polypropylene |
| RC | Resistor-Capacitor |
| RMSE | Root Mean Square Error |
| SEI | Solid-Electrolyte Interphase |
| SEM-EDX | Scanning Electron Microscope and Energy Dispersive X-ray analysis |
| Si | Silicon |
| SoC | State-of-Charge |
| SoH | State-of-Health |
| SP | Single Particle model |
| SPI | Solid Permeable Interphase |
| THD | Total Harmonic Distortion |

# A Appendix

## A.1 Mathematical description on EIS

To better understand the working principle of EIS, the mathematical derivation is illustrated with the help of an electrochemical system that takes periodic current $\mathrm{I}(\mathrm{t})$ as input with $\hat{\mathrm{i}}$ as perturbation amplitude and computes the temporal evolution of voltage $\mathrm{V}(\mathrm{t})$. The derivation of the formula is adapted from Bensmann et al. [101].

$$\mathrm{V}(\mathrm{t}) = \int_{-\infty}^{\infty} \mathrm{g}(\tau) \cdot \mathrm{I}(\mathrm{t}-\tau)\,\mathrm{d}\tau \tag{A.1}$$

$$\mathrm{I}(\mathrm{t}) = \frac{\hat{\mathrm{i}}}{2} \cdot (\mathrm{e}^{\mathrm{j}\omega\mathrm{t}} + \mathrm{e}^{-\mathrm{j}\omega\mathrm{t}}) \tag{A.2}$$

By substituting Equation (A.2) in (A.1), one obtain

$$\mathrm{V}(\mathrm{t}) = \frac{\hat{\mathrm{i}}}{2} \cdot \int_{-\infty}^{\infty} \mathrm{g}(\tau) \cdot (\mathrm{e}^{\mathrm{j}\omega(\mathrm{t}-\tau)} + \mathrm{e}^{-\mathrm{j}\omega(\mathrm{t}-\tau)})\,\mathrm{d}\tau \tag{A.3}$$

$$\mathrm{V}(\mathrm{t}) = \frac{\hat{\mathrm{i}}}{2} \cdot \left[ \mathrm{e}^{\mathrm{j}\omega\mathrm{t}} \underbrace{\int_{-\infty}^{\infty} g(\tau) \cdot e^{-j\omega\tau}\, d\tau}_{\mathrm{G}(\omega)=\mathrm{Z}(\omega)} + \mathrm{e}^{-\mathrm{j}\omega\mathrm{t}} \underbrace{\int_{-\infty}^{\infty} g(\tau) \cdot e^{j\omega\tau}\, d\tau}_{\mathrm{G}(-\omega)=\mathrm{Z}(-\omega)} \right] \tag{A.4}$$

Shown in Equation (A.4), the Fourier transformed function exhibits Hermitian symmetry, i.e., $\mathrm{G}(-\omega)$ is the conjugate of $\mathrm{G}(\omega)$ [190]. Both conjugates are the mirror of each other and have the same amplitude, only differing in signs of frequency. Hereby, the the frequency response function hereby is equivalent to the impedance: $\mathrm{G}(\omega) = \mathrm{Z}(\omega)$.

## A.2 Mathematical description on NFRA

For the nonlinear analysis in this thesis, NFRA is implemented and the working principle is detailed as follows. As an example, an electrochemical system with a nonlinear correlation between current as input and voltage as output can be depicted using the Volterra series based on Bensmann at al. [101].

$$V(t) = \sum_{n=1}^{\infty} \int_{-\infty}^{\infty} \dots \int_{-\infty}^{\infty} g_n(\tau_1, \dots, \tau_n) \cdot I(t-\tau_1) \dots I(t-\tau_n)\, d\tau_1 \dots d\tau_n \tag{A.5}$$

Similarly, the system is excited periodically as shown below.

$$\begin{aligned} V(t) = \sum_{n=1}^{\infty} \left(\frac{\hat{i}}{2}\right)^n \int_{-\infty}^{\infty} \dots \int_{-\infty}^{\infty} g_n(\tau_1, \dots, \tau_n) \cdot (e^{j\omega(t-\tau_1)} + e^{-j\omega(t-\tau_1)}) \\ \dots (e^{j\omega(t-\tau_n)} + e^{-j\omega(t-\tau_n)})\, d\tau_1 \dots d\tau_n \end{aligned} \tag{A.6}$$

By applying the n-fold Fourier transformation,

$$G_n(\omega_1, \dots, \omega_n) = \int_{-\infty}^{\infty} \dots \int_{-\infty}^{\infty} g_n(\tau_1, \dots \tau_n) \cdot e^{-j\omega\tau_1} \dots e^{-j\omega\tau_n}\, d\tau_1 \dots d\tau_n \tag{A.7}$$

This delivers the following expression.

$$\begin{aligned} V(t) = {} & \frac{\hat{i}}{2} \cdot \left[ G_1(\omega) e^{j\omega t} + G_1(-\omega) e^{-j\omega t} \right] \\ & + \left(\frac{\hat{i}}{2}\right)^2 \left[ G_2(\omega, \omega) e^{2j\omega t} + 2G_2(\omega, -\omega) e^0 + G_2(-\omega, -\omega) e^{-2j\omega t} \right] \\ & + \left(\frac{\hat{i}}{2}\right)^3 [\, G_3(\omega, \omega, \omega) e^{3j\omega t} + 3G_3(\omega, \omega, -\omega) e^{j\omega t} + 3G_3(\omega, -\omega, -\omega) e^{-j\omega t} \\ & + \; G_3(-\omega, -\omega, -\omega)^{-3j\omega t} \,] + \dots \end{aligned} \tag{A.8}$$

Via harmonic probing, i.e., sorting and grouping the coefficient term with similar frequency, one could obtain the linear $Y_1$ as well as the nonlinear system responses $Y_2$, $Y_3$, etc.

$$
\begin{aligned}
V(t) = {} & e^{0}\left[\frac{\hat{i}^{2}}{2}G_2(\omega,-\omega)+\ldots\right] \\
& + \underbrace{e^{j\omega t}\left[\frac{\hat{i}}{2}G_1(\omega)+\ldots\right]+e^{-j\omega t}\left[\frac{\hat{i}}{2}G_1(-\omega)+\ldots\right]}_{y_1(t)} \\
& + \underbrace{e^{2j\omega t}\left[\frac{\hat{i}^{2}}{4}G_2(\omega,\omega)+\ldots\right]+e^{-2j\omega t}\left[\frac{\hat{i}^{2}}{4}G_2(-\omega,-\omega)+\ldots\right]}_{y_2(t)} \\
& + \underbrace{e^{3j\omega t}\left[\frac{\hat{i}^{3}}{8}G_3(\omega,\omega,\omega)+\ldots\right]+e^{-3j\omega t}\left[\frac{\hat{i}^{3}}{8}G_3(-\omega,-\omega,-\omega)+\ldots\right]}_{y_3(t)}
\end{aligned}
\tag{A.9}
$$

## A.3 Multi-step parameterisation results for the rebuilt experimental cell from LG 18650 HG2

**Table A.1:** List of parameters that are obtained from parameterisation (marked with a), post-mortem analysis (marked with b) and Witt et al. [65] (marked with c). for rebuilt experimental cell from commercial LG 18650 HG2

| Parameter | Unit | Negative | Separator | Positive |
|---|---|---|---|---|
| [b]Particle radius, R | µm | 4 | - | 2.5 |
| [b]Electrode thickness, d | µm | 56.3 | 220 | 46.6 |
| [a]Active material volume fraction, $\varepsilon_s$ | - | 0.55 | - | 0.67 |
| [a]Electrolyte volume fraction, $\varepsilon_e$ | - | 0.42 | 0.74 | 0.19 |
| [c]Bruggemann constant, $\beta$ | - | 2.74 | 1 | 0.89 |
| [c]Transference number, $t_p$ | - | | 0.24 | |
| [c]Electrolyte concentration, $c_{el}$ | $mol\,m^{-3}$ | | 1000 | |

**Table A.2:** Redlich Kister coefficients in $J\,mol^{-1}$.

| Coefficient | Negative | Positive |
|---|---|---|
| $A_1$ | -6536.41 | -26070.50 |
| $A_2$ | 7866.77 | 2100.65 |
| $A_3$ | -11935.70 | 7233.14 |
| $A_4$ | 1247.70 | 19521.57 |
| $A_5$ | 15127.43 | -20571.70 |
| $A_6$ | 91743.97 | -89723.30 |
| $A_7$ | 64700.28 | 114776.10 |
| $A_8$ | -445264.00 | 154066.10 |
| $A_9$ | -310992.00 | -253362.00 |
| $A_10$ | 988557.30 | -109429.00 |
| $A_11$ | 393655.50 | 235359.00 |
| $A_12$ | -990131.00 | 29709.15 |
| $A_13$ | -160243.00 | -81957.70 |
| $A_14$ | 367108.10 | 0 |

**Table A.3:** Chemical potentials in $\mathrm{J\,mol^{-1}}$.

| Parameter | Value |
|---|---|
| $\mu^0_{\mathrm{neg,Li(s)}}$ | $-1.7042 \cdot 10^4$ |
| $\mu^0_{\mathrm{V_{Li}(s)}}$ | 0 |
| $\mu^0_{\mathrm{Li(neg/SEI)}}$ | 0 |
| $\mu^0_{\mathrm{V_{Li}(neg/SEI)}}$ | 0 |
| $\mu^0_{\mathrm{Li^+(SEI/e)}}$ | 0 |
| $\mu^0_{\mathrm{V_{Li}(SEI/e)}}$ | 0 |
| $\mu^0_{\mathrm{Li^+(e)}}$ | 0 |
| $\mu^0_{\mathrm{e^-(s)}}$ | 0 |
| $\mu^0_{\mathrm{pos,Li(s)}}$ | $-3.8036 \cdot 10^5$ |

# A.4 Parameterisation ageing study for the commercial LG 18650 HG2

**Table A.4:** List of parameters that change at different ageing instantaneous of full cell commercial LG 18650 HG2.

| **Parameter** | **Unit** | **before cycling** | 500$^{th}$cycle | 1000$^{th}$cycle | 2000$^{th}$cycle | 3000$^{th}$cycle |
|---|---|---|---|---|---|---|
| Active material volume fraction | | | | | | |
| Positive electrode, $\varepsilon_{s,pos}$ | - | 0.67 | 0.58 | 0.53 | 0.48 | 0.37 |
| Negative electrode, $\varepsilon_{s,neg}$ | - | 0.57 | 0.49 | 0.47 | 0.43 | 0.34 |
| Charge transfer coefficient | | | | | | |
| Charge transfer process at positive electrode, $\alpha_{pos}$ | - | 0.55 | 0.55 | 0.55 | 0.55 | 0.55 |
| Charge transfer process at negative electrode, $\alpha_{s/SEI}$ | - | 0.50 | 0.50 | 0.50 | 0.50 | 0.50 |
| Ad-/desorption at SEI, $\alpha_{SEI/e}$ | - | 0.50 | 0.50 | 0.50 | 0.50 | 0.50 |
| Rate constant | | | | | | |
| Charge transfer process at poitive electrode, $k_{0,pos}$ | $m\,s^{-1}$ | $4.21 \cdot 10^{-9}$ | $2.31 \cdot 10^{-9}$ | $7.36 \cdot 10^{-10}$ | $1.79 \cdot 10^{-10}$ | $4.21 \cdot 10^{-11}$ |
| Charge transfer process at negative electrode, $k_{0,s/SEI}$ | $s^{-1}$ | 100 | 20 | 12 | 3 | 2.5 |
| Ad-/desorption at SEI, $k_{0,SEI/e}$ | $s^{-1}$ | $4.0 \cdot 10^{6}$ | $4.0 \cdot 10^{6}$ | $4.0 \cdot 10^{6}$ | $4.0 \cdot 10^{6}$ | $2.0 \cdot 10^{6}$ |
| Double layer capacitance | | | | | | |
| Charge transfer process at positive electrode, $C^{DL}_{pos}$ | $F^2\,m^{-1}$ | 2 | 2 | 5 | 5 | 5 |
| Charge transfer process at negative electrode, $C^{DL}_{s/SEI}$ | $F^2\,m^{-1}$ | 20 | 10 | 7 | 30 | 10 |
| Ad-/desorption at negative electrode, $C^{DL}_{SEI/e}$ | $F^2\,m^{-1}$ | 0.4 | 0.5 | 0.5 | 0.5 | 2.5 |
| Electronic conductivity | | | | | | |
| Positive electrode, $\sigma_{s,pos}$ | $S\,m^{-1}$ | 0.02 | 0.02 | 0.02 | 0.02 | 0.02 |
| Negative electrode, $\sigma_{s,neg}$ | $S\,m^{-1}$ | 15.4 | 15.4 | 15.4 | 0.3 | 0.04 |
| SEI thickness, $d_{SEI}$ | nm | 78 | 200 | 300 | 340 | 350 |
| SEI ionic conductivity, $\kappa_{SEI}$ | $S\,m^{-1}$ | $2.61 \cdot 10^{-4}$ | $2.61 \cdot 10^{-4}$ | $2.61 \cdot 10^{-4}$ | $2.61 \cdot 10^{-4}$ | $2.61 \cdot 10^{-4}$ |

**Table A.5:** List of parameters that assume constant for the ageing of full cell commercial LG 18650 HG2.

| Parameter | Unit | Negative | Separator | Positive |
|---|---|---|---|---|
| Particle radius, R | µm | 4 | - | 2.5 |
| Electrode thickness, d | µm | 56.3 | 220 | 46.6 |
| Electrolyte volume fraction, $\varepsilon_e$ | - | 0.42 | 0.74 | 0.27 |
| Bruggemann constant, $\beta$ | - | 2.74 | 1 | 0.89 |
| Transference number, $t_p$ | - | | 0.24 | |
| Electrolyte concentration, $c_{el}$ | $\mathrm{mol\,m^{-3}}$ | | 1000 | |
| Maximum active material concentration, $c_{s,max}$ | $\mathrm{mol\,m^{-3}}$ | 38632 | - | 37898 |
| Initial active material concentration, $c_{s,0}$ | $\mathrm{mol\,m^{-3}}$ | 38594 | - | 1388.3 |
| Contact resistance, $R_{cc}$ | $\omega/\mathrm{m^2}$ | $1 \cdot 10^{-4}$ | - | $6 \cdot 10^{-4}$ |

**Table A.6:** Redlich Kister coefficients in $\mathrm{J\,mol^{-1}}$ for full cell commercial LG 18650 HG2.

| Coefficient | Negative | Positive |
|---|---|---|
| $A_1$ | -6536.41 | -26070.50 |
| $A_2$ | 7866.77 | 2100.65 |
| $A_3$ | -11935.70 | 7233.14 |
| $A_4$ | 1247.70 | 19521.57 |
| $A_5$ | 15127.43 | -20571.70 |
| $A_6$ | 91743.97 | -89723.30 |
| $A_7$ | 64700.28 | 114776.10 |
| $A_8$ | -445264.00 | 154066.10 |
| $A_9$ | -310992.00 | -253362.00 |
| $A_10$ | 988557.30 | -109429.00 |
| $A_11$ | 393655.50 | 235359.00 |
| $A_12$ | -990131.00 | 29709.15 |
| $A_13$ | -160243.00 | -81957.70 |
| $A_14$ | 367108.10 | 0 |

**Table A.7:** Chemical potentials in $\mathrm{J\,mol^{-1}}$ for full cell commercial LG 18650 HG2.

| Parameter | Value |
|---|---|
| $\mu^0_{\mathrm{neg,Li(s)}}$ | $-1.7042 \cdot 10^4$ |
| $\mu^0_{\mathrm{V_{Li}(s)}}$ | 0 |
| $\mu^0_{\mathrm{Li(neg/SEI)}}$ | 0 |
| $\mu^0_{\mathrm{V_{Li}(neg/SEI)}}$ | 0 |
| $\mu^0_{\mathrm{Li^+(SEI/e)}}$ | 0 |
| $\mu^0_{\mathrm{V_{Li}(SEI/e)}}$ | 0 |
| $\mu^0_{\mathrm{Li^+(e)}}$ | 0 |
| $\mu^0_{\mathrm{e^-(s)}}$ | 0 |
| $\mu^0_{\mathrm{pos,Li(s)}}$ | $-3.8036 \cdot 10^5$ |

# B Publications within the Research of the Dissertation

## B.1 Journal publications

- H.S. Chan, E.J.F. Dickinson, T.P. Heins, J. Park, M. Gaberšček, Y.Y. Lee, M. Heinrich, V. Ruiz, E. Napolitano, P. Kauranen, E. Fedorovskaya, J. Moškon, T. Kallio, S. Mousavihashemi, U. Krewer, G. Hinds, S. Seitz
  "Comparison of methodologies to estimate state-of-health of commercial Li-ion cells from electrochemical frequency response data", *Journal of Power Sources*, vol. 542, pp. 231814, 2022. [Online]. Available: https://doi.org/10.1016/j.jpowsour.2022.231814

- H.S. Chan, L. Bläubaum, D. Vijayshankar, F. Röder, C. Nowak, A. Weber, A. Kwade, U. Krewer
  "Revealing the Impact of Particle Size Distribution on Ageing of Lithium-Ion Batteries with Frequency Response Analysis", *Batteries & Supercaps*, vol. 6, issue 10, e202300203, 2023. [Online]. Available: https://doi.org/10.1002/batt.202300203

- H.S. Chan, Y.Y. Lee, D. Witt, J. Ulrich, A. Weber, U. Krewer
  "Improved Identifiability of Kinetic Parameters in Lithium-ion Batteries via Nonlinear Frequency Response Analysis", *Batteries & Supercaps*, vol. 8, issue 11, e202500179, 2025. [Online]. Available: https://doi.org/10.1002/batt.202500179

- L. Bläubaum, F. Röder, C. Nowak, H.S. Chan, A. Kwade, U. Krewer
  "Impact of Particle Size Distribution on Performance of Lithium-Ion Batteries", *ChemElectroChem*, vol. 7, no. 23, pp. 4755-4766, 2020. [Online].
  Available: https://doi.org/10.1002/celc.202001249

- T. Vidaković-Koch, T. Miličić, L.A. Živković, H.S. Chan, U. Krewer, M. Petkovska
  "Nonlinear frequency response analysis: a recent review and perspectives", *Current Opinion in Electrochemistry*, vol. 30, pp. 100851, 2021. [Online].
  Available: https://doi.org/10.1016/j.coelec.2021.100851

- Y.Y. Lee, H.S. Chan, A. Weber, U. Krewer
  "Full-, Half-, and Symmetrical Cell Analysis of Lithium-Ion Battery Using Impedance and Nonlinear Frequency Response", *Journal of The Electrochemical Society*, vol. 171, no. 7, pp. 070543, 2024. [Online]. Available: https://doi.org/10.1149/1945-7111/ad5ef9

## B.2 Conference contributions

- H.S. Chan, E.J.F. Dickinson, T.P. Heins, J. Park, Y.Y. Lee, A. Weber, S. Seitz, U. Krewer
  "Nonlinear Frequency Response Analysis in Capacity Estimation and Accelerated Aging Identification of Li-ion Batteries", $12^{th}$ International Symposium on Electrochemical Impedance Analysis, Presentation (Online), November 29-30, 2021
- H.S. Chan, Y.Y. Lee, D. Witt, A. Weber, U. Krewer
  "Nonlinear Frequency Response Analysis – A Modelling Assessment for Li-ion Batteries", $18^{th}$ Symposium on Modeling and Experimental Validation of Electrochemical Energy Technologies, Hohenkammer, Presentation, March 14-16, 2022
- J. Ulrich, H.S. Chan, A. Weber, U. Krewer
  "Modeling the Nonlinear Frequency Response of plated Lithium-Ion Batteries", $19^{th}$ Symposium on Modeling and Experimental Validation of Electrochemical Energy Technologies, Duisburg, Poster, March 21-23, 2023
- Y.Y. Lee, H.S. Chan, A. Weber, U. Krewer
  "Electrode-resolved analysis of nonlinearities in NMC/Si-Graphite lithium-ion battery", Advanced Battery Power: The International Conference (Kraftwerk Batterie), Aachen, Poster, April 26-28, 2023
- Y.Y. Lee, H.S. Chan, A. Weber, U. Krewer
  "Exploring the Potential of Nonlinear Frequency Response Analysis in Electrode-Resolved and Full-Cell Lithium-ion Batteries", $35^{th}$ Topical Meeting of the International Society of Electrochemistry, Australia, Presentation, May 7-10, 2023
- Y.Y. Lee, H.S. Chan, A. Weber, U. Krewer
  " Accelerated Aging of Lithium-Ion Batteries: Insights from Nonlinear Frequency Response Analysis", $244^{th}$ ECS Meeting, Gothenburg, Sweden, Presentation, Oct 8-12, 2023
- U. Krewer, A. Weber, J. Ulrich, H.S. Chan
  " Nonlinear Frequency Response Analysis – Basics and Application for Battery Analysis", PRiME 2024, Honolulu, USA, Presentation, Oct 6-11, 2024